

Wearable multi-electrode platform for ion sensing

Présentée le 6 avril 2020

à la Faculté informatique et communications
Laboratoire des systèmes intégrés (IC/STI)
Programme doctoral en microsystemes et microélectronique

pour l'obtention du grade de Docteur ès Sciences

par

Francesca CRISCUOLO

Acceptée sur proposition du jury

Prof. D. Atienza Alonso, président du jury
Prof. G. De Micheli, Dr S. Carrara, directeurs de thèse
Prof. D. De Marchi, rapporteur
Dr F. Catthoor, rapporteur
Prof. M. Gijs, rapporteur

*A Wendy,
la regina del mio cuore*

If we knew what it was we were doing, it would not be called research, would it?
— Albert Einstein

Acknowledgements

The first acknowledgement can only go to the person who let me take this important path: thanks *Nanni* for giving me the opportunity to work and grow in the LSI group and for always guiding and supporting me with dedication during these years. I also want to express my sincere gratitude to my second mentor: thanks *Sandro* for the endless and useful scientific discussions and for the enthusiasm that you have always transmitted me. I hope I can always keep it and show it to the others too. Furthermore, I would like to thank *each jury member* for accepting to be part of this work and for the interest they have shown.

The second part of my acknowledgements goes to *my family*: thank you *mom, dad and Marco* for your infinite love and for always supporting me. Even if far away, you are always my home and my most solid point of reference. And, of course, thank you *Wendy*, for giving me the best moments and for teaching me what true love is. You will always live in the most special part of my heart. I dedicate this thesis to you.

Thanks to my grandfather, *nonno Mimí*, whose curiosity, sympathy and energy I always carry with me and in my way of being.

Thanks to all *my family from Salerno* for their sincere affection despite the distance. Thanks to all my very nice uncles, caring aunts and beautiful cousins, to Aunt Pina, to uncle Paolo. Thanks to my special grandmother, *nonna Tetta*.

Furthermore, I have to thank all my friends.

Thanks first of all to those who are now looking at me from a bright star, thanks *Alessandro* and *Fabio*. You are one of the reasons why I wrote this thesis and even if you are not in this world anymore, you will always live in my heart. I owe much of my way of being to you and to your courage. You have been and will always be a true example, as well as part of me.

Thanks *Marco* and *Fil* for your historical and deep friendship. Even if you are far away, you are always like brothers to me.

Thank you *Teo*, for your sincere friendship, for your contagious joy and for all the adventures and binges.

Thank you *Awet*, for becoming my little brother in such a short period of time. You are such an incredible and genuine person, I am so lucky to have you as a friend.

Thank you *Stefano*, our friendship was born quite randomly, but you come up to be one of the

Acknowledgements

people I admire the most. Thank you for sharing your energy and 'craziness' with me.

Thanks to *Daniele* and *Silvia* for all funny moments and skiing days together.

Thanks to my special friends in Salerno: *Fra, Luca, Giuliano, Peppe, Davide, Sergio, Alessandra, Roberta, Andrea, Alfonso, Anna, Alessandro, Paola* and all the others.

Thanks to my LSI family and in particular to those who in those years have conquered an important space in my life: to *Ele* for her sincere affection, to *FraS* and *Enrico* for their infinite availability and energy, to *Simo* for his generosity and for being an amazing 'husband', to *Giovanni* for all the wonderful adventures together in the mountains and beyond, to *Ivan* for his sympathy and honesty, to *Aya* for her infinite affection and for being a great office mate, to *Giulia* for all the funny moments, to *Enrico C.* for his kindness. To *Nadja* and *Irene* for their infinite sweetness and their precious scientific and moral support in all the most difficult moments. You are certainly among the people I respect the most in the world, from a professional and non-professional point of view. Thanks *Cristina* for your affection, thanks *Carole* for your efficiency, thanks *Chantal* for your support and valuable help. Thanks to my students *Marco* and *Kwassi* for the great work together. Thanks to *all other LSIs* for the amazing moments together.

Thanks to *my friends around the world* for all the unforgettable moments they gave me. In particular thanks *Bil, Paola* and *Nico* for all the adventures together. Thanks *Tea* and *Chiara* for your sweetness.

Thanks to *Nico* and all my *friends from Nanolab and volleyball* for the good moments together. Thank you to the *CMI staff*, and in particular to *Nico, Rémy, Julien* et *Cyrille* for their precious help and patience in the cleanroom.

Thanks to *Fiorella, Dario* and *Ambra* for having always been close to me.

Thanks to the *Afifi family*, the *Santopolo family*, to *my brother's friends*, to *Gio*, with whom I grew up.

Thanks to *Mrs. Verde* and *nonna Ginetta*, my incredible acquired grandmothers.

Thanks to my second mother, *Maria Teresa*, who has always accompanied me, in the musical world and not only, since I was a child.

Thanks to the *Ferrigno family*, for their sincere affection and for always welcoming me like a daughter. You are truly a second family to me. Thanks to *Virgola* who fills my heart of joy with her sincere love and energy.

Finally thanks to the most incredible person of all, despite the distance and the difficulties, for his profound honesty, for his unconditional love, for the continuous support, for his incredible ability to question and improve himself every day, thank you my love, thanks *Gigi*,

Francesca

Il primo ringraziamento non può che andare alla persona che mi ha permesso di intraprendere questo importante percorso: grazie *Nanni* per avermi dato l'opportunità di lavorare e crescere nel gruppo LSI e per avermi sempre guidata e supportata con dedizione durante questi anni. Voglio inoltre esprimere la mia più sincera gratitudine al mio secondo mentore: grazie *Sandro* per le interminabili ed utili discussioni scientifiche e per l'entusiasmo che mi hai sempre trasmesso. Spero di riuscire sempre a mantenerlo e mostrarlo agli altri anche io. Inoltre vorrei ringraziare i *membri della giura* per aver accettato di essere parte di questo lavoro e per l'interesse dimostrato.

La seconda fetta dei miei ringraziamenti è rivolta alla *mia famiglia*: grazie *mamma, papà e Marco* per il vostro amore infinito e per avermi sempre sostenuto. Anche se lontani, siete sempre la mia casa ed il mio più solido punto di riferimento. Ed ovviamente grazie *Wendy*, per avermi regalato le emozioni più belle e per avermi insegnato cosa sia il vero amore. Vivrai sempre nella parte più speciale del mio cuore. A te dedico questa tesi.

Grazie al mio nonnino, *nonno Mimí*, la cui curiosità, simpatia ed energia porto sempre con me e nel mio modo di essere.

Grazie a tutta *la mia famiglia salernitana* per il loro sincero affetto nonostante la lontananza. Grazie a tutti i miei simpaticissimi zii, alle premurose zie ed agli splendidi cugini, a zia Pina, a zio Paolo. Grazie alla mia nonna speciale, *nonna Tetta*.

Non posso inoltre non ringraziare tutti i miei amici.

Grazie innanzitutto a chi mi guarda da lassù, grazie *Alessandro e Fabio*. Siete uno dei motivi per cui ho scritto questa tesi ed anche se ora non siete più qui, vivete sempre nel mio cuore e gran parte del mio modo di essere lo devo a voi ed al vostro coraggio. Siete stati e sarete sempre un vero esempio, nonché parte di me. Vi porterò in ogni mio gesto.

Grazie *Marco e Fil* per la vostra storica e profonda amicizia. Anche se ora siete lontani, siete sempre dei fratelli per me.

Grazie *Teo*, per la tua sincera amicizia, per la tua allegria contagiosa e per tutte le avventure e mangiate.

Grazie *Awet*, per essere diventato come un fratello minore per me in un periodo di tempo così breve. Sei una persona incredibile e genuina, sono davvero fortunata ad averti come amico!

Grazie *Stefano*, la nostra amicizia è nata in modo abbastanza casuale, ma sei arrivato ad essere una delle persone che ammiro di più. Grazie perché condivedi la tua energia e sana "follia" con me.

Grazie *Daniele e Silvia* per tutti i momenti divertenti e le sciare assieme.

Grazie ai miei speciali amici salernitani: *Fra, Luca, Giuliano, Peppe, Davide, Sergio, Alessandra, Roberta, Andrea, Alfonso, Anna, Alessandro, Paola ed ad tutti gli altri*.

Grazie alla mia seconda famiglia LSI ed in particolare a coloro che in questi anni hanno conquistato uno spazio importante nella mia vita: ad *Ele* per il suo sincero affetto, a *FraS* ed *Enry* per la loro infinita disponibilità ed energia, a *Simo* per la sua generosità e per essere 'marito' insostituibile, a *Giovanni* per tutte le meravigliose avventure assieme in montagna e non solo, ad *Ivan* per la sua simpatia e bontà, ad *Aya* per il suo infinito affetto e per essere stata una compagna di ufficio speciale, a *Giulia* per tutti i momenti divertenti, ad *Enrico C.* per la sua gentilezza. A *Nadja* ed *Irene* per la loro infinita dolcezza e per il loro prezioso supporto

Acknowledgements

scientifico e morale in tutti i momenti più difficili. Siete sicuramente tra le persone che stimo di più al mondo, dal punto di vista professionale e non. Grazie *Cristina* per il tuo affetto, grazie *Carole* per la tua efficienza, grazie *Chantal* per il tuo supporto e prezioso aiuto. Grazie ai miei studenti *Marco* e *Kwassi* per il bel lavoro svolto assieme. Grazie a tutti gli altri LSiers per ogni momento trascorso assieme.

Grazie *ai miei amici sparsi per il mondo* per tutti i momenti indimenticabili che mi hanno regalato. In particolare grazie *Bil*, *Paola* e *Nico* per tutte le avventure assieme. Grazie a *Tea* e *Chiara* per la loro dolcezza.

Grazie a *Nico* ed agli *amici del Nanolab e di pallavolo* per i bei momenti di spensieratezza assieme.

Grazie allo *staff del CMI*, ed in particolare a *Nico*, *Rémy*, *Julien* et *Cyrille* per il loro prezioso aiuto in cleanroom e per l'infinita pazienza.

Grazie a *Fiorella*, *Dario* ed *Ambra* per essermi sempre stati vicina anche da lontano.

Grazie alla *famiglia Afifi*, alla *famiglia Santopolo*, *agli amici di mio fratello*, a *Gio*, con i quali sono cresciuta.

Grazie alla *Sig. Verde* ed a *nonna Ginetta*, le mie incredibili nonne acquisite.

Grazie alla mia seconda mamma, *Maria Teresa*, che mi ha sempre accompagnato nel mondo musicale e non fin da quando sono piccola.

Grazie alla *famiglia Ferrigno*, per il loro affetto sincero e per avermi sempre accolta come una figlia. Siete davvero una seconda famiglia per me. Grazie a *Virgola* che mi riempie di gioia con il suo amore sincero e la usa energia.

Infine grazie alle persona più incredibile di tutte, nonostante la lontananza e le difficoltà, per la sua profonda onestà, per il suo amore incondizionato, per il supporto continuo, per la sua incredibile capacità di mettersi in discussione e migliorarsi ogni giorno, grazie amore mio, grazie *Gigi*,

Francesca

Abstract

With the growth of personalized medicine and e-Health, there has been an increasing interest in the development of accurate sensing systems able to support this healthcare revolution for both in- and off-hospital monitoring. Remote biosensing devices can dramatically simplify the acquisition, management and exchange of clinical data and facilitate check-ups without moving the patient and/or the physician. In addition, the emerging data-driven healthcare model enables the delivery of personalized treatments, the so-called *personalized medicine*. This is a recent branch of medicine that tackles the low efficacy of many pharmacological treatments as it is now well-known that the response of each individual may vary significantly from person to person. Wearable devices occupy a primary role in this data-driven revolution to collect data in medicine. Despite the great research efforts, current wearable biosensors still have several issues, such as poor collection, separate sampling and analysis, low multi-sensing capabilities, drifts and lack of data for the correlation with blood values. Progress in materials science to enhance sensitivity, selectivity, detection range, and to reduce costs is also needed. This thesis investigates and addresses some of the challenges related to wearable chemical sensors, with particular interest on sweat sensing. This field is very attractive as this biofluid is highly promising as alternative to blood in diagnostics. In fact, it is readily accessible and reproducible, it does not require invasive procedures like blood collection, it contains several recognized biomarkers with diagnostic capabilities and good correlation with blood values, and it can be easily monitored continuously. In this thesis, a wearable electrochemical platform addressing some of these challenges is fabricated. This device enables the monitoring of several ions for different applications: Li^+ for *Therapeutic Drug Monitoring* (TDM) of people affected by psychiatric disorders, Pb^{2+} for the control of heavy metal contamination, K^+ and Na^+ for tracking of physical exercise.

The sensing is based on the use of *Solid-Contact Ion-Selective Electrodes* (SC-ISEs) with noble metal nanostructures. These materials are efficiently deposited in a fast on-step electrodeposition process. We demonstrate the superior behaviour of the sensors in terms of sensitivity, selectivity and stability, both on macro and miniaturized electrodes. The sensors are successfully proposed for the first time for the monitoring of lithium levels in sweat for applications in TDM of psychiatric disorders. Lead sensors are also fabricated and tested in sweat to pro-

Abstract

pose an innovative method for the control of heavy metal contamination. In addition, the detection of sweat potassium and sodium for physical exercise and hydration monitoring is also demonstrated. A custom-made flexible electrochemical sensing system including a temperature sensor, a stable reference electrode and several ion-sensing channels is fabricated with lithographic techniques. The platform is integrated with low-cost cotton fluidics that enables the collection of fresh sweat and the disposal of the already-tested sample fluid. The successful tracking of sodium and potassium ions in human volunteers during physical exercise monitoring is reported. With its high accuracy, selectivity and stability, this device represents an important step towards the development of efficient and low-cost non-invasive healthcare tracking systems for e-Health.

Keywords: *Wearable sensors; ions; sweat; flexible sensors; solid contact; potentiometric sensors; ion-selective electrodes; electrochemical sensors.*

Résumé

Les progrès en médecine personnalisée et e-Health ont suscité un intérêt croissant pour le développement de systèmes de détection précis, capables de soutenir cette révolution des services de santé pour le contrôle médical en milieu hospitalier et non-hospitalier. Les biocapteurs connectés permettent de simplifier considérablement l'acquisition, la gestion et l'échange de données cliniques, et facilitent les contrôles nécessaires requis par les protocoles de soins, sans avoir à déplacer le patient et/ou le médecin. En outre, l'émergence des modèles médicaux basés sur les données rend possible l'administration de traitements personnalisés, la dénommée *médecine personnalisée*. Il s'agit d'une branche récente de la médecine qui adresse la faible efficacité de nombreux traitements pharmacologiques, étant donné que la réponse de chaque individu peut varier considérablement d'une personne à l'autre. Les capteurs portables occupent un rôle primordial dans cette révolution digitale pour la collecte de données. Malgré les grands efforts de recherche, les biocapteurs portables actuels sont sujets à divers problèmes, tels que la mauvaise collecte, l'échantillonnage et l'analyse séparés des données, les faibles capacités de multi-détection, et le manque de données corrélant les valeurs obtenues via la transpiration et le sang. Des progrès en science des matériaux sont également nécessaires afin d'améliorer la sensibilité, la sélectivité, la plage de détection, et les coûts des capteurs.

La présente thèse porte sur l'étude des capteurs chimiques portables, et tente de répondre à certains des défis auxquels ils sont confrontés, avec un intérêt particulier pour la détection à partir de la sueur. Ce domaine est extrêmement attractif puisque ce fluide biologique est particulièrement prometteur comme alternative aux diagnostics sanguins. À savoir, il est facilement accessible et reproductible en laboratoire, il ne nécessite pas de procédures invasives comme le prélèvement de sang, il contient plusieurs biomarqueurs (électrolytes et métabolites) et manifeste une bonne corrélation avec les valeurs sanguines. Les mesures à partir de la sueur peuvent être réalisées en continu également. Dans ce travail, une plate-forme électrochimique portable qui adresse certains des défis susdits est fabriquée. Ce dispositif permet la détection de plusieurs ions pour différentes applications : Li^+ pour l'optimisation de la dose de lithium des personnes souffrant de troubles psychiatriques, Pb^{2+} pour le contrôle de la contamination par les métaux lourds, K^+ et Na^+ pour le suivi de l'exercice physique.

La détection est basée sur l'utilisation d'électrodes sélectives aux ions à contact solide avec des nanostructures de métaux nobles. Ces matériaux peuvent être déposés de manière efficace avec un rapide processus d'électrodéposition. L'excellente réponse des biocapteurs en termes de sensibilité, de sélectivité, et de stabilité à long terme est prouvée sur des macro- et microélectrodes. Ces capteurs ont été utilisés pour démontrer avec succès, et pour la première fois, l'optimisation non-invasive de la dose de lithium dans les troubles psychiatriques, ainsi que pour le contrôle de la contamination par les métaux lourds dans la transpiration. De plus, la détection de potassium et sodium pour la surveillance de l'exercice physique et de l'hydratation est également démontrée. Un dispositif de détection électrochimique sur mesure, et sur support flexible, comprenant un capteur de température, une électrode de référence stable à contact solide, et plusieurs canaux de détection d'ions, est fabriqué avec des techniques lithographiques. La plate-forme est intégrée avec un système fluidique économique en coton, qui permet la collecte de sueur fraîche et l'élimination du fluide déjà testé. Enfin, le système complet est utilisé avec succès pour la détection de sodium et potassium dans la sueur des volontaires humains pendant l'activité physique. La haute précision, la sélectivité, et la stabilité du dispositif proposé représente une étape importante vers le développement de biocapteurs non-invasifs, efficaces, et économiques pour la santé digitale.

Mots Clés : *Capteurs portables ; ions ; transpiration ; capteurs flexibles ; contact solide ; capteurs potentiométriques ; électrodes sélectives d'ions ; capteurs électrochimiques.*

Sommario

Con la crescita della medicina personalizzata e della e-Health, gli ultimi anni hanno visto un crescente interesse verso lo sviluppo di sensori in grado di sostenere questa rivoluzione sanitaria che coinvolge il monitoraggio dei pazienti sia all'interno che all'esterno dell'ospedale. I dispositivi di monitoraggio remoto possono semplificare notevolmente l'acquisizione, la gestione e lo scambio di dati clinici e facilitare i controlli necessari richiesti dai protocolli di cura, senza spostare il paziente e/o il medico. Inoltre, l'emergente modello di medicina digitale consente di fornire trattamenti personalizzati ai pazienti, secondo la cosiddetta *medicina personalizzata*. Questo è un ramo recente della medicina che vuole risolvere il problema della bassa efficacia di molti trattamenti farmacologici. Infatti è ormai noto che la risposta di ciascun individuo può variare in modo significativo da persona a persona. I dispositivi indossabili occupano un ruolo primario in questa rivoluzione digitale per la raccolta di dati. Nonostante i grandi sforzi di ricerca, gli attuali sensori indossabili presentano ancora diversi problemi irrisolti, come la difficile raccolta dei campioni, la separazione di campionamento ed analisi, le scarse capacità di multi-sensing e la mancanza di dati che correlano i valori di sudore e sangue. Sono inoltre necessari progressi nella scienza dei materiali al fine di ridurre i costi e migliorare sensibilità e selettività.

Questa tesi vuole indagare ed affrontare alcune delle sfide relative ai sensori chimici indossabili, con particolare interesse per il sudore. Questo campo è estremamente promettente in quanto questo biofluido è particolarmente promettente come alternativa al più usato sangue. Infatti, esso è facilmente accessibile e riproducibile in laboratorio, non richiede procedure invasive come il prelievo del sangue, contiene diversi biomarcatori (elettroliti e metaboliti) con capacità diagnostiche e buona correlazione con i valori nel sangue, e può essere facilmente monitorato in modo continuo. In questo lavoro viene fabbricata una piattaforma elettrochimica indossabile che cerca di affrontare alcune di queste problematiche. Il dispositivo consente il monitoraggio di diversi ioni per varie applicazioni: Li^+ per l'ottimizzazione della dose di litio in persone affette da disturbi psichiatrici, Pb^{2+} per il controllo della contaminazione da metalli pesanti, K^+ e Na^+ per il monitoraggio dell'esercizio fisico e dell'idratazione.

Il rilevamento si basa sull'uso di elettrodi ionoselettivi a contatto solido basati su nanostrutture di metalli nobili. Questi materiali possono essere depositati in modo efficiente e rapido tramite

un processo elettrochimico. L'eccellente risposta dei sensori in termini di sensibilità, selettività e stabilità a lungo termine viene dimostrata in questo lavoro su macro- e microelettrodi. Per la prima volta, inoltre, viene proposto l'utilizzo di questi sensori per l'ottimizzazione non invasiva della dose di litio in persone affette da disturbi psichiatrici e per il controllo di contaminazione da metalli pesanti mediante analisi del sudore. Inoltre, viene riportato anche il rilevamento di potassio e sodio nel sudore per il monitoraggio dell'esercizio fisico e dell'idratazione. Viene fabbricato, inoltre, tramite tecniche litografiche, un sistema flessibile di sensori elettrochimici che include un sensore di temperatura, un elettrodo di riferimento a contatto solido stabile e diversi canali per il rilevamento di ioni. La piattaforma include una fluidica in cotone economica che consente la raccolta di sudore fresco e lo smaltimento del fluido già testato. Il sistema completo viene infine usato con successo per il monitoraggio di sodio e potassio nel sudore di volontari umani durante l'attività fisica. Con la sua elevata precisione, selettività e stabilità, questo dispositivo rappresenta un passo importante verso lo sviluppo di sistemi di monitoraggio non invasivi, efficienti ed economici per la rivoluzione digitale della medicina moderna.

Parole chiave: *Sensori indossabili; ioni; sudore; sensori flessibili; contatto solido; sensori potenziometrici; elettrodi ione-selettivi; sensori elettrochimici.*

Indice

Acknowledgements (English/Italian)	i
Abstract (English/Français/Italiano)	v
List of acronyms	xxv
1 The healthcare revolution	1
1.1 Data-driven healthcare: e-Health and personalized medicine.	2
1.2 Sweat as alternative biofluid	5
1.2.1 Sweat production by eccrine glands	5
1.2.2 Comparison with other bodily fluids	8
1.2.3 Main applications area	8
1.2.4 Challenges	9
1.3 Importance of ion-sensing	9
1.4 Research contributions	11
1.5 Thesis outline	12
2 Ion-Selective Electrodes (ISEs)	13
2.1 The main advantages of ISEs	13
2.2 Ion activity and activity coefficients	14
2.3 Structure and working principle of ISEs	15
2.4 Towards all-solid-state ISEs	17
2.4.1 Solid contacts based on conductive polymers	18
2.4.2 Solid contacts based on nanostructured layers	19
2.5 Performance evaluation criteria of ISEs	20
2.5.1 Sensitivity	20
2.5.2 Limit Of Detection (LOD)	21
2.5.3 Potential response and stability	22
2.5.4 Interference studies	24

2.6	State-of-the-art and challenges in solid-contact ISEs	26
3	Noble metals nanostructured layers for improved ion-sensing	31
3.1	State-of-the-art on SC materials	31
3.2	Experimental methods	32
3.2.1	Materials and micro-electrodes fabrication	32
3.2.2	ISM fabrication	33
3.2.3	Morphological characterization	33
3.2.4	Electrochemical measurements	34
3.3	Noble metal nanostructures for highly-stable solid-contact ISEs	34
3.3.1	Morphological characterization	36
3.3.2	Characterization by current reversal chronopotentiometry and cyclic voltammetry	37
3.3.3	Sensor calibration	41
3.3.4	Stability of potential response	42
3.3.5	Selectivity studies	43
3.4	Mixed gold and platinum nanostructured solid contacts	43
3.4.1	Morphological characterization	43
3.4.2	Characterization by current reversal chronopotentiometry and cyclic voltammetry	44
3.4.3	Sensor calibration	45
3.5	Fast electrodeposition procedures of platinum nanostructures on miniaturized electrodes	47
3.5.1	Morphological characterization	47
3.5.2	Current reversal chronopotentiometry and solid-contact capacitance . .	48
3.5.3	Calibration of the lithium ion-selective electrodes	50
3.5.4	Reversibility and lifetime studies	52
3.6	Summary	53
3.7	Main contributions and conclusions	54
4	Use of nanostructured solid-contact ISEs in healthcare for sweat analysis	55
4.1	Lithium monitoring in mood disorders	55
4.1.1	Motivation	55
4.1.2	Experimental methods	57
4.1.3	Experimental results and discussion	58
4.1.4	Summary	63
4.2	Monitoring of heavy metal contamination	63
4.2.1	Motivation	63
4.2.2	Experimental methods	64
4.2.3	Experimental results and discussion	65
4.2.4	Summary	68
4.3	Monitoring of physical exercise	68
4.3.1	Motivation	68

4.3.2	Experimental methods	70
4.3.3	Experimental results and discussion	71
4.3.4	Summary	77
4.4	Main contributions and conclusions	77
5	Fabrication of a flexible electrochemical platform	79
5.1	Microfabrication of a flexible integrated platform	79
5.1.1	Design constraints	80
5.1.2	Design of the flexible platform prototype	81
5.1.3	Process flow	82
5.1.4	Summary	90
5.2	Characterization of the flexible WEs	90
5.2.1	Electrochemical tests	90
5.2.2	Bending tests	92
5.2.3	Summary	92
5.3	Flexible all-solid-state REs	93
5.3.1	Motivation	94
5.3.2	Experimental methods	94
5.3.3	Testing of different all-solid-state REs on rigid substrates	95
5.3.4	Fabrication and testing of flexible all-solid-state REs	99
5.3.5	Summary	100
5.4	Use of the complete flexible electrochemical system for lithium detection	100
5.4.1	Experimental methods	101
5.4.2	Experimental results and discussion	102
5.4.3	Summary	102
5.5	Integrated temperature sensor	103
5.5.1	Experimental methods	103
5.5.2	Design and testing	103
5.5.3	Summary	105
5.6	Main contributions and conclusions	106
6	A wearable system for ion sensing	107
6.1	Optimization of platform design and wells	107
6.2	Optimization of the fluidic system	109
6.3	Tests with portable read-out electronics	113
6.4	Testing of the whole system in artificial and in real sweat	116
6.4.1	A wearable electrochemical sensing system for lithium monitoring	117
6.4.2	Wearable multi-sensing platform for ion sensing in sweat	118
6.4.3	Test on human volunteers	120
6.5	Main contributions and conclusions	122
7	Conclusions and future work	123

Indice

Bibliography	127
Curriculum Vitae	139

Elenco delle figure

1.1	Possible responses of different patients to the same pharmacological treatment.	2
1.2	Efficacy rates of several drug treatments. Reprinted with permission from [1]	3
1.3	A brief historic timeline of wearables.	4
1.4	The total wearable device shipment and revenue in the world market from 2016 to 2022. (source Tractica, 2017)	5
1.5	a) Distribution of eccrine sweat glands in the human body (glands/CM ²). b) Concentration ranges of different sweat analytes. Reprinted with permission from [2].	6
1.6	a) Cross section of the skin around a sweat gland. b) Structure of a sweat gland. c) Ionic flow in the ductal and coil regions of a sweat gland. Reprinted with permission from [2].	7
1.7	Partition pathway of different chemical species from interstitial fluid and blood into sweat. Reprinted with permission from [3].	7
1.8	Examples of applications of ion-sensors in different fields.	10
2.1	(a) Structure and working principle of conventional ISEs. (b) Electrochemical setup for potentiometric measurements using conventional ISEs. (c) Typical calibration curve of a potentiometric ISE.	16
2.2	Potential profile within a cell containing a conventional ISE and a liquid junction RE. The RE bridge consists of a reference electrolyte solution separated from the sample solution by a porous frit.	17
2.3	Structure and working principle of ISEs with SCs based on conductive polymers.	19
2.4	Structure and working principle of ISEs with SCs based on nanostructured SCs.	19
2.5	Determination of upper and lower LOD according to IUPAC definition.	21
2.6	Ion fluxes and typical potential profile during a water layer test for evaluating ISEs potential drift.	22
2.7	CRC curves with and without nanostructured SCs. The behaviour of gold and platinum nanostructures are compared.	23

Elenco delle figure

2.8	Calibration curves of ISE with different selectivity coefficients. A smaller selectivity coefficient gives lower interference.	25
2.9	Fabrication and testing of paper-based disposable ISEs. Reprinted with permission from [4]. Copyright (2012) American Chemical Society	27
2.10	Fabrication of the CNT-cotton sensing electrodes: (a) bare cotton yarn, (b) dyeing with CNT inks, (c) shielding with a pipette tip, and (d) dip coating into the membrane cocktail. (e) Schematic of the prototype electrode: (I) connection of the CNT yarn to a measuring device, (II) pipette tip (shield), and (III) membrane coated CNT yarn end. Reprinted with permission from [5].	28
2.11	a) Picture of the tattoo pH potentiometric sensor illustrating the two electrodes and the connection points for the voltmeter. Reprinted with permission from [6]. b) Scheme of the structure of a NH_4^+ sensing tattoo ISE. Reprinted with permission from [7].	29
2.12	a) Fully integrated wearable band for perspiration analysis. Reprinted with permission from [8]. b) Wearable sweatband based on gold nanodendrites for sodium sensing. Reprinted with permission from [9]. Copyright (2017) American Chemical Society	30
3.1	a) Scheme of the fabricated nanostructures-based SC-ISEs. b) SEM cross-sectional view of a Li^+ ISE with platinum nanoflowers as SC. Reprinted with permission from [10].	34
3.2	SEM images of Pt/PtNanoflowers and Au/AuNanocorals SCs at different fabrication steps for: bare electrodes (a-b); electrodes after nanostructuring (c-d). Reprinted with permission from [10].	35
3.3	SEM images of a Pt/PtNanoflowers/ISM before (a) and after (b) the electrochemical measurements. Reprinted with permission from [10].	36
3.4	SEM images of a Au/AuNanocorals/ISM before (a) and after (b) the electrochemical measurements. Reprinted with permission from [10].	36
3.5	CRC measurements of all-solid-state Li^+ ISEs on platinum (a) and gold (b) substrates showing the significant improvement in potential stability when nanostructured SCs are used. (± 5 nA for 60 s in 0.01 M LiCl solution) Reprinted with permission from [10].	37
3.6	CRC comparison of different stacks of nanostructured Li^+ SC-ISEs. In particular, gold nanocorals and platinum nanoflowers were employed as SCs on both platinum (a) and gold (b) substrates. (± 5 nA for 60 s in 0.01 M LiCl solution) The three curves of the same colours correspond to three different samples of the same type. Reprinted with permission from [10].	38
3.7	Cyclic voltammograms in a 5 mM potassium ferro/ferricyanide solution of: a) Pt, Pt/PtNanoflowers and Pt/AuNanocorals SCs; b) Au, Au/PtNanoflowers and Au/AuNanocorals SCs. It is evident that electrode nanostructuring significantly increases the SC capacitance, as expected. (scan rate 100 mV/s) Reprinted with permission from [10].	40

3.8	Example of potentiometric time traces obtained during the calibration of Li^+ SC-ISEs with (blue curve) and without (black curve) nanostructured SC. The use of platinum nanoflowers provides a much more stable potential response. Reprinted with permission from [10].	40
3.9	Example of a typical calibration curve of Li^+ ISEs with platinum nanoflowers as SCs. Reprinted with permission from [10].	41
3.10	ISM thickness as a function of the ISM cocktail volume drop-casted on the electrode. Reprinted with permission from [10].	42
3.11	a) Reversed calibration of Li^+ ISEs based on platinum nanostructured SCs between 10^{-5} M and 10^{-1} M (the logarithm of the concentration is reported above the corresponding potential step. b) Potential stability over time of two Li^+ ISEs based on platinum nanostructured SCs during immersion in a 3 mM LiCl solution. Reprinted with permission from [10].	43
3.12	SEM images of the proposed (a) AuNanocorals/PtNanoflowers and (b) PtNanoflowers/AuNanocorals SCs for portable and wearable ion-sensing applications. Reprinted with permission from [11]. ©[2018]IEEE	44
3.13	CV measurements of the proposed AuNanocorals/PtNanoflowers (pink curve) and PtNanoflowers/AuNanocorals (green) SCs in comparison with the flat platinum electrode (black) and the previously developed AuNanocorals (orange) and PtNanoflowers (blue) SCs. All voltammograms were obtained in a 5 mM potassium ferro/ferricyanide solution at a scan rate of 100 mV/s. Reprinted with permission from [11]. ©[2018]IEEE	45
3.14	CRC measurements of the proposed AuNanocorals/PtNanoflowers (pink curve) and PtNanoflowers/AuNanocorals (green) SCs in comparison with the flat platinum electrode (black) and the previously developed AuNanocorals (orange) and PtNanoflowers (blue) SCs. All curves were obtained with a Li^+ ISM in a 0.01 M LiCl solution applying a current of ± 5 nA for 60 s. Reprinted with permission from [11]. ©[2018]IEEE	46
3.15	Example of Li^+ calibration curve obtained with a Li^+ ISE based on a AuNanocorals/PtNanoflowers SC. The small inset shows the corresponding time trace. Reprinted with permission from [11]. ©[2018]IEEE	46
3.16	SEM images of platinum nanostructures deposited by LSV with different voltage ranges: between 0 and -0.6 V for the procedures called LSV1 (a), between 0 and -0.8 V for LSV2 (c). The comparisons with the structures obtained with 2 subsequent depositions is given in (b) and (d). Reprinted with permission from [12].	48
3.17	(a) A schematic illustration of the fabrication of the Li^+ ISEs based on the one-step electrodeposition of platinum nanostructures on custom-made evaporated gold micro-electrodes. Their structure and working principle during electrochemical measurements is highlighted in (b). Reprinted with permission from [12].	49

Elenco delle figure

3.18	CRC measurements of the different fabricated Li^+ ISEs on micro-electrodes without platinum nanostructures and with platinum nanoflowers deposited by LSV1 and LSV2. Reprinted with permission from [12].	49
3.19	Calibration time traces of lithium-ISE fabricated on different SCs.	50
3.20	Calibration curve of lithium SC-ISE with platinum nanostructures deposited by LSV2. Reprinted with permission from [12].	51
3.21	Reversed calibration between 10^{-3} and 10^{-1} M of for a Li^+ SC-ISE on micro-electrodes. Platinum nanoflowers were deposited by LSV2. Reprinted with permission from [12].	52
3.22	Calibration traces obtained from the freshly prepared Li^+ SC-ISE (green) and the ones after 40 days of storage in dry (light blue) and then in wet (dark blue) conditions. Platinum nanoflowers were deposited by LSV2. Reprinted with permission from [12].	53
4.1	Scheme of the proposed non-invasive approach for Therapeutic Drug Monitoring (TDM) of lithium in sweat. Reprinted with permission from [13]. ©[2018]IEEE	56
4.2	Calibration curves of Li^+ ISEs based on platinum nanostructured SCs after conditioning at different concentrations: a) long range calibration range (between 10^{-6} M and 0.1 M); b) short range calibration around the therapeutic window values. Reprinted with permission from [10].	59
4.3	Calibration curve of a Li^+ SC-ISE in sweat. The inset shows the corresponding time trace. Adapted with permission from [14]. ©[2018]IEEE	61
4.4	Reversed calibration in the range 10^{-3} – 10^{-1} M of a Li^+ SC-ISE in sweat. Adapted with permission from [14]. ©[2018]IEEE	62
4.5	Sensor stability over time when exposed to sweat with 10 mM NaCl. The two curves correspond to the responses of two distinct electrodes. Adapted with permission from [14]. ©[2018]IEEE	62
4.6	Calibration curve of a Pb^{2+} SC-ISE in aqueous solution. The inset shows the corresponding time trace.	65
4.7	Calibration curve of a Pb^{2+} SC-ISE in sweat. The inset shows the corresponding time trace.	66
4.8	Reversed calibration in the range 10^{-3} – 10^{-1} M of a Pb^{2+} SC-ISE in sweat. . . .	67
4.9	Sensor stability over time when exposed to sweat with 1 mM $\text{Pb}(\text{NO}_3)_2$. The two curves correspond to the responses of two distinct electrodes.	68
4.10	Calibration curve of a K^+ SC-ISE in aqueous solution. The inset shows the corresponding time trace.	71
4.11	Calibration curve of a Na^+ SC-ISE in aqueous. The inset shows the corresponding time trace.	71
4.12	Calibration curve of a K^+ SC-ISE in sweat. The inset shows the corresponding time trace.	73
4.13	Calibration curve of a Na^+ SC-ISE in sweat. The inset shows the corresponding time trace.	74

4.14	Reversed calibration in the range $10^{-3} - 10^{-1}$ M of a K^+ SC-ISE in sweat.	75
4.15	Reversed calibration in the range $10^{-3} - 10^{-1}$ M of a Na^+ SC-ISE in sweat.	75
4.16	Sensor stability over time when exposed to sweat with 10 mM KCl. The two curves correspond to the responses of two distinct electrodes.	76
4.17	Sensor stability over time when exposed to sweat with 10 mM NaCl. The two curves correspond to the responses of two distinct electrodes.	76
5.1	Working principle of a three-electrodes electrochemical cell with nano-biostructures. Reprinted with permission from [15].	80
5.2	Design of the complete wearable electrochemical multi-sensing platform fabricated in this work.	82
5.3	Fabrication steps of the flexible electrochemical multi-sensing platform on a PI substrate.	83
5.4	Cyclic voltammograms of the flexible platinum electrodes in a 5 mM potassium ferro/ferricyanide solution.	91
5.5	SEM image of the platinum nanoflowers deposited on the flexible sensing electrodes.	91
5.6	Effect of bending on the potential response of the flexible Li^+ ISEs.	92
5.7	Different strategies for the fabrication of reference membranes. Reprinted with permission from [16]. ©[2019]IEEE	93
5.8	Example of a calibration of a Li^+ ISE with a all-solid-state RE based on a IL-PVC membrane. The corresponding calibration time trace is given in the small inset. Adapted with permission from [16]. ©[2019]IEEE	96
5.9	Dependence of RE potential at increasing chloride concentrations from 10^{-9} up to 10^{-1} M by subsequent chloride additions every 100s (activity steps of a decade up to 10^{-6} M, half a decade up to 10^{-1} M). The responses of three different samples are reported per each RE type. Reprinted with permission from [16]. ©[2019]IEEE	97
5.10	SEM images of the different reference membranes. Reprinted with permission from [16]. ©[2019]IEEE	98
5.11	Reference membranes potential at different pH. The responses of three different samples are reported per each RE type. Reprinted with permission from [16]. ©[2019]IEEE	98
5.12	Cyclic voltammograms of a gold screen-printed electrode in a 5 mM potassium ferro/ferricyanide solution versus the different REs. Reprinted with permission from [16]. ©[2019]IEEE	99
5.13	Calibration time traces obtained with flexible REs in comparison with a double junction Ag/AgCl electrode. Adapted with permission from [13].	100
5.14	Time stability of an all-solid-state RE based on a IL-PVC membrane. ($LiCl$ 10 mM) ©[2019]IEEE	101

Elenco delle figure

5.15	Li ⁺ calibrations obtained with the flexible electrochemical sensing platform in water (a) and in artificial sweat (b) by subsequent LiCl additions. The flexible all-solid-state RE is used in all measurements. Reprinted with permission from [13]. ©[2019]IEEE	102
5.16	Experimental setup for the resistive measurements on the temperature sensor.	103
5.17	Calibration curve obtained using the extreme values of the current-voltage characteristics of the resistors.	105
5.18	Calibration curve obtained using the mean values of the current-voltage characteristics of the resistors.	105
6.1	Image of the microfabricated flexible platform with smaller pitch (2.54 cm) and smaller electrodes dimension (radius of 500 μm).	108
6.2	Image of the platform wells obtained with the adhesive Kapton tape to avoid intermixing of the membranes cocktails and of the conditioning solutions among neighbouring electrodes.	109
6.3	Fluidic test with fast adsorbing Whatman paper on a lithium-selective electrode: a) scheme of the experimental setup; b) obtained time trace at increasing LiCl concentration.	109
6.4	Fluidic test with fast adsorbing Whatman paper on a lithium-selective electrode: a) scheme of fluidic design and experimental setup; b) obtained time trace while going up and down in LiCl concentration.	110
6.5	Adsorbing tests of fluidic systems fabricated with different materials: a) Whatman paper; b) wound adsorbent patch; c) make-up removing patch. The samples on the left of each picture are using 1 layer for the reservoir, the sample in the middle 2 layers and the one on the right 3.	112
6.6	Comparison of the adsorbing power of different fluidic systems (Whatman paper, make-up removing pads and cotton adsorbent patches).	113
6.7	Test of the final fluidics made with make-up cotton pads while increasing and decreasing lithium concentration. The fluid is drop-cast on one side of the narrow channel in order to simulate the region where the sweat will be produced and soaked.	113
6.8	Different blocks of the potentiometric board: (1) socket for the power supply, (2) Programming/Debugging Interface, (3) UART serial port and alternative power supply, (4) microcontroller unit, (5) Bluetooth module, (6) four-channels potentiometric readout and pH readout circuitry, (7) temperature readout block. Reprinted with permission from [17]. ©[2019]IEEE	114
6.9	Potassium sensor calibration in water background electrolyte. Reprinted with permission from [17]. ©[2019]IEEE	115
6.10	Sodium sensor calibration in water background electrolyte. Reprinted with permission from [17]. ©[2019]IEEE	115

6.11	Different blocks constituting AmpPot board: (1) power supply socket, (2) programming/debugging interface, (3) UART/I2C serial ports, (4) microcontroller unit, (5) Bluetooth module, (6) amperometric readout blocks, (7) potentiometric readout blocks. Reprinted with permission from [18]. ©[2020]IEEE	115
6.12	Lithium sensor calibration in water background electrolyte. Reprinted with permission from [18]. ©[2020]IEEE	116
6.13	Experimental setup to simulate in-situ measurements using our wearable lithium-sensing system. [19]	117
6.14	Comparison between the potential values obtained with the proposed wearable lithium-sensing system with respect to the predicted ones. [19]	118
6.15	Overview of the wearable headband for ion-sensing in sweat: a) different sensing sites available on the flexible electrochemical platform; b) picture of the fabricated flexible electrochemical platform on a PI substrate; c) flexibility of the fabricated electrochemical platform; d) read-out electronics for potentiometric sensors. [20]	119
6.16	Cotton fluidics of the complete wearable headband for ion-sensing in sweat. [20]	119
6.17	Potentiometric response of each electrode of the flexible electrochemical multi-sensing platform during subsequent exposure to 10 mM LiCl, 10 mM NaCl, 10 mM KCl and 10 mM Pb(NO ₃) ₂ in artificial sweat. [20]	120
6.18	Experimental setup used for the testing of the wearable platform on human volunteers.	121
6.19	Potassium and sodium trends in the sweat of a volunteer during 30 minutes of indoor cycling after the perspiration starts. [20]	121
6.20	Scatter plots of potassium and sodium comparing the in-situ and ex-situ measurements in the sweat of a volunteer during 30 minutes of indoor cycling after the perspiration starts. [20]	122

Elenco delle tabelle

3.1	The total resistance, potential drift and capacitance values of the different fabricated Li^+ ISEs have been computed from the CRC measurements. Five samples for each stack sequence were fabricated and tested. Reprinted with permission from [10].	39
3.2	Analytical parameters of Li^+ SC-ISEs based on Pt/PtNanoflowers SCs. Reprinted with permission from [10].	41
3.3	Potential drift and capacitance values obtained from the CRC measurements of the different fabricated Li^+ ISEs on micro-electrodes in comparison with the literature values on macro-electrodes. Reprinted with permission from [12]. . .	50
3.4	Sensor parameters obtained from the calibration curves of the different fabricated Li^+ ISEs on micro-electrodes in comparison with the literature values on macro-electrodes. Reprinted with permission from [12].	51
3.5	Sensor parameters obtained from the calibration traces in Figure 3.22 for the freshly prepared Li^+ SC-ISE and the ones after 40 days of storage in dry and then in wet conditions. Reprinted with permission from [12].	52
4.1	Composition of the artificial perspiration solution used in this work.	58
4.2	Selectivity coefficient of Li^+ ISEs based on platinum nanostructured SCs for different interfering ions obtained by SSM and FIM in comparison with the highest literature values [10].	59
4.3	Analytical parameters in sweat of a Li^+ ISEs based on platinum nanostructured SCs [14].	61
4.4	Effect of conditioning concentration on the analytical parameters of Pb^{2+} SC-ISEs.	66
4.5	Selectivity coefficient of Pb^{2+} ISEs based on platinum nanostructured SCs for different interfering ions obtained by SSM and FIM in comparison with the literature values.	66
4.6	Analytical parameters in artificial sweat of a Pb^{2+} ISEs based on platinum nanostructured SCs.	67

Elenco delle tabelle

4.7	Effect of conditioning concentration on the analytical parameters of K^+ SC-ISEs.	72
4.8	Effect of conditioning concentration on the analytical parameters of Na^+ SC-ISEs.	72
4.9	Selectivity coefficient of K^+ ISEs based on platinum nanostructured SCs for different interfering ions obtained by SSM and FIM in comparison with the literature values.	72
4.10	Selectivity coefficient of Na^+ ISEs based on platinum nanostructured SCs for different interfering ions obtained by SSM and FIM in comparison with the literature values.	73
4.11	Analytical parameters in artificial sweat of a K^+ ISEs based on platinum nanostructured SCs.	74
4.12	Analytical parameters in artificial sweat of a Na^+ ISEs based on platinum nanostructured SCs.	74
5.1	Detailed runcard for the fabrication of the flexible electrochemical multi-sensing platform.	84
5.2	Comparison of sensitivity and LOD values of a Li^+ SC-ISE when the calibration procedure is performed using different all-solid-state REs. The RE membranes were deposited on previously chlorinated silver REs [16].	96
5.3	Analytical parameters of the flexible Li^+ -sensing system in water and in sweat [13]	102
5.4	Electrical resistivity of some metals at 20 °C.	104
6.1	Performance of the developed front-end on the developed lithium ISE [18] . . .	116

List of acronyms

BD	Bipolar Disorder
CRC	Current Reversal Chronopotentiometry
CE	Counter Electrode
CV	Cyclic Voltammetry
DC	Direct Current
EIS	Electrochemical Impedance Spectroscopy
IBE	Ion beam etching
IL	Ionic Liquid
IPA	Isopropanol
ISE	Ion-Selective Electrode
ISM	Ion-Selective Membrane
IUPAC	International Union of Pure and Applied Chemistry
LOD	Limit Of Detection
LOR	Lift-Off Resist
LSV	Linear Sweep Voltammetry
OCP	Open Circuit Potential
OM	Optical Microscope
PI	Polyimide
PR	Photoresist
POC	Point-Of-Care
PVB	Polyvinyl Butyral
PVC	Polyvinyl Chloride
RE	Reference Electrode
RF	Radio Frequency
SC	Solid Contact
SC-ISE	Solid-Contact Ion-Selective Electrode
SEM	Scanning Electron Microscopy
THF	Tetrahydrofuran
WE	Working Electrode

The healthcare revolution

An healthcare revolution that leads to major changes in public health takes place about every 50 years. In the 1870s, the germ theory of diseases, the antiseptic techniques, the advances in anesthesia promoted significant improvements in clinical care, leading, in the following years, to the development of modern hospitals and medicine education. In 1928, the discovery of penicillin boosted the use of medication to treat diseases. In the '70s, the establishment of the Randomized Controlled Trial (RTC) defined the era of evidence-based medicine, as we know it today [21, 22]. The next revolution is happening now, with the advancing of the digital age. The last two decades have seen a huge expansion of the enabling technology, such as the increase of the electronics processing power, the widespread adoption of electronic records, the improvements in analytics and sensing. These advancements empower the collection of enormous amount of information on patients, populations and environments in which we live, laying the foundations for *data-driven healthcare*. This is based on the use of these recorded data to continuously improve the efficacy, quality and inexpensiveness of the medical care.

This work wants to reduce the gap between the new needs of the society and of the medical system, by implementing some efficient solutions for handling and processing of the biological information present in sweat, one of the most promising bodily fluid as a non-invasive alternative to blood. In particular, highly performing ion-sensors for the detection of perspiration electrolytes have been developed for several application, including Therapeutic Drug Monitoring (TDM), tracking of contamination by heavy metals and physical exercise monitoring.

This chapter gives an overview of the reasons and characteristics of this data-driven revolution, with particular focus on the role of sweat and ion sensing. This technology could be applied also in other fields, such as food and agriculture.

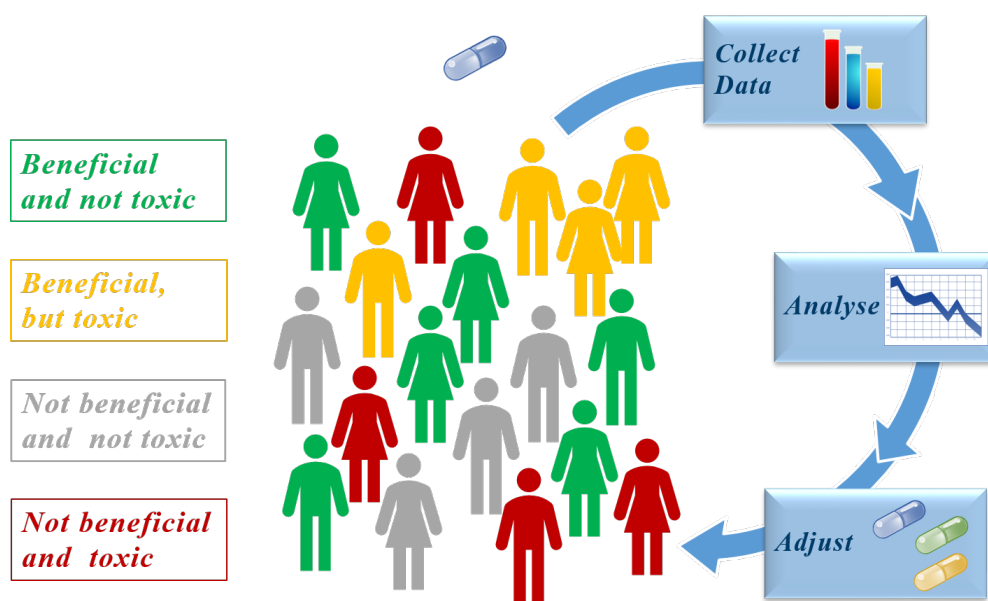


Figure 1.1 – Possible responses of different patients to the same pharmacological treatment.

1.1 Data-driven healthcare: e-Health and personalized medicine.

With the increase of aging population and of chronic diseases world-wide, the concept of traditional medicine is not able to face the new needs of the society and the significant increase of the medical costs. The conventional reactive model of care management is inadequate to address these challenges. New concepts of medicine to deliver cost-effective healthcare both in- and off-hospital are needed. The recent technological advancements represents the key solution to establish a new proactive model that provides medical healthcare and patients monitoring anytime anywhere, linking the hospitals and the external world by the exchange of information. This is typically defined *remote healthcare* or *electronic healthcare (e-Health)* [23].

Remote healthcare can dramatically simplify the acquisition, management and exchange of clinical data and facilitate the necessary controls required by the care protocols without moving the patient and/or the physician. In addition, the emerging data-driven healthcare model of medicine enables the delivery of personalized treatments to the patients, in the so-called *Personalized medicine*. This is a recent branch of medicine that tackles the low efficacy of many pharmacological treatments. In fact, it is now well-known that the response of each individual may vary significantly from person to person even when identical drugs are used. A typical situation is shown in Figure 1.1. The green corresponds to the ideal case, in which the drug is effective without significant side effects. The red case, on the contrary, is the worst scenario, when the drug is not effective and even toxic. In the intermediate cases the drug is simply neither effective nor beneficial or the therapy is effective, but also harmful. These differences can be explained by considering that individuals do not have the same genetic predispositions. This leads to different phenotype level, i.e. different outcomes resulting from

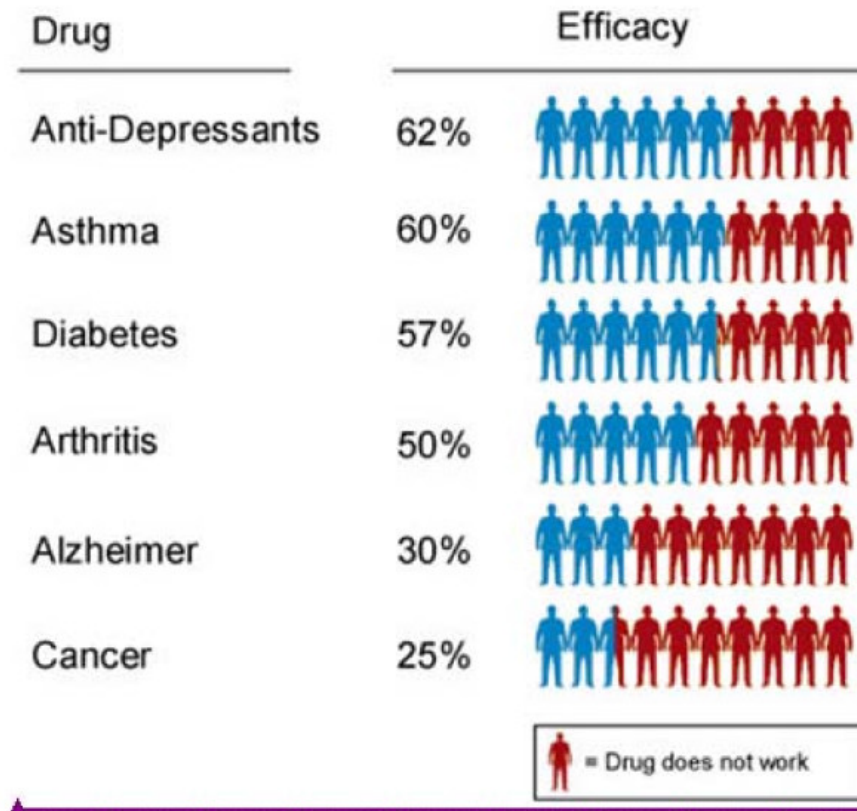


Figura 1.2 – Efficacy rates of several drug treatments. Reprinted with permission from [1]

the interaction of its genetic characteristics with the external environment. In addition, each person differs also in terms of daily metabolism. In other words the reaction of the patient might vary from one day to another.

All these issues explain the low effectiveness of many drug therapies, as reported in 1.2 [1]. It is clear from the low values reported in the graph that personalized therapy can play a significant role in improving healthcare and reducing the costs for ineffective treatments. To implement this new model of medicine, we need innovative systems that are able to monitor several diagnostic parameters at the same time and to correlate them to the supplied treatment, in order to check its adequacy and adjust it if necessary [2, 15, 24]. If in 1900 the global average life expectancy was around 31 years according to the World Health Organization (WHO), this value is expected to rise to 80 by 2030. These advancements in healthcare and innovative technologies can be certainly considered one of the key enablers of these improvements [2].

The development of miniaturized, effective, low-power and cheap technologies has given a major boost to the realization of remote healthcare systems. In fact, several examples have already been reported in several applications in the last twenty years. These include glucose meters, monitoring of heart failures, asthma management, recording of activity of elderly people, physical exercise and heart monitoring [23].

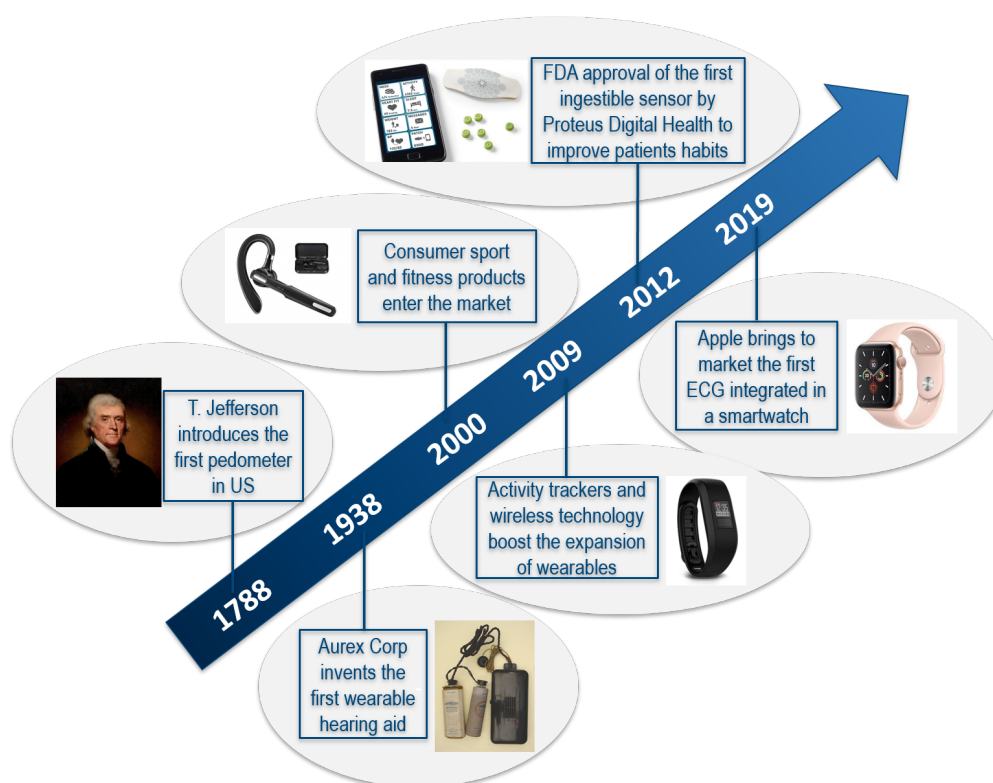


Figura 1.3 – A brief historic timeline of wearables.

It is clear that wearable devices occupy a primary role in e-Health to collect data. With the enormous technological revolution of recent years, also wearables have seen a great expansion. A brief timeline can be found in Figure 1.3. Their rapid spread is confirmed by considering the market value of these systems in terms of shipments and revenues (Fig. 1.4).

Wearables can record various physiological and metabolic parameters at real-time, including heart and respiratory rate, blood pressure, temperature, oxygen saturation (SpO₂), step count, and accidental falling. The collected information is then used to track health metrics, identify physiological anomalies, diagnose disease symptoms at an early stage or develop behavioral models [2].

It is clear from our discussion that there is an enormous interest in developing efficient wearable devices that are able to track in real-time physiological and biochemical signals from individuals. The recent advancements in physical sensors has enabled the commercialization of several electronics products able to measure parameters like activity, heart and respiration rate, posture, as explained before. On the contrary, the progress in wearable chemical sensors did not show the same growth, despite the huge efforts that can be found in literature, because of the inherent challenges in handling and processing bodily fluids.

This thesis attempts to investigate and address some of the challenges related to wearable chemical sensors, with particular interest on sweat sensing. In the next paragraph, a brief

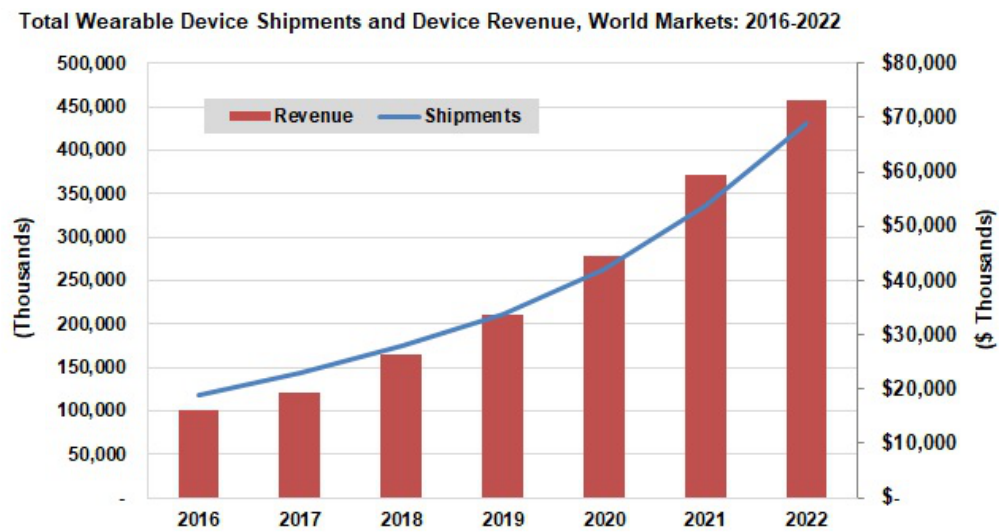


Figura 1.4 – The total wearable device shipment and revenue in the world market from 2016 to 2022. (source Tractica, 2017)

overview of the potential and the increasing interest towards this bodily fluid is given.

1.2 Sweat as alternative biofluid

Sweat, or perspiration, is a thermoregulating response of our body. Every human produces about 500 to 700 ml of sweat per day under most climate conditions [3].

Sweat offers some exclusive promising characteristics as alternative to the more used blood. In fact, it is readily accessible and reproducible in the laboratory, it does not require invasive procedures like blood collection, it contains several recognized biomarkers (electrolytes and metabolites) with diagnostic capabilities and good correlation with blood values, and it can be easily monitored continuously [25, 26].

1.2.1 Sweat production by eccrine glands

Sweat can be produced in several parts of our body, including chest, palm, forehead and sole. Sweat glands play a significant role in the secretion of perspiration, thus in the thermoregulation of the individual. In general, sweat glands are present in most regions of the human body, but they are concentrated more in certain parts [2].

There are primarily two types of sweat glands: apocrine and eccrine. The second ones are present in larger number, with higher concentration under the feet, in the palms and in the forehead. The distribution of eccrine sweat gland in the human body is reported in Figure 1.5 [2].

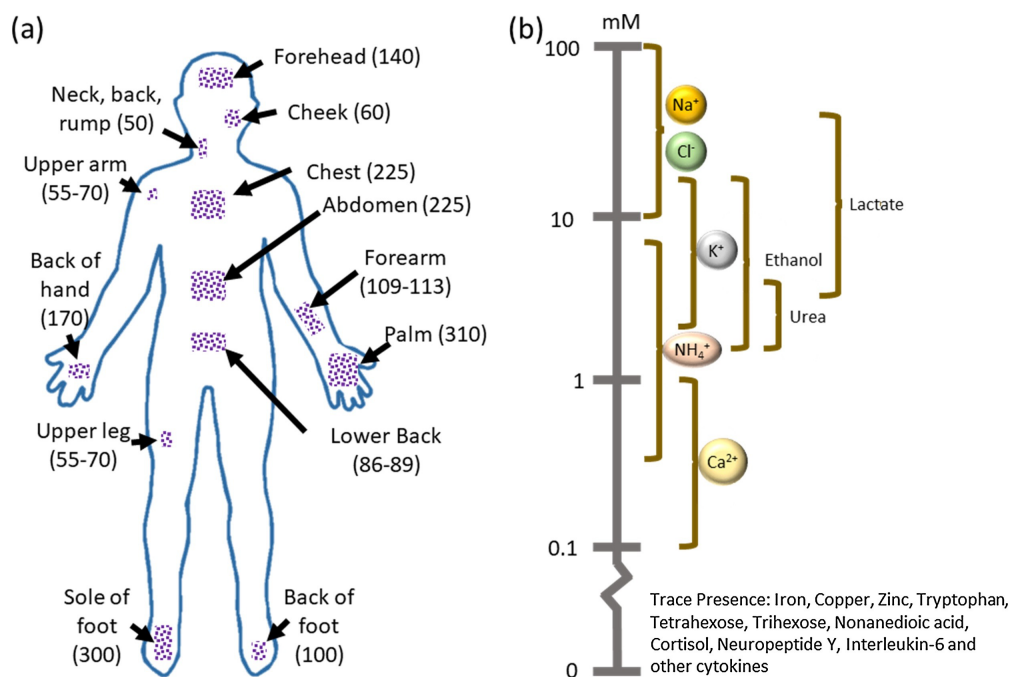


Figura 1.5 – a) Distribution of eccrine sweat glands in the human body (glands/CM²). b) Concentration ranges of different sweat analytes. Reprinted with permission from [2].

Eccrine sweat glands opens on the skin surface (Fig. 1.6a). Eccrine sweat is typically composed of water mixed with products originating from the blood, such as urea, sodium chloride, immunoglobulins and proteins. It is odorless. On the contrary apocrine sweat glands are typically located within hair follicles in private areas of the human body. They can activate with stress, emotions or high levels of adrenaline [2].

It is evident that eccrine sweat glands are the ones of interest for wearable applications. Thus, it is important to understand their structure and method of secretion of perspiration. Each gland consists of a secretory coil and a thermal duct (Fig. 1.6a-b). The secretory coil falls in the dermis. It attracts water to oppose the osmotic gradient generated by sodium and chloride ions that are actively transferred into it. The hydrostatic pressure will then bring the fluid to the skin surface, where the sweat is secreted. During the whole process several compounds can enter the perspiration both through the secretory coil and the thermal duct. These include hormones, metabolites, ions, acids, peptides and small proteins (Fig. 1.6c) [2].

It is hypothesized that many compounds found in sweat are the result of passive or active transport from the adjacent interstitial fluid and blood vessels, thus explaining the affinity among analytes in these bodily fluids [2]. Despite this similarity, the medical relevance of many of those analytes is still unproven as the correlation with the blood values must be better understood. The possible mechanism of transfer of the chemical compounds are illustrated in Figure 1.7. Small lipophilic (hydrophobic) analytes show strong sweat-blood correlation values as they partition transcellularly through the lipophilic cell membrane. Among these chemical

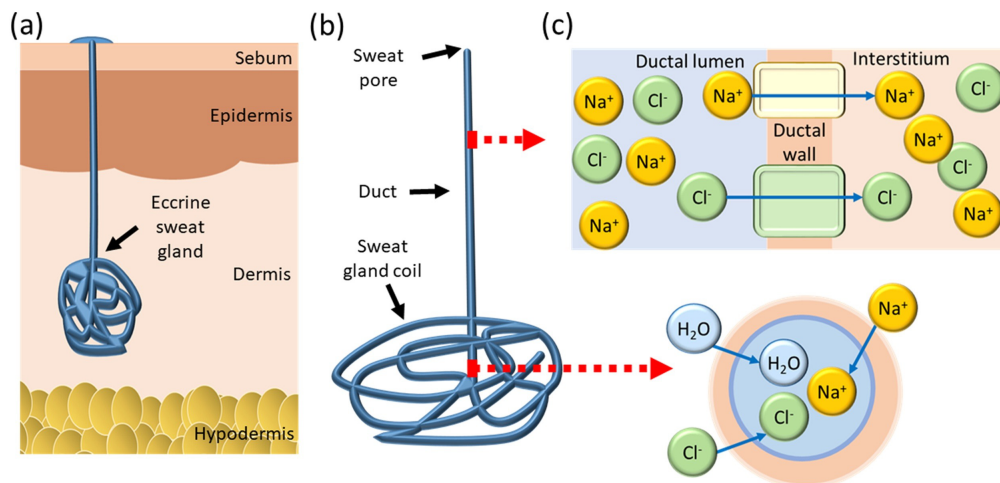


Figure 1.6 – a) Cross section of the skin around a sweat gland. b) Structure of a sweat gland. c) Ionic flow in the ductal and coil regions of a sweat gland. Reprinted with permission from [2].

species we have steroid hormones (cortisol, testosterone) and drugs (levodopa, ethanol, methylxanthine). On the contrary, larger compounds are supposed to enter in sweat through a paracellular route active channels or exosomes which affect the correlation between the two body fluids [3].

It is clear that the level of filtering in tight junctions is higher, due to the greater number of cellular barriers. Sweat glucose well represents this phenomenon: it is about 100 times more diluted with respect to the corresponding values in blood or interstitial fluid as it is transported via a paracellular route. This effect represents naturally a big challenge in the field of biosensors, where highly sensitive and selective systems are required.

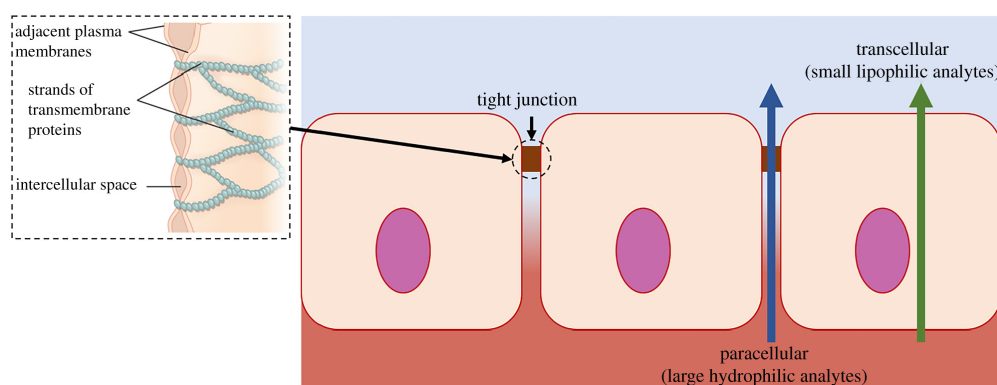


Figure 1.7 – Partition pathway of different chemical species from interstitial fluid and blood into sweat. Reprinted with permission from [3].

1.2.2 Comparison with other bodily fluids

Blood, followed by urine in some cases, is the gold standard in order to determine the concentration of chemical compounds. However, its collection is invasive and requires in most cases qualified personnel. In addition, it is not suitable for continuous monitoring. Among the already mentioned sweat, other possible alternatives are saliva, interstitial fluid and tears. Each of them shows some major limitations with respect to sweat. On-demand and continuous monitoring of tears is critical as the current tear collection protocols generate eye irritation and stimulate the production of reflex tears that interfere with the readings. Sensing in saliva is very challenging during everyday life as the concentration is strongly dependent on the most recent drinks or food consumed by the individual. Furthermore, plaques and bacteria coming from the food might attach on the sensor surface, thus compromising the efficiency of the system. Finally, microneedles or under-the-skin excitation currents are needed to take out interstitial fluid. These methods can be irritating and uncomfortable for the dermis, especially during prolonged monitoring [2, 25].

1.2.3 Main applications area

Sweat contains in general electrolytes (i.e. sodium, potassium, magnesium, chloride, calcium), organic compounds (e.g. urea, ammonia, ethanol, lactate), metabolites and trace compounds (e.g. zinc, iron, tryptophan, interleukin 6). The typical concentration rate in sweat are reported in Figure 1.5b [2].

A lot of research is currently going on sweat test as a potential candidate to substitute blood analysis [25, 27, 28]. In fact, the academic publishing over the last 5-years has seen a 10-fold increase in this area. Both ions and other metabolites have been used as sweat biomarkers for different purposes. Electrochemistry is the most investigated sensing method because of the good sensitivity, small sample volume, low cost, simple design, easy integration into microfabrication processes for large-scale production and straightforward signal interpretation.

Sweat biomarkers can be exploited to detect the genetic predisposition to diseases like cystic fibrosis in infants by measuring the level of chlorides and to determine other related conditions. Furthermore, a deeper understanding of the glucose correlation with blood values has been studied recently to allow continuous monitoring of diabetes. Lactate and ammonia are related to the shift from aerobic to anaerobic metabolic conditions. Ischaemia can be related to lactate concentration. Urea and creatinine might indicate renal dysfunction. Cortisol provides an indication of stress levels. Iron and copper concentration might be used to monitor sports anemia. Skin temperature and pH can be used to obtain insights on several skin injuries and diseases [2, 3].

The most prominent examples of wearable systems are the fully integrated sweat band described in Nature [8] and the RFID sensor patch for sodium monitoring that appeared in IEEE

Spectrum [29]. However, also colorimetric [30] and other sensing techniques are used. For more detailed reviews on this topic please refer to [25, 27, 28].

Some of these devices are now also commercially available for applications in different fields. The most important case in the field of sweat diagnosis is the one of chlorides testing to diagnose Cystic Fibrosis (CF) by means of coulometric titration (ChloroCheck®), osmolality (Wescor Vapro® Vapor Pressure osmometer) or conductivity (Sweat Chek™ Analyzer) measurements.

1.2.4 Challenges

Despite the great research efforts and the large amount of biological information, current biosensors still have to address several unsolved issues, such as poor collection, separate sampling and analysis, low multi-sensing capabilities and lack of data correlating sweat and blood values. Progress in materials science to enhance selectivity, detection range and stability is also needed. With the recent advancements in sensing integration and in wearable technologies, some challenges are beginning to be tackled, but there is still large room for improvement [3].

One of the main current limitations towards the widespread use of sweat wearable technologies is the small amount of sweat produced in sedentary individuals and the lack of proper techniques for sweat stimulation. A volume of about 20-200 μL is necessary to obtain stable potential readings. Currently there are mainly two methods for sweat stimulation: passive production (e.g. physical exercise or sauna) and electrical stimulation (iontophoresis) with the aid of pilocarpine.

Our wearable platform will tackle some of these challenges, enabling the monitoring of several ions for different applications: Li^+ for Therapeutic Drug Monitoring (TDM) of people affected by psychiatric disorders, Pb^{2+} for controlling heavy metal contamination, K^+ and Na^+ for tracking of physical exercise.

1.3 Importance of ion-sensing

This work focuses mainly on the development of ion-sensors for healthcare applications. As discussed in the previous paragraphs and as will be explained in more details also in Chapter 4, electrolytes provide significant information on patient's health. This includes the monitoring of physical exercise (Na^+ and K^+), heavy metal contamination (Pb^{2+} , As^{2+}), TDM (Li^+).

However, ion sensors find application in several different fields outside healthcare, like food and water quality monitoring, industrial control, agriculture and fishery (Fig. 1.8). The same technology developed in this work might be easily extended to other functions outside medical care. As most of the times these fields involve water solutions, interference effects are expected to be much lower than in bodily fluids, thus facilitating the sensing. *Ion-selective electrodes* (ISEs) can be used in a wide variety of applications for determining the concentrations of



Figura 1.8 – Examples of applications of ion-sensors in different fields.

various ions in aqueous solutions. The following is a list of some of the main areas in which ion sensors have been used.

- Pollution Monitoring: CN, F, S, Cl, NO₃ etc., in effluents, and natural waters.
- Agriculture: NO₃, Cl, NH₄, K, Ca, I, CN in soils, plant material, fertilisers and feedstuffs.
- Food Processing: NO₃, NO₂ in meat preservatives.
- Salt content of meat, fish, dairy products, fruit juices, brewing solutions.
- F in drinking water and other drinks.
- Ca in dairy products and beer.
- K in fruit juices and wine making.
- Corrosive effect of NO₃ in canned foods.
- Detergent Manufacture: Ca, Ba, F for studying effects on water quality.
- Paper Manufacture: S and Cl in pulping and recovery-cycle liquors.
- Explosives: F, Cl, NO₃ in explosive materials and combustion products.
- Electroplating: F and Cl in etching baths; S in anodising baths.
- Biomedical Laboratories: Ca, K, Cl in body fluids (blood, plasma, serum, sweat).
- F in skeletal and dental studies.

In this work the detection of ions is based on the use of ISEs. Their structure and functioning will be illustrated in detail in Chapter 2. ISEs represent the largest part of current ion sensors. This can be explained by considering that fast and non-expensive measurements are possible with these devices. In addition, low maintenance is needed. Finally, a major reason behind their success is related to the demand, as the determination of electrolytes is most frequently performed by clinical analysis, with a market of more than 10 billion US \$/year. In fact, ISE membranes are available for most of the clinically relevant ions, with characteristics that perfectly meet the medical requirements. Other techniques with respect to ISEs have also been investigated for ion-sensing ([31]). These include especially optical sensors, in particular luminescent ([32]) and colorimetric ([33, 34]) detection of ions. These require more elaborate and larger system implementations.

1.4 Research contributions

In the era of data-driven healthcare, the realization of fully integrated wearable systems for analyses of electrolytes and metabolites is still far from trivial. In principle, we need systems capable of sensing several compounds, using small sample volume without losing their performance. In this regard, electrochemical sensors offer some significant advantages because of the inexpensive and reproducible fabrication procedures, the possibility of miniaturization and the simplicity of the read-out. A continuous challenge in the field of electrochemical medical sensors is the reproducible detection of organic compounds and ions in the physio-pathological concentration range, avoiding problems of interference.

This thesis aims at addressing some of the unresolved issues in this field, with particular focus on the detection of ions in sweat, as we explained previously the exceptional advantages of this bodily fluid. The main contributions are summarized below.

- The realization of highly stable and highly reproducible *Solid-Contact Ion-Selective Electrodes* (SC-ISEs) for efficient detection of ions based on fast electrodepositions of noble metal nanostructures (less than 4 minutes).
- The realization of a flexible electrochemical multi-sensing platform to be integrated in a wearable system. This includes a flexible all-solid-state *Reference Electrode* (RE) and a low-cost paper fluidics.
- The successful testing of the integrated wearable headband for the detection for the first time of lithium for *Therapeutic Drug Monitoring* (TDM) of people affected by *Bipolar Disorder* BD in sweat.
- The successful testing of the integrated wearable headband for the monitoring for the first time of heavy metal contamination (in particular lead detection) in sweat in people exposed to risky environments.

- The validation of the wearable headband on real human subjects for detection of potassium and sodium during physical exercise.

1.5 Thesis outline

The thesis outline is reported below.

Chapter 1 has given an overview of the data-driven healthcare revolution, explaining the need for efficient wearable systems and the potential of sweat sensing in this sense.

Chapter 2 gives a detailed background on the basic principles and applications of potentiometric ion-sensors, with particular focus on the effort to develop all-solid-state ISEs for miniaturized and wearable applications.

Chapter 3 describes our work on the development of exceptionally stable all-solid state ISEs suitable for portable and wearable applications based on fast electrodeposition of noble metal nanostructures.

Chapter 4 shows the application of the developed *Solid-Contact* (SC) technology in sweat sensing for healthcare applications. In particular, the detection of lithium levels for Therapeutic Drug Monitoring in psychiatric disorders and the monitoring of heavy metal contamination in sweat in risky environments are proposed for the first time.

Chapter 5 presents the fabrication of a flexible electrochemical multi-sensing platform by microfabrication techniques and the realization of stable all-solid-state REs.

Chapter 6 describes the optimization of the design of the flexible platform and the integration with an efficient paper fluidics to ensure fresh sweat on the sensors surface. The validation of the complete system is also presented in a simulated wearable setup as well as in real human volunteers during physical exercise.

Chapter 7 concludes the thesis. It provides a brief summary of the main achievements of this work in the field of wearable sensors. Considering the accomplished objectives, some perspectives on the future work are also discussed.

This chapter gives some background on the basic principles and applications of potentiometric ion-sensors. These systems exploit *Ion-Selective Membranes* (ISMs) to efficiently detect the target ion in solution by means of *Open Circuit Potential* (OCP) measurements. They are widely used for several applications thanks to their high accuracy and simple detection principle. However, conventional ISEs are based on bulky liquid-junctions. Consequently, the research has tried in the last decades to create efficient and miniaturized all-solid-state ISEs, suitable for portable and wearable applications. This chapter aims to describe the working principle and the main limitations of ISEs, with particular focus on the recent interest in SC-ISEs for remote monitoring systems.

First, the structure and working principle of conventional liquid-junction ISEs is described. Secondly, we explain the main criteria to evaluate their performance. Thirdly, the motivations behind the recent effort to develop all-solid-state ISEs for portable and wearable applications are discussed. Finally, the current challenges and future perspectives of this technology are highlighted.

2.1 The main advantages of ISEs

Ion-sensors are one of the most used chemical detection systems with applicability in many different fields, as described in the previous chapter. Medical analysis accounts certainly for one of the biggest portions of those applications. So far, the most efficient and precise ion-sensing devices employ electrochemical measurements based on ISEs [35]. These are based on the deposition on the sensor surface of an ISM that contains a species, called ionophore, that selectively binds to the target ion. Higher ion concentrations in solution will result in larger amounts of ions in the ISM. This in turn will produce a measurable and proportional Open Circuit Potential with respect to a stable *Reference Electrode* (RE).

Potentiometric ion sensors offer several advantages including the relative simplicity of the

OCP measurements and the low cost. For these reasons they are ideal candidates for a variety of applications. A wide concentration range can be measured with these systems, making them very flexible to the user's needs. Both cations and anions can be detected. The working temperature range is wide.

They are particularly useful in biological and medical applications as they measure directly the activity of the ion, rather than its concentration. With careful use, accuracy and precision levels of 2-3 % can be achieved for some ions. This performance is comparable to the most specialized analytical techniques, which require complex and expensive instrumentation.

In addition, it is possible to mass produce arrays of miniaturized sensors for simultaneous analysis of cations and anions mixtures, with possibilities of easy and compact integration.

Moreover, the measurements do not require high voltages as in capillary electrophoresis. Finally, the direct correlation between the measured potential and ion activity suggests the absence of a scaling law and of signal reduction with reduced electrode dimensions [36–38].

2.2 Ion activity and activity coefficients

In order to understand the theory behind the definitions of the most important analytical parameters of ISEs, it is crucial to have some background on some basic thermodynamic notions. This section introduces the concepts of thermodynamic activity of an analyte and of single ion activity coefficient. In addition, the mean activity coefficient and the ionic strength of a solution are also defined.

The activity describes the effective concentration of a solution. The equilibria in ionic solutions depend on the ion activities. The activity of an ion a_j in solution is proportional to its molar concentration c_j according to the following equation [39]:

$$a_j = \gamma_j c_j \quad (2.1)$$

where γ is the single ion activity coefficient. Its value cannot be obtained experimentally. However, the single ion activity coefficient for anions γ_- or cations γ_+ can be calculated in most practical cases from the mean activity coefficient of the solution γ_{\pm} . This is defined as follows:

$$\log \gamma_{\pm} = \frac{|z_-|}{|z_+| + |z_-|} \log \gamma_+ + \frac{|z_+|}{|z_+| + |z_-|} \log \gamma_- \quad (2.2)$$

where z_+ and z_- are the valences of the cations and anions, respectively. The splitting of the mean activity coefficient into the relevant single ion activity coefficients can be done using different conventions. The hydration theory of Stokes, Robinson and Bates gives the most accurate results. However, in ordinary analytical procedure, the simplified Debye-Hückel

convention [39] is sufficient for the purpose:

$$\log \gamma_+ = \left| \frac{z_+}{z_-} \right| \log \gamma_{\pm} \quad (2.3)$$

$$\log \gamma_- = \left| \frac{z_-}{z_+} \right| \log \gamma_{\pm} \quad (2.4)$$

The value of the mean activity coefficient γ_{\pm} can be computed in most cases using the extended Debye-Hückel equation[39]:

$$\log \gamma_{\pm} = -\frac{A |z_+ z_-| \sqrt{I}}{1 + B \sqrt{I}} + CI. \quad (2.5)$$

This is a semiempirical relationship. A is a parameter ($A=0.5108$) that varies with temperature in Kelvin as $\propto T^{-3/2}$. B and C are fittable parameters that depend on the electrolyte. I is the ionic strength of the solution defined as:

$$I = 0.5 \sum_j z_j^2 c_j \quad (2.6)$$

A list of experimental values of B and C is reported in [40].

2.3 Structure and working principle of ISEs

The structure and working principle of conventional ISE is shown in Figure 2.1a. It can be observed that they are macroscopic systems. An ISM is used to separate an inner filling solution with constant Cl^- concentration from the sample solution. The ISM allows the flow and entrapment of only one specific ion through it. Such selectivity of the ISM is ensured by the presence of an ionophore, that is a neutral species that selectively binds to the target ion M^+ .

Typical membrane cocktails include 1-2% of ionophore, 60-70% of plasticizer and 30-40 % of high molecular weight *PolyVinyl Chloride* (PVC). The polymeric matrix gives mechanical stability and should be chemically inert. The plasticizer increases the free volume of the polymeric materials, thus improving mobility, flexibility and durability. Commonly used plasticizers are bis(2-ethylhexyl)sebacate (DOS) or ortho-nitrophenyl octyl ether (o-NPOE). In order to ensure Nernstian behaviour, small amounts of lipophilic ions are added to avoid the extraction of a large amount of counterions from the sample solution to the ISM. In other words, the membrane should be exclusively permeable to ions of the same sign of the target ion (Donnan exclusion). Tetraphenylborates are typically used for this purpose in cation-selective ISM, whereas tetraalkylammonium salts are often employed for anion-selective membranes [35, 41, 42].

If the concentrations of the ions in the inner and the sample solution are not equal, a potential

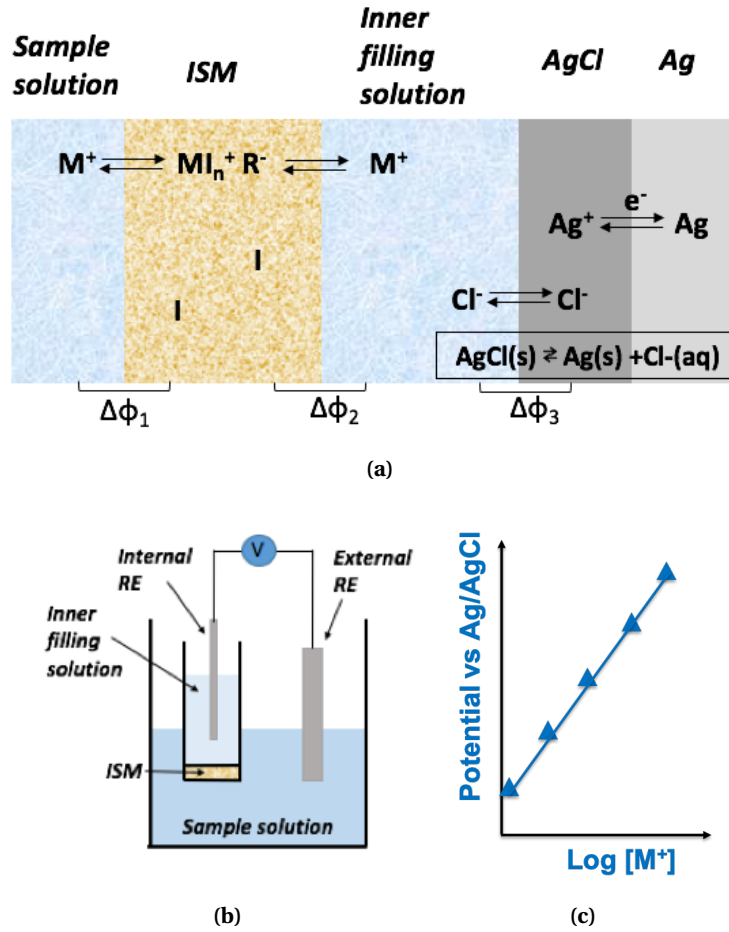


Figura 2.1 – (a) Structure and working principle of conventional ISEs. (b) Electrochemical setup for potentiometric measurements using conventional ISEs. (c) Typical calibration curve of a potentiometric ISE.

difference is generated across the membrane due to ions exchange and accumulation in the ISM. It is possible to predict the activity, i.e. the concentration, of the target ion in solution by measuring the OCP of this kind of *Working Electrode* (WE) with respect to a stable RE. In particular, by keeping constant the activity of the target ion in the internal solution a_A , Nernst equation can be employed to determine the unknown activity on the other side of the membrane a_x :

$$E = \frac{RT}{z_A F} \ln\left(\frac{a_x}{a_A}\right) = \text{const} + 2.3 \frac{RT}{z_A F} \log a_x \quad (2.7)$$

where R is the general gas constant, T the temperature, z_A the valence of the target ion and F Faraday's constant. The internal filling solution acts as a liquid contact that ensures ion-to-electron transduction thanks to the reaction $AgCl(s) \rightarrow Ag(s) + Cl^-(aq)$ and consequent

definition of the interfacial potential $\Delta\phi_3$. It is important to notice that ISEs can detect free, not complex, ion concentrations [35, 36, 43, 44].

It is evident from Figure 2.1b that the ISEs are typically measured in a two-electrodes setup, where the ISE acts as the cathode and the RE as the anode. The measured potential difference is the sum of all potential differences in the cell (Figure 2.2). Consequently, it is crucial to keep all potentials independent of sample solution, except the one at the interface sample/membrane [35].

By definition, the calibration curve is the plot showing how the output signal of the sensor varies as a function of the analyte concentration. Using Equation 2.7, it is possible to observe that a linear relationship is found, in principle, in potentiometric ISEs when the potential is plotted with respect to the log of the concentration. An example of a typical calibration curve for this type of sensors is given in Figure 2.1c.

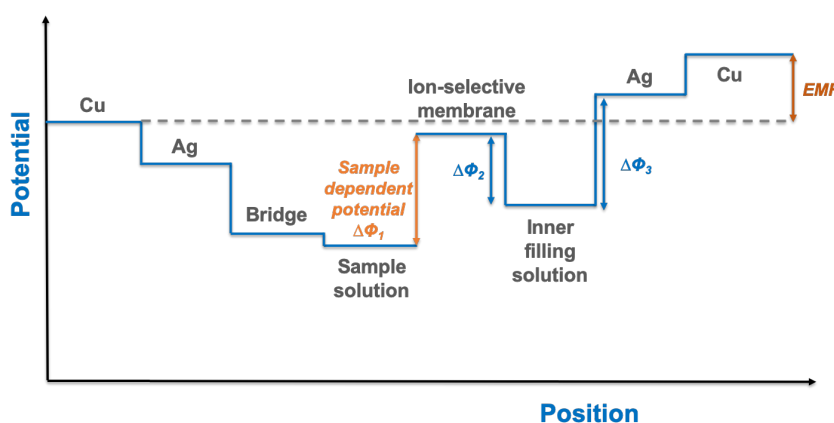


Figure 2.2 – Potential profile within a cell containing a conventional ISE and a liquid junction RE. The RE bridge consists of a reference electrolyte solution separated from the sample solution by a porous frit.

It is clear that the slope of the calibration curve, that is $\frac{RT}{z_A F}$, represents the sensitivity of the sensor S . By simple calculations, it is possible to prove that $S = 59.16/z_A$ at ambient temperature. The sensitivity of potentiometric sensor is mainly dependent on the ions charge z . Monovalent cations will have a calibration slope of 59 mV/decade, which means that a 10-fold concentration will cause a change of 59 mV in the measured potential. On the contrary, the divalent cations will generate a calibration curve with a slope of 29.6 mV/decade. The same reasoning is valid for anions, but in this case negative potential changes will be observed.

2.4 Towards all-solid-state ISEs

Nowadays clinical analysis constitutes the largest area of routine application of ISEs thanks to the availability of accurate ISMs for the most clinically relevant ions (Cl^- , Na^+ , K^+ , Ca^{+2} ,

H^+), large demand and low production costs. Conventional ISEs are very accurate, with small potential drift and long lifetime [35, 36]. However, the internal electrolyte of ISEs is prone to evaporation and highly sensitive to temperature and pressure variations that can lead to large volume changes and eventually to delamination. Moreover, and most importantly, the filling solution limits the reproducible miniaturization of these systems because of the difficult trapping of the solution inside the electrodes. This drawback prevents their miniaturization and applicability for Lab-On-a-Chip (LOC) devices. These systems are portable single chips able to perform complex and time-consuming laboratory operations. Their number is continuously increasing in recent years. Therefore, over the past 50 years several all-solid-state potentiometric ion-sensors have been implemented towards next-generation portable and miniaturized ion-sensing devices integrated with steering circuits and read-out electronics [35]. These ISEs exploit SCs between the ISM and the electronic conductive substrate to achieve ion-to-electron transduction: a properly designed ISM is deposited on top of a metal electrode to attract selectively the target ions close to the surface; the change in charge distribution due to the accumulation of ions at the electrode surface is detected by simply measuring the OCP with respect to the RE. Different ions-to-electron transduction mechanisms are possible [35, 36, 43, 44].

The first all solid-state ISE was proposed in 1970 by Hirata and Date [45], followed by another one proposed by Cattrall et al. [46] the year after. Both systems were based on coated-wire electrodes. Poor reliability was achieved mainly because of the purely capacitive interface and of the reduced interfacial contact area. Since then, several advances have been made thanks to the use of new SC materials and to better understanding of transport phenomena and water accumulation in the membrane. In particular, the most promising candidates for commercial SC ISEs are conductive polymers and nanostructures with high double layer capacitance. These two classes of materials exploit different ion-to-electron transduction mechanisms [41, 47–49]. The next two paragraphs describes their working principle and main characteristics.

2.4.1 Solid contacts based on conductive polymers

Conductive polymers are often used as SCs for ISEs because they are able to conduct both electrons and ions when properly doped, hence they can be used as effective ion-to-electron transducers through redox reactions (Figure 2.3). Polypyrrole [50], poly(3,4-ethylenedioxythiophene) (PEDOT) [51], polyaniline [52] and poly(3-octylthiophene) (POT) [53] are nowadays the most studied conductive polymers for applications in all solid-state ISEs. They are typically deposited by electropolymerization or drop casting from polymeric solutions. The first three polymers are highly stable and possess large conductivity and redox capacitance. However, their electro-activity shows off in a wide range of potentials that can cause several side reactions and consequent drift of the potential response. In addition, the redox potential can be greatly influenced by the crystallinity degree, doping effect on the glass transition temperature and film morphology. On the contrary, POT participates much less in side reactions, but has a

much lower conductivity and redox capacitance [35, 43].

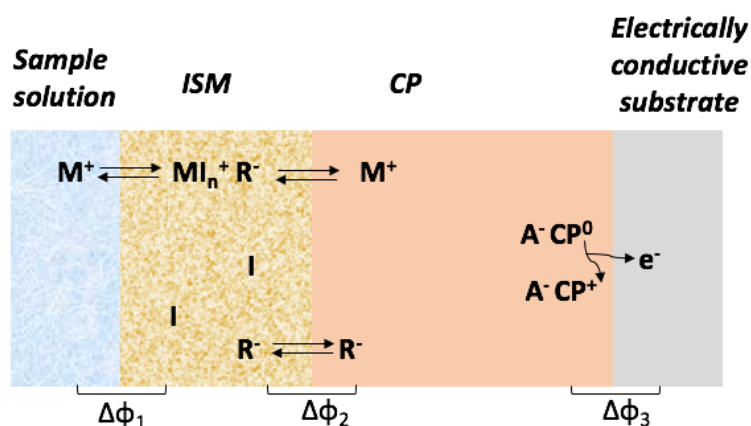


Figura 2.3 – Structure and working principle of ISEs with SCs based on conductive polymers.

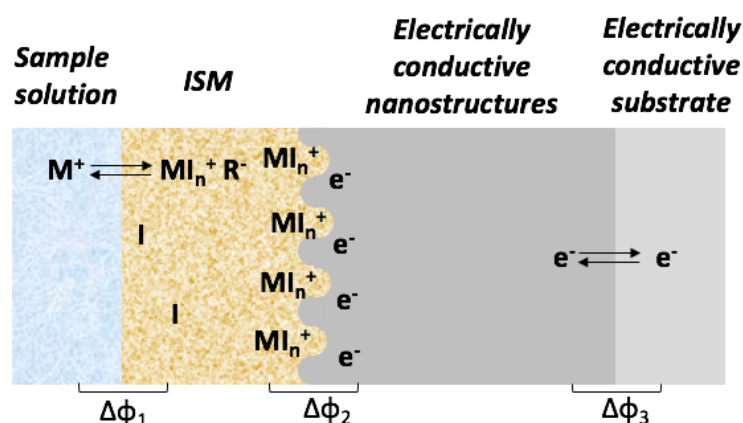


Figura 2.4 – Structure and working principle of ISEs with SCs based on nanostructured SCs.

2.4.2 Solid contacts based on nanostructured layers

Nanostructured materials exploit the formation of an electrical double layer at the membrane/electrode interface for ion-to-electron transduction: the accumulation of ions on one side of the interface thanks to the role of the ISM induces the accumulation of electrons and holes on the other side; this leads to the formation of an asymmetric capacitor. In these systems the interfacial potential is not related to redox reactions, as in the case of conductive polymers, or to ion partitioning, as in conventional ISEs, but to the amount of charge accumulated in the double layer, leading to the potential different $\Delta\Phi_2$ (Figure 2.4). Thanks to their large surface area, nanostructured materials enable the achievement of good adhesion, avoiding the risk of water absorption, and are typically characterized by high capacitance values. This property is

crucial to reduce polarization effects due to the small but non-zero currents required for the measurement. For more details on these considerations, refer to Section 3.3. Both carbon and noble metals nanostructures have been successfully investigated so far in literature for ISEs *Solid Contacts* (SCs) [35, 42, 54–60]. In this work, the superior properties of electrodeposited nanostructured layers of noble metals in ion sensing is demonstrated.

2.5 Performance evaluation criteria of ISEs

The design and the development of a sensor strongly depends on the requirements of the final application. The most important parameters in a sensing system are:

- Selectivity - ability to measure the concentration of a substance in presence of other interfering substances
- Sensitivity - ability to discriminate small variations of the analyte concentration
- *Limit Of Detection* (LOD): the minimum analyte concentration that can be reliably detected;
- Dynamic Linearity Range: ability to follow linearly variations of analyte concentration in a certain concentration window.

In addition, SC-ISEs must satisfy several properties in order to be used in portable devices: they must provide reproducible and precise results, possibly with calibration-free measurements; they must be biocompatible and show high stability over time in order to ensure the possibility of monitoring the patient for several hours (and eventually even longer) without calibration. Potential drift is known to be one of the most critical issues in ion sensing. In this regard, it is crucial to plan several tests to control the sensor performance. The most important sensor parameters will be described in more detailed below.

2.5.1 Sensitivity

Before using a sensor, it is fundamental to calibrate it in order to characterize its analytical performance. A calibration procedure results in the establishment of a calibration curve, that shows the relationship between the sensor output and the analyte concentration. In order to calibrate a sensor, its response (e.g. the open circuit potential for ISEs) is recorded at increasing and known concentrations of target analyte. The sensitivity is then defined as the slope of the calibration plot [41].

As explained in Section 2.3, a linear relation is usually found when the OCP is plotted against the log of the ion activity, according to Nernst equation (Eq. 2.7). Thus, at room temperature ideal SC-ISEs show a Nernstian slope of 59.2 mV/decade in the case of monovalent ions and of 29.6 mV/decade in the case of divalent ions. However, in reality these slopes are not always

observed. In order to have an ideal behaviour, the membrane must be perfectly selective to the target ion. In addition, the RE potential must be independent of sample composition. This is roughly achieved in practice. Nernstian behaviour is attained only when the membrane-target ion binding is fully reversible. Furthermore, the membrane composition must not be influenced by this process in order to have an ideal response. For instance, this is not the case of AgCl-based membranes, where, very often, the surface is modified by other less soluble halides [35, 36, 43, 44].

2.5.2 Limit Of Detection (LOD)

The LOD is one of the most important parameters to characterize the sensor performance. In fact, it provides an indication of the smallest concentration of analyte that can be reliably measured. In general, in analytical chemistry the LOD is defined according to the *International Union of Pure and Applied Chemistry* (IUPAC) standard, as:

$$LOD = \frac{3 \times \sigma_b}{Sensitivity} \quad (2.8)$$

where σ_b is the standard deviation of the signal of the blank (that is a solution identical to the analyzed one, but without target analyte). The factor 3 maintains the required confidence level of 99%. In other words, the LOD is the concentration at which there is an increase of the signal with respect to the background level of the noise determined as three times the standard deviation of the blank measurement[61].

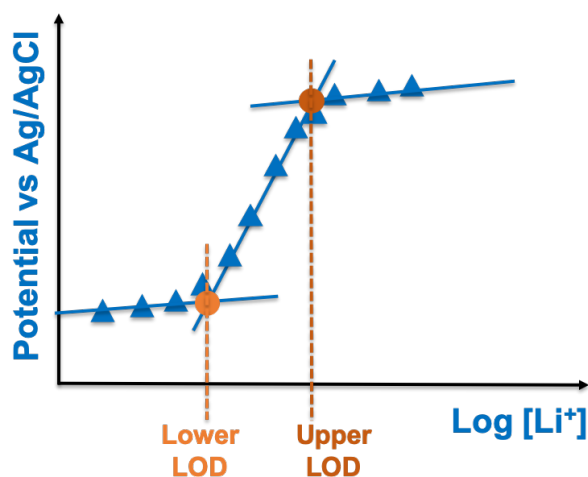


Figure 2.5 – Determination of upper and lower LOD according to IUPAC definition.

However, the standard IUPAC definition for potentiometric ISEs is different from the traditional one: the upper and lower LODs can be determined as the intercepts between different linear segments of the calibration curve, as shown in Figure 2.5. In fact, a deviation from the linear response is usually observed in ISEs at high and low activity concentrations. The

upper LOD is caused by loss of permselectivity (also called Donnan Exclusion), that is the permeability only to ions with the same charge sign of the measuring ion. In fact, the sensor shows Nernstian response only if no significant amount of counter ions (ions with opposite charge sign of the measuring ion) are coextracted together with primary ions from the sample into the membrane phase. In the opposite case, a reduction of the measured OCP with respect to the expected value is observed. On the other side, the lower detection limit can be explained considering interference effects or leaching out of target ions from the membrane. In addition, proper membrane conditioning is needed in order to make the membrane sensitive in a specific concentration range [41, 61].

It is important to notice that the unique definition of LOD in potentiometry is more restrictive than the classical one. In fact, for an ideal membrane, the LOD corresponds to the situation in which a well-defined part (50 % for ions of the same charge) of the interfering ions replaces the target ones in the organic phase. This will give a deviation of $17.8/z$ mV in the potential, where z is the ion charge number. On the contrary, the more common definition of LOD, that is three times the standard deviation of the noise, would result in a much lower value as the typical noise level in potentiometry is about 0.06-0.08 mV [41, 61].

2.5.3 Potential response and stability

A first relevant characterization step for SC-ISEs is the monitoring of the sensor potential stabilization time when it comes in contact with a solution for the first time. It is worth to notice that the selection of the electrically conductive substrate has an important effect [35, 62].

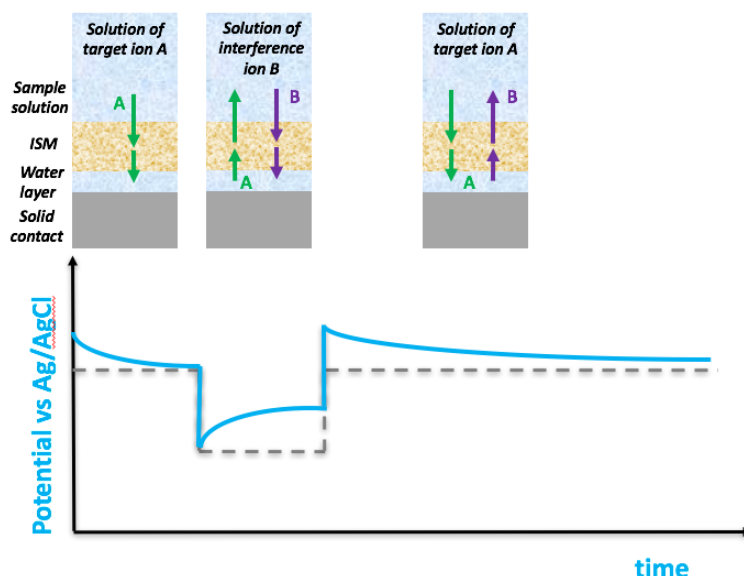


Figura 2.6 – Ion fluxes and typical potential profile during a water layer test for evaluating ISEs potential drift.

However, the most crucial and common issues of all-solid-state ISEs is potential drift over a long period of time, i.e. potential instability. This is typically due to the formation of a water layer at the ISM/SC interface. Its formation can be deduced from several effects: slow stabilization time, sensitivity of the sensor to osmolality variations, positive potential drift upon addition of interfering ions, negative drift upon their elimination. The most commonly used method for monitoring of drift effects due to formation of an aqueous layer is the so-called water layer test [41]. It consists in potential measurements during successive exposures of the sensor to concentrated solutions (e.g. 0.1M) of target and interfering ions for an extended period of time (several hours). Even small ionic fluxes during ion exchanges can lead to large changes of the very thin water layer at the ISE/SC interface, leading to positive and negative drifts during exposure to the interfering and target ion, respectively. The mechanism of fluxes and consequent potential variations is illustrated in Figure 2.6.

Potential stability can also be investigated by means of *Current Reversal Chronopotentiometry* (CRC). This method consists in the application of a direct current of a few nanoamperes, that is then reversed. The measured potential is characterized by a first jump followed by a slow drift. The potential drift $\frac{dE}{dt}$ can be computed from the slope of the curve [41, 47]. An example of this type of measurement is shown in Figure 2.7 for a Li^+ ISE based on two types of nanostructures, as compared with the one deposited on a bare electrode (the solid black curve in the graph).

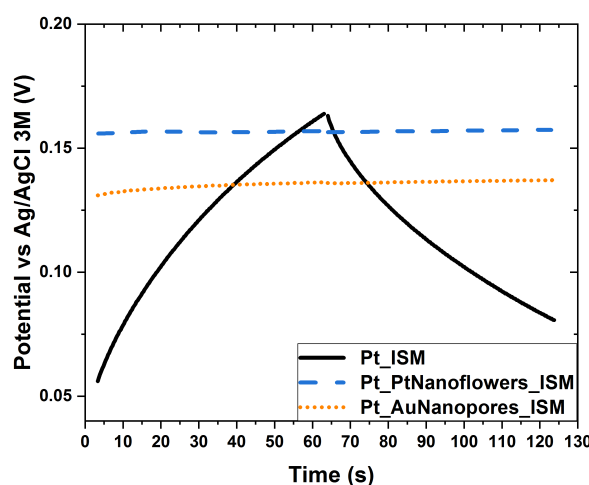


Figure 2.7 – CRC curves with and without nanostructured SCs. The behaviour of gold and platinum nanostructures are compared.

The capacitance of the electrode can be measured by using CRC as $C = \frac{i}{dE/dt}$, where i is the applied current and dE/dt the potential drift [35].

It is important to notice that the fabrication itself can give rise to water uptake, leading to the formation of a water film even before the contact with an aqueous solution. For instance, *Tetrahydrofuran* (THF) is known to be highly hygroscopic. Hence, if necessary,

freshly distilled THF and dry conditions can be used in order to minimize water uptake during fabrication [41, 42]. Drift can also be due to the small but non-zero currents required for the measurements. The assessment of the effect of current polarization is therefore important, especially on miniaturized electrodes (mm or sub-mm size) [35, 41]. Another possible source of potential drift is the degradation over time of membrane composition, related for instance to leaching out of ionophores or lipophilic salts. This effect can also be tracked by means of CRC [35, 41, 42].

2.5.4 Interference studies

One of the most crucial parameter of every sensor is its selectivity, i.e. the ability of a sensor to measure a concentration of a substance in presence of other interfering compounds. In fact, also in ISEs this is one of the most important characteristics as other ions of the same charge sign of the target one might be able to replace the target ions from the ISM. As explained in IUPAC reports [47], Nikolsky-Eisenman equation is used to express the measured potential under the presence of interfering ions:

$$E = E_0 + \frac{RT}{zF} \ln \left[a_A + \sum_B K_{A,B}^{pot} (a_B)^{\frac{z_A}{z_B}} \right] \quad (2.9)$$

where E_0 is a constant including the standard potential of the electrode, z_A and z_B are the valence number of the target and interfering ions respectively, a_A and a_B their activities, $K_{A,B}^{pot}$ the potentiometric selectivity coefficient of the target ion A against the interfering ion B. If $K_{A,B}^{pot} < 1$ the sensor is more selective towards the target ion. The smaller its values, the higher is the selectivity. On the contrary, if $K_{A,B}^{pot} > 1$, the sensor is more selective towards the interfering ions, but this case is rare.

It is important to notice that Equation 2.9 is valid under the following assumptions: 1) both ions show Nernstian response 2) $K_{A,B}^{pot}$ is constant 3) target and interfering ions have the same charge (when mono and divalent ions are present more complex equations must be used) [39, 47].

The selectivity coefficient in Equation 2.9 acts as a weighting factor for any ion activity. The calibration curves for membranes of different selectivity is given in Figure 2.8. It is evident that the higher the selectivity coefficient, the stronger the interference and, consequently, the smaller the LOD, while the sensitivity is not affected.

According to IUPAC recommendations three different methods are possible for the determination of the selectivity coefficients [63]:

- the Separate Solution Method (SSM) I uses two different solutions for the measurements. The first one contains only target ions A at activity a_A , the second one has only interfering

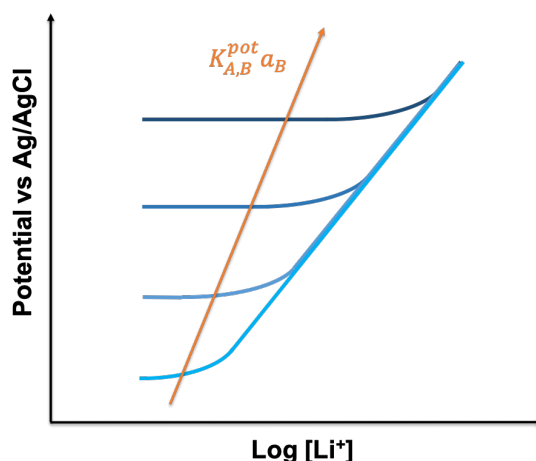


Figura 2.8 – Calibration curves of ISE with different selectivity coefficients. A smaller selectivity coefficient gives lower interference.

ions B at activity $a_B = a_A$. The selectivity coefficient is calculated as:

$$\log K_{A,B}^{pot} = \frac{(E_B - E_A)z_A F}{2.303RT} + \left(1 - \frac{z_A}{z_B} \log a_A\right) \quad (2.10)$$

It is worth to notice that with this method the slopes of both target and interfering ions must be Nernstian. Therefore, it is necessary to record the full calibration curve for each ion. The calculations of the selectivity coefficients will be done by using the potential values falling in the concentration window for which all ions of interests show Nernstian behaviour. While these might seem easy to do, in practice, if membrane selectivity is high, it can be difficult to achieve a Nernstian response for all interfering ions. If this happens, the incomplete ion-exchange at the sample/ISE interface will generate a bias and the experimentally determined selectivity coefficients may vary significantly. Several methods have been proposed to solve this issue. The simplest and most used one is based on membrane conditioning in a solution of the interfering ion, instead of the target one. This expedient will induce a complete ion-exchange at high concentrations, providing unbiased values of the selectivity coefficients.

- the Separate Solution Method (SSM) II is based on the independent determination of the calibration curves for ions A and B. The two activities that satisfy the condition $E_A = E_B$ are employed for the calculation of the selectivity coefficient according to equation 2.10.
- the Fixed Interference Method (FIM) uses solutions containing interfering ions at constant concentration and varying concentration of the target ions. The intersection of the extrapolated linear portions of the calibration curve plotted in semilogarithmic scale can be used to determine the activity of the target ion a_A . From its values, the selectivity

coefficient $K_{A,B}^{pot}$ can be computed according to the following equation:

$$K_{A,B}^{pot} = \frac{a_A}{(a_B)^{\frac{z_A}{z_B}}} \quad (2.11)$$

where z_A and z_B have the same sign.

The first and third methods are used in this work to compare the results as they are considered the most reliable ones. In fact, the SSM II, also called Matched Potential Method (MPM), has given, in some cases, negative potential changes. Therefore, the selectivity coefficients obtained with this method are meaningless [64, 65].

It is important to notice that the FIM can provide an indication of the minimum target ion concentration at which the interference effect is not relevant. Moreover, it has been shown in some papers [44, 63] that the measurements of some interfering ions in addition to target ion sensing can be used to remove interference errors.

2.6 State-of-the-art and challenges in solid-contact ISEs

Several all-solid-state ISEs have been developed in recent years to allow their integration into portable and wearable systems. However, some critical issues challenges still need to be addressed. The main limitations and current state-of-the-art of SC-ISEs technology is given below.

Frequent calibration is required in conventional ISEs, with consequent need of automation or qualified personnel. Because of their potential application as portable systems, high device-to-device reproducibility is needed for all-solid-state ISEs towards the development of calibration-free sensors. The calibration slope of these sensors is expected to be close to the theoretical value, hence reproducibility can be expressed in terms of its intercept, i.e. of the standard potential E_0 . A deviation of 0.7 mV can be considered acceptable for clinical laboratory. As discussed earlier, conductive polymers exhibit a wide redox potential window, with large values variability due to different factors. Therefore, it is extremely difficult to achieve very high E_0 reproducibility for this class of materials. In this regard, the choice of the electrically conductive substrate can be crucial to achieve good E_0 reproducibility and short equilibration time [10, 35].

As already discussed in the previous section, the most critical aspects of all-solid-state ISEs is probably potential stability. There are mainly two possible causes of potential drift: the formation of a water layer at the ISM/SC interface and the small but non-zero current required for OCP measurements. In the first case, the sensor is generally sensitive to osmolality variations, that is the concentration of all solutes in a given weight of water (expressed as milliosmoles of solute per kilogram of water). Membrane delamination can eventually occur during operation because of poor adhesion to the substrate.

2.6. State-of-the-art and challenges in solid-contact ISEs

A low LOD is another key element for efficient sensing. Conditioning of the membrane has been proved to be essential to achieve low LOD thanks to control of transmembrane ion fluxes [35, 42].

Recently, the importance of cytotoxicity assays during the development of sensors for on-body and in vivo ion sensing has also been highlighted. In fact, it is important to assess the toxicity of the ISM compounds to ensure their biocompatibility [66].

Different kinds of SCs have been investigated in literature to tackle these challenges, with particular attention to potential stability. Carbon nanotubes have been proposed as ion-to-electron transducers to increase contact capacitance in [55] and obtain efficient miniaturized systems. Systems using graphene [56, 57], reduced graphene oxide [67, 68] and fullerene [69] SC electrodes have also been realized. Gold nanoparticles [58, 70] and nanoporous films were used as SCs for K^+ ISEs. For a more detailed description of the state-of-the-art on current SC materials we refer the reader to section 3.1.

Many examples of portable SC ions-sensors for ions monitoring in several applications have already been reported in the last decade using these SC materials. We describe only a few of them here. A K^+ all-solid-state sensor for decentralized measurements was fabricated by screen printing of carbon nanotubes on a planar plastic substrate [71]. Quasi-Nernstian slope with a LOD of -6.5 was found, with good stability in the short term. The device was also tested in real samples for saliva and beverages monitoring. A K^+ sensor using platinum nanostructures as SC for monitoring of cell death has been reported [42].

In several works, paper was used as substrate to reduce costs. A simple route to fabricate disposable potentiometric ion sensors is shown in [4]: a conductive paper is produced by dipping conventional filter paper in a suspension of carbon nanotubes in a water-surfactant mixture; this acts both as conductor and ion-to-electron transducer (Fig. 2.9). The comparisons with the classical ISEs show good analytical performance towards K^+ , NH_4^+ and pH. A complete paper-based device for Cl^- and K^+ detection with integrated RE has been reported in [72]. The sensors have been tested both in aqueous and biological samples showing linear response and good reproducibility using a sample of only 20 μ l. A polymeric ISE device with a SC made of poly(3-octylthiophene) (POT), a lipophilic conductive polymer, was fabricated on

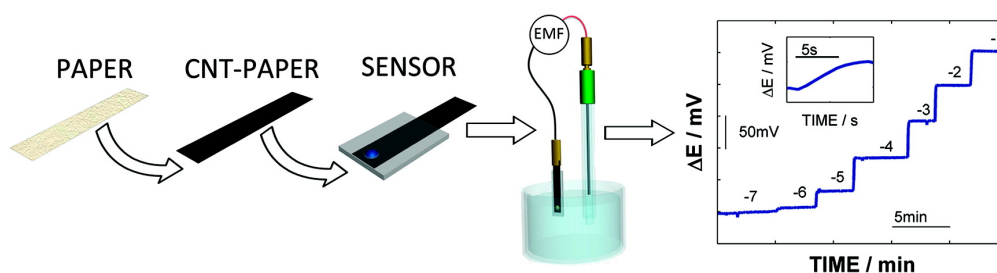


Figure 2.9 – Fabrication and testing of paper-based disposable ISEs. Reprinted with permission from [4]. Copyright (2012) American Chemical Society

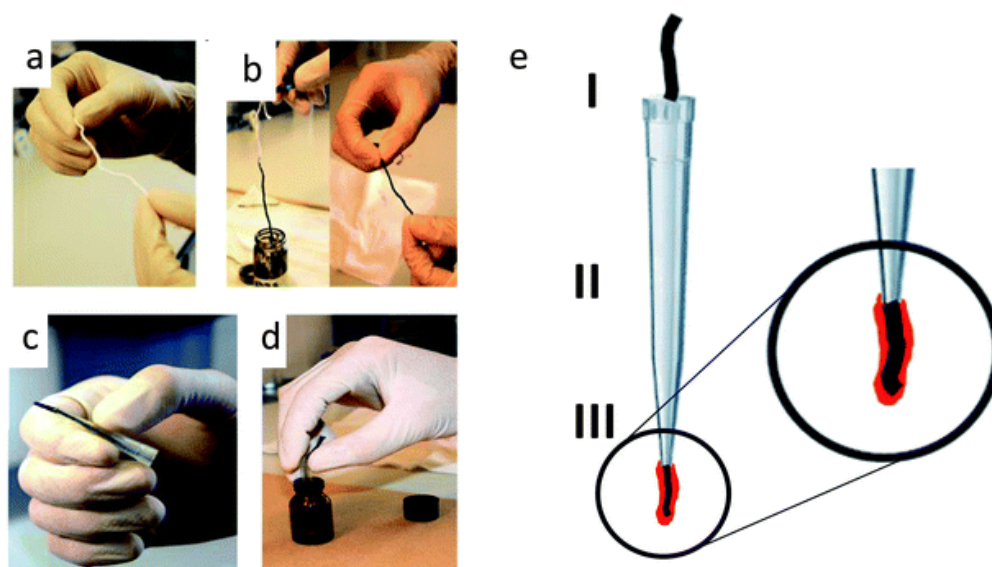


Figure 2.10 – Fabrication of the CNT–cotton sensing electrodes: (a) bare cotton yarn, (b) dyeing with CNT inks, (c) shielding with a pipette tip, and (d) dip coating into the membrane cocktail. (e) Schematic of the prototype electrode: (I) connection of the CNT yarn to a measuring device, (II) pipette tip (shield), and (III) membrane coated CNT yarn end. Reprinted with permission from [5].

a carbon nanotube conductive paper. This sensor was able to achieve LOD in the nanomolar range for K^+ , Cd^{2+} and Ag^+ [73].

Several examples of wearable patches for analysis of ions in sweat also exist. One of the first attempts was reported in 2000 by *Lynch et al.*. Iontophoresis stimulation was used to produce sweat. A peristaltic pump moves the sample to an array of SC-ISEs for the detection of K^+ , Na^+ and Cl^- . However, the great interest in all-solid-state ion sensors and in wearable devices has dramatically increased only in the last decade. The same group showed a primitive wearable belt for Na^+ detection in sweat [74]. Since then, many more sophisticated examples have been produced. Sodium, hydrogen and ammonia ISEs have been fabricated on textile substrates [5]. The procedure is based on a simple dyeing process of commercial cotton yarns using a carbon nanotube ink (Fig. 2.10).

ISEs have also been transferred directly to the skin through temporary tattoo to detect pH, ammonium and sodium [6, 7, 75]. The electrodes structures for H^+ and NH_4^+ sensing are given in 2.11a. The devices are resistant to mechanical deformations experienced by the human skin. They were tested on body with different setups with good analytical results.

Several sweat patches for chloride and sodium concentration using ISEs have also been reported [76, 77]. One of the most famous and interesting examples of wearable multi-sensing platforms was reported in *Nature* in 2016. Perspiration analysis has been performed using a fully integrated wearable headband which includes K^+ and Na^+ ISEs [8] (Figure 2.12a). The wireless system is tested for monitoring of human sweat during indoor and outdoor physical activity. Recently, an electrochemical autonomous sample extraction system has also been

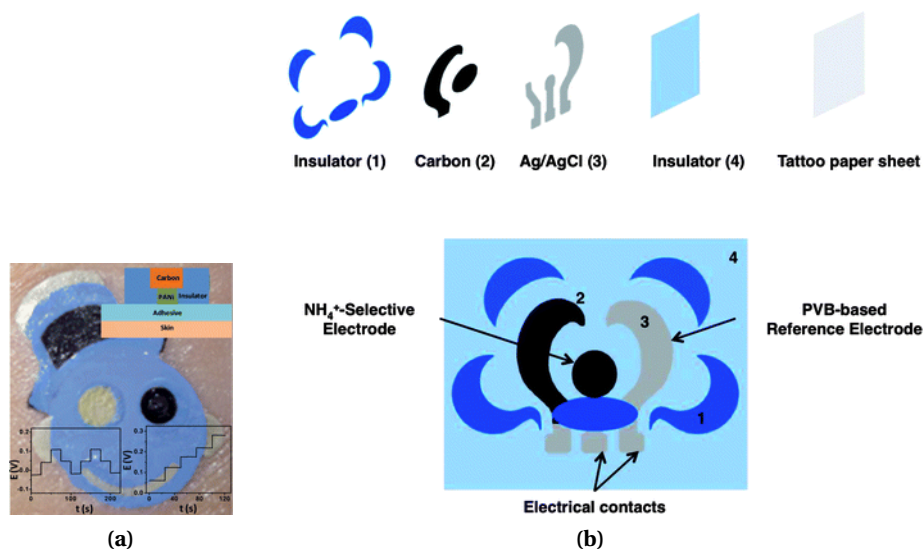


Figure 2.11 – a) Picture of the tattoo pH potentiometric sensor illustrating the two electrodes and the connection points for the voltmeter. Reprinted with permission from [6]. b) Scheme of the structure of a NH_4^+ sensing tattoo ISE. Reprinted with permission from [7].

implemented to induce sweat production with various secretion profiles [78].

Other examples include the wearable multi-sensing patch for continuous sweat monitoring of lactate, pH and Na^+ described in [30]. An interesting headband design was proposed by [9]: this is based on the use of a sweat collecting channel to ensure that enough sweat is wetting the electrodes (Figure 2.12b).

For more detailed reviews on recent advances in wearable chemical sensors we refer the readers to [27, 79]. Despite the huge efforts in recent years for the development of wearable potentiometric ion sensors to measure ions in sweat, no commercial examples exist on the market yet. However, some start-up companies with several patents [80, 81] are developing the technology to reach the commercial stage, like Eccrine systems, Incl [82] and Kenzen, Incl [83].

In conclusion, although major advances have been achieved in the last years, large room for improvements still exists to fabricate all-solid-state ISEs for portable and wearable devices [35]. This work addresses the realization of a general-purpose portable multi-electrode ion-sensing platform for different healthcare applications. This system will employ ISEs based on metallic nanostructured SCs in order to obtain improved potential stability and to avoid unwanted side reactions that are common when using conductive polymers. The same technology could also be applied in other fields of applications, like water monitoring in situations of aggressive pollution.

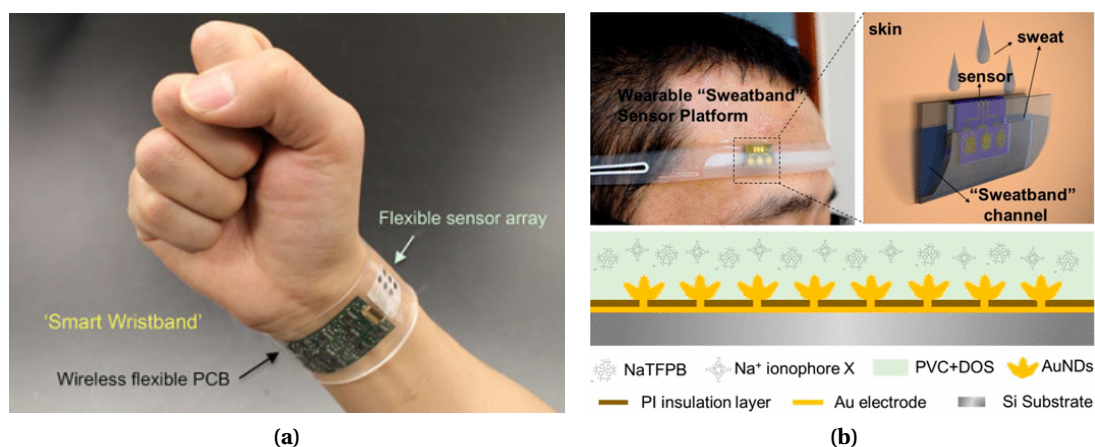


Figura 2.12 – a) Fully integrated wearable band for perspiration analysis. Reprinted with permission from [8]. b) Wearable sweatband based on gold nanodendrites for sodium sensing. Reprinted with permission from [9]. Copyright (2017) American Chemical Society

Noble metals nanostructured layers for improved ion-sensing

With the growing interests in smart systems and remote-monitoring devices in several fields, there has been in recent years an increasing effort to develop stable and efficient all-solid-state ISEs. Despite several solutions have been proposed, many challenges stills need to be overcome, like biocompatibility, potential stability, long-term storage and reproducibility.

In the previous chapter, we discuss briefly the current progress in SC-ISEs. In this chapter, we will continue the discussion on the state-of-the art on SC-ISEs with focus on the SC materials. Afterwards, we present the development of exceptionally stable all-solid state ISEs suitable for portable and wearable applications. The technology is based on a fast and highly reproducible potentiostatic deposition of noble metals. These materials offer improved sensing properties, high stability and biocompatibility. Different nanostructures, substrates and geometries have been considered in order to find the best solutions. Both gold and platinum nanomaterials have been investigated [10]. In addition, the response of SCs based on the combination of different nanostructured layers has also been studied [11]. Furthermore, an alternative synthesis method based on *Linear Sweep Voltammetry* (LSV) has been developed for the efficient deposition of these nanostructures on miniaturized electrodes [12].

3.1 State-of-the-art on SC materials

All solid-state ISEs have attracted special attention in recent years thanks to the unprecedented expansion of portable and wearable analytical devices for a variety of applications. The main challenge towards the development of a breakthrough technology is the stability of the potential response. For this reason, a variety of novel SC materials has been proposed. In particular, conductive polymers and high capacitance nanostructures seem to be the most promising solutions [43, 49, 84], as discussed in the previous chapter.

Nanostructured materials offer several advantages with respect to conductive polymers, including the possibility to achieve high conductivity, the absence of possible side-reactions

and the insensitivity to pH and light [9, 35]. They exploit the electrical double layer that is formed at the membrane/electrode interface for ion-to-electron transduction: the accumulation of ions on one side of the interface thanks to the role of the ISM attracts electrons or holes on the other side; this leads to the formation of an asymmetric capacitor. In these systems the interfacial potential is not related to redox reactions, as in the case of conductive polymers, or to ion partitioning, as in conventional ISEs, but to the amount of charge accumulated in the double layer. Thanks to their large surface area and their hydrophobic behaviour, nanostructured materials enable the achievement of good adhesion, avoiding the risk of water absorption. Moreover, they are typically characterized by high capacitance values. This property is crucial to reduce polarization effects due to the small but non-zero currents required for the measurement. For a more detailed description we refer the reader to [85]. Both carbon and noble metals nanostructures have been successfully investigated as SCs for ISEs: carbon nanotubes [55, 86–88], fullerene [69, 89], porous carbon [54, 90, 91], graphene [56, 57, 67, 68, 88], different polymer/carbon composites [92, 93], platinum nanoparticles supported on carbon black [59], platinum nanopetals [42], gold nanodendrites [9], gold nanoclusters [70], nanoporous gold films [60] and gold nanoparticles [26, 58]. An example of a SC-ISE based on MoO₂ microspheres has also been reported [94].

3.2 Experimental methods

This section provides a detailed description of the fabrication and characterization steps of the noble metal nanostructured SCs developed in this work.

3.2.1 Materials and micro-electrodes fabrication

Two types of substrates were investigated: commercial screen -printed electrodes and custom-made evaporated micro-electrodes.

Platinum and gold Screen Printed Electrodes (SPEs) with an active area of 12.56 mm² were purchased from Metrohm (Switzerland). All chemicals were purchased from Merck (Germany).

Gold micro-electrodes were used for the deposition of the platinum nanoflowers in section 3.5. The electrodes were fabricated in IMEC fabs. The gold electrodes were sputter deposited and patterned on a Si substrate, which was covered with a thermal SiO₂ layer. Subsequently, a Plasma-Enhanced Chemical Vapor Deposited (PECVD) SiO₂ passivation layer was deposited and patterned on the gold electrodes using contact lithography leaving only the bond-pads and electrode area for the platinum deposition open. Finally, the wafer was diced and a single die with the gold electrodes was mounted and wire-bonded to a printed circuit board (PCB) with connectors. All bond-pads, wire-bonds and connector pads were covered by epoxy (Epotek H70e-2) to shield them from the fluids during the platinum deposition and the final use of the electrodes. The electrodes have circular shape with a radius of 305 µm.

3.2.2 ISM fabrication

After the electrochemical cleaning of the electrodes [42], noble metals nanostructures were electrodeposited onto platinum and gold screen printed electrodes using an Autolab Potentiostat controlled by Nova Software (Metrohm, Switzerland). Gold and platinum nanostructures were deposited by applying a potential of -3 V in HAuCl_4 5 mM, NH_4Cl 1.25 M for 120 s and -1 V in 50 mM H_2SO_4 , 25 mM H_2PtCl_6 for 200 s, respectively, using a three-electrodes setup. A K0265 Ag/AgCl RE from Ametek (United States) was used for all depositions.

When using evaporated microelectrodes, platinum nanostructures were deposited by LSV in a 50 mM H_2SO_4 , 25 mM H_2PtCl_6 aqueous solution using an Autolab potentiostat with Nova software. A three-electrodes setup was employed with a Ag/AgCl double junction as RE. Two different potential ranges were used: between 0 and -0.6 V for the procedures LSV1, between 0 and -0.8 V for LSV2.

A volume of 10 μl of membrane cocktails consisting of 28.00 wt% Poly(vinyl chloride) high molecular weight, 1 wt% Li Ionophore VI (6,6-Dibenzyl-1,4,8-11-tetraoxacyclotetradecane), 0.7 wt% Potassium tetrakis(4-chlorophenyl)borate and 70.3 wt% 2-Nitrophenyl octyl ether for 100 mg of mixture dissolved in 1 mL of THF was drop-casted on SPEs. The membrane was kept at dark for 24 hours to allow solvent evaporation. Subsequently, the ISE was conditioned for 24 hours at 0.01 M LiCl, unless otherwise stated.

3.2.3 Morphological characterization

Scanning Electron Microscopy (SEM) was used for the morphological characterization of the electrodes. No sample pre-treatments were performed on the screen-printed electrodes. On the contrary, a thin iridium layer was deposited on the micro-electrodes by evaporation in order to reduce surface charging due to the glass cover. The SEM analysis was carried out at the Interdisciplinary Centre of Electronic Microscopy (CIME) of École Polytechnique Fédérale de Lausanne (EPFL) by using a Merlin or a Gemini 300 microscope from Zeiss (resolution up to 0.6 nm in STEM mode, probe current up to 300 nA, acceleration voltage 20 V to 30 kV) in SE mode. The accelerating voltage used for the SEM imaging is in the range 2-5 kV. The images of the nanostructured SCs were taken with an *In-Lens* detector at a Working Distance (WD) of 6 mm, while all others with an *HE-SE2* detector at a WD of 2.7 mm. The analysis of the different ISM thicknesses for different solution volumes was performed with a Xlf-30 scanning electron microscope at CIME (resolution up to 2 nm at 30 kV and 8 nm at 1 kV, acceleration voltage 1 kV to 30 kV) in SE mode. The electrodes have been broken to visualize their cross sections and to measure the average height of the deposited membrane, as in Figure 3.1b. An accelerating voltage of 2 kV and a WD of 9.4 mm were set for these measurements.

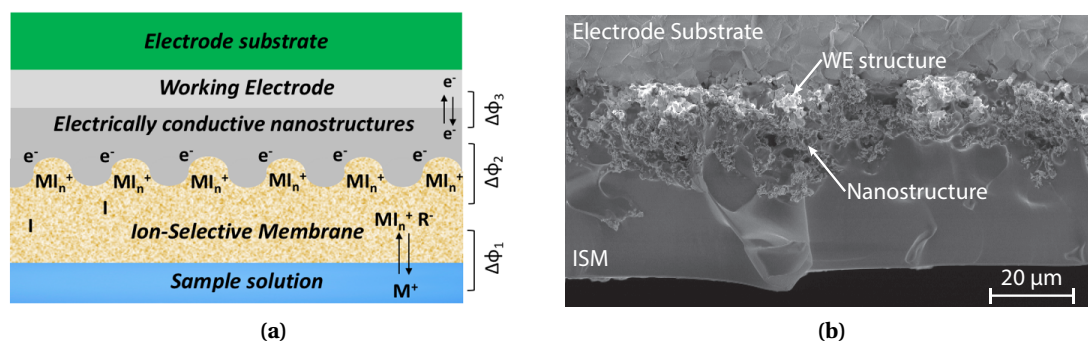


Figure 3.1 – a) Scheme of the fabricated nanostructures-based SC-ISEs. b) SEM cross-sectional view of a Li^+ ISE with platinum nanoflowers as SC. Reprinted with permission from [10].

3.2.4 Electrochemical measurements

All potentiometric and CRC measurements were performed in a two-electrodes cell setup by means of an Autolab potentiostat with Nova Software by Metrohm (Section 3.3 and 3.4) or an EMF6 Precision Electrode Interface by Lawson lab (Section 3.5). A Ag/AgCl double junction RE was used in all measurements with 3 M KCl as internal electrolyte and a 1 M lithium acetate salt bridge.

Cyclic voltammetric measurements were performed in a three-electrodes configuration using a K0265 Ag/AgCl RE from Ametek (United States). A 5 mM ferro/ferricyanide aqueous solution was employed.

3.3 Noble metal nanostructures for highly-stable solid-contact ISEs

In this section we propose a simple and reproducible fabrication method that can be applied to obtain high-quality and highly-stable all-solid-state ISEs for different applications. The sensors are based on the use of noble metal nanostructured SCs. These materials offer several advantages over carbon materials and conductive polymers, including fast and conformal one-step electrodeposition, high stability, non toxicity and increased surface area. SCs based on gold nanocorals are employed for the first time and compared to platinum nanoflowers to overcome the pervasive challenge of potential drift in current ISEs technology.

In all cases, a one-step electrodeposition procedure is used, allowing a much simpler and faster fabrication protocol with respect to the previously reported gold nanoporous SCs [60]. In addition, the effect of different substrates is deeply investigated. The various ISEs are characterized morphologically and electrochemically by SEM and CRC measurements. It is found that the use of nanostructured gold and platinum contacts gives an increase of the SC capacitance by one or two orders of magnitude, respectively, with respect to the flat metal, while the SC resistance is significantly reduced. The microfabricated sensors offer Nernstian behaviour with short response time (~ 15 s) and small potential drift during CRC

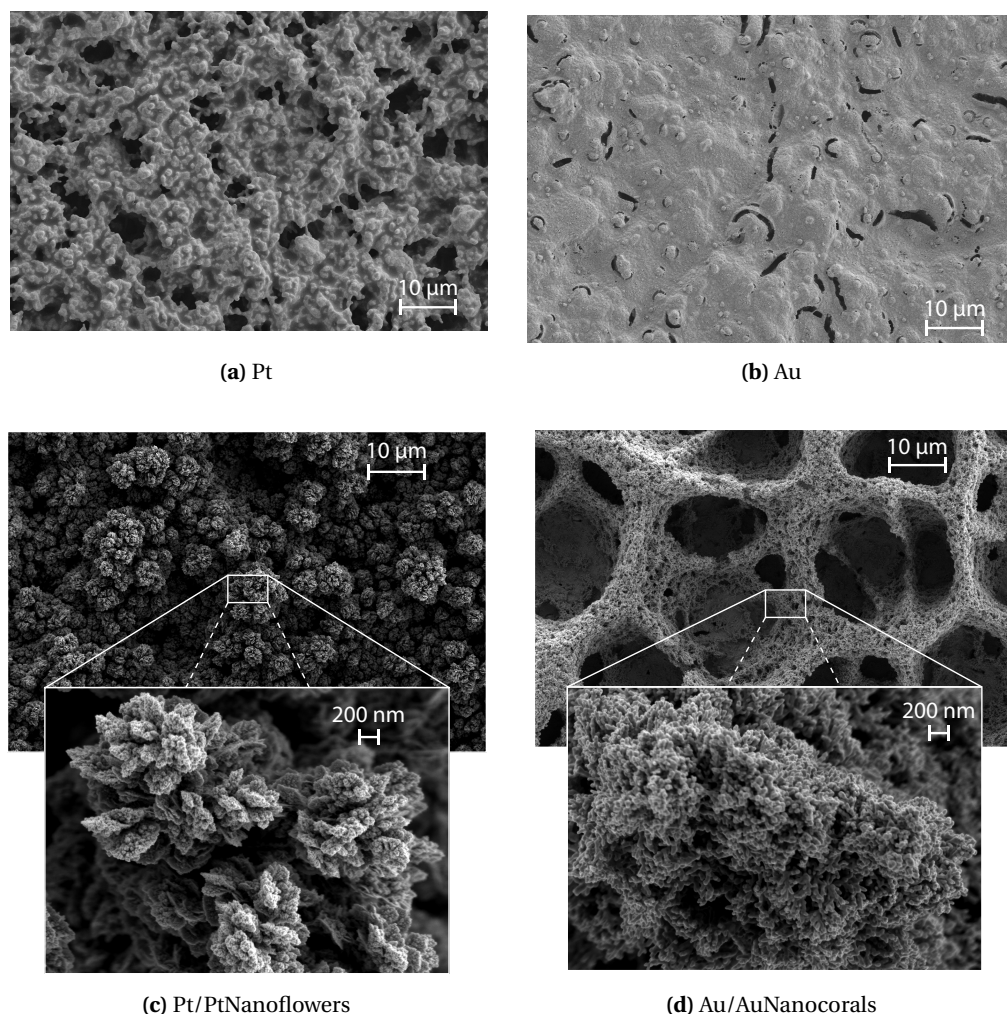


Figure 3.2 – SEM images of Pt/PtNanoflowers and Au/AuNanocorals SCs at different fabrication steps for: bare electrodes (a-b); electrodes after nanostructuring (c-d). Reprinted with permission from [10].

measurements ($\frac{dE}{dt} = 3 \times 10^{-5} \pm 2 \times 10^{-5}$ V/s). The exceptional stability of sensor response is also verified when no potential is applied. Low LOD and high selectivities are obtained, with values comparable to the ones reported for conventional ISEs. To our knowledge, we achieve the highest selectivities towards Ca^{2+} ever reported for SC-ISEs.

A scheme of the ISEs with noble metal nanostructured SCs that have been used in this work is given in Figure 3.1. Both gold and platinum nanostructured layers were developed previously to achieve sensitive detection of glucose [42, 95]. The platinum nanoflowers were also investigated to build a K^+ ISM on a platinum electrode microfabricated by standard lithographic methods and metal evaporation. In this work, for the first time, we use and compare these nanostructures to fabricate Li^+ ISM with improved sensing performance. We employ SPEs instead of the evaporated ones used in [42]. Both gold and platinum substrates are investigated as electrode materials.

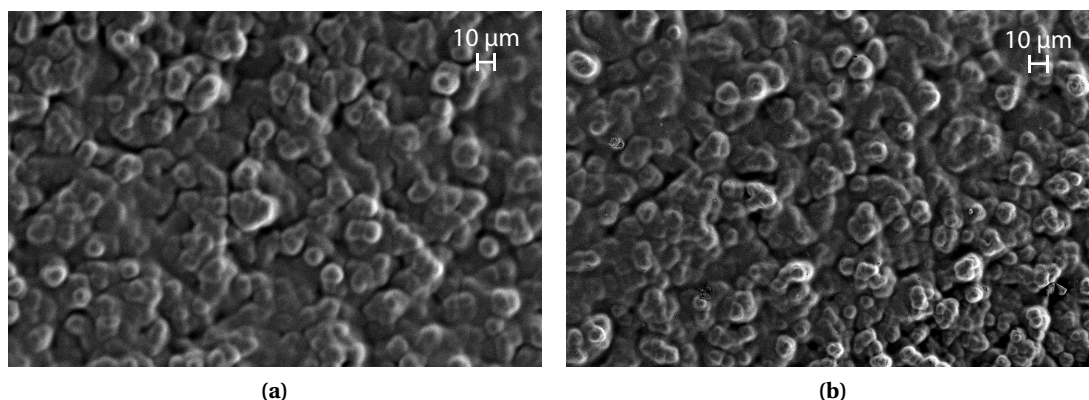


Figura 3.3 – SEM images of a Pt/PtNanoflowers/ISM before (a) and after (b) the electrochemical measurements. Reprinted with permission from [10].

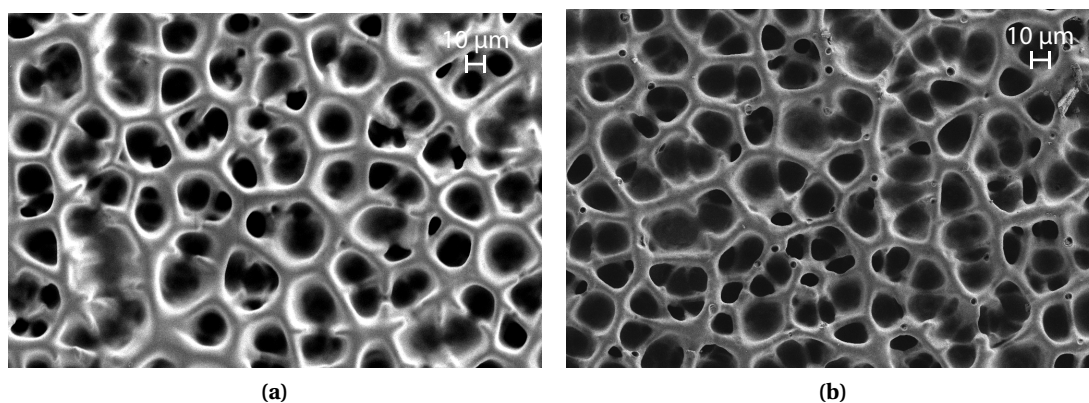


Figura 3.4 – SEM images of a Au/AuNanocorals/ISM before (a) and after (b) the electrochemical measurements. Reprinted with permission from [10].

3.3.1 Morphological characterization

SEM images were taken at different fabrication steps. In particular, the morphology of gold and platinum SPEs was investigated before and after the electrochemical nanostructuring of the substrate material. The bare platinum and gold SPEs are depicted in Figure 3.2a and 3.2b, respectively. SEM images of platinum nanoflowers deposited on a platinum SPE are reported in Figure 3.2c, while gold nanostructures on a gold SPE are reported in Figure 3.2b. It is evident that in all cases conformal and homogeneous depositions are obtained, despite the active area of the SPEs is larger than the microfabricated electrodes used in [42]. The platinum nanostructures form a highly branched fractal architecture. On the contrary, the electrochemically deposited gold is organized in pores with dimensions in the order of tens of micrometers. These are made of nanocoral-shaped features, as evident from the pictures at higher magnifications (zoom in Fig. 3.2c and 3.2d). In general, it is possible to conclude that the electrochemical deposition of platinum and gold nanostructures allows the shift from

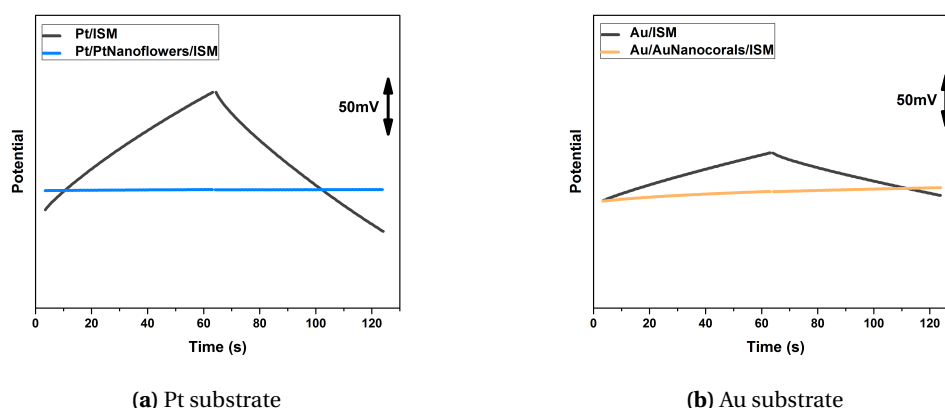


Figure 3.5 – CRC measurements of all-solid-state Li^+ ISEs on platinum (a) and gold (b) substrates showing the significant improvement in potential stability when nanostructured SCs are used. (± 5 nA for 60 s in 0.01 M LiCl solution) Reprinted with permission from [10].

micro- to nanoscale surface roughness, thus providing a significant increase in the surface area of the electrode.

Cross depositions of platinum nanoflowers on gold substrates and of gold nanocorals on platinum ones were also performed. No significant effect of substrate material on surface morphology was found, therefore we are not reporting the images here.

The pictures of the ISM membranes before and after the electrochemical measurements are reported in 3.3 and 3.4 on Pt/PtNanoflowers and Au/AuNanocorals SCs, respectively. No significant difference in topography was found after ISEs usage.

3.3.2 Characterization by current reversal chronopotentiometry and cyclic voltammetry

The electrochemical performance of Li^+ ISEs with and without nanostructured SCs on different substrates was compared by means of CRC measurements. This is a useful method to investigate potential stability. A direct current of a few nA is applied for certain time and then reversed, while measuring the sensor potential. The E-t curves show two main features: a jump when the change in current direction occurs and a slow potential drift at longer times [51].

The CRC measurements with and without nanostructured SCs on platinum and gold SPEs are given in Figure (3.5a) and (3.5b), respectively. It is evident that in both cases the presence of nanostructured SCs radically improves potential stability with respect to the ISM directly deposited on the platinum and gold SPEs. This phenomenon can be attributed to the different ion-to-electron transduction mechanism that is exploited by nanostructured materials [35]

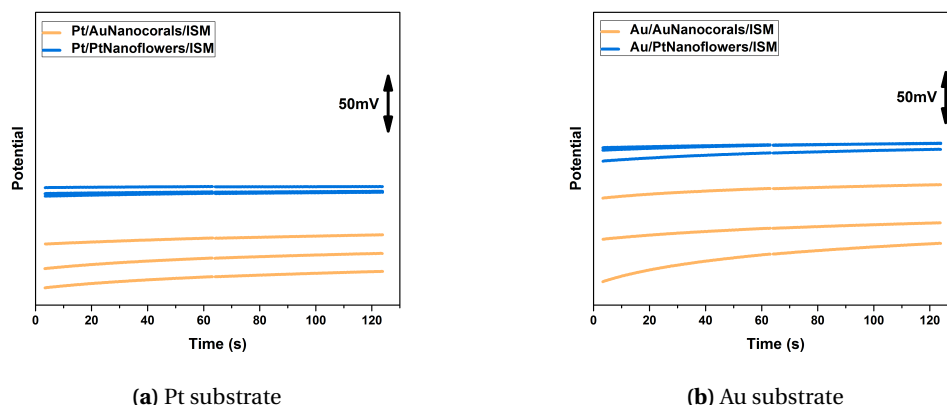


Figura 3.6 – CRC comparison of different stacks of nanostructured Li⁺ SC-ISEs. In particular, gold nanocorals and platinum nanoflowers were employed as SCs on both platinum (a) and gold (b) substrates. (± 5 nA for 60 s in 0.01 M LiCl solution) The three curves of the same colours correspond to three different samples of the same type. Reprinted with permission from [10].

(Fig. 3.1a): the ISM traps the target ions. Consequently, an accumulation of electrons is induced on the other side of the ISM and an asymmetric capacitor is formed. The interfacial potential is not related to redox reactions, as in the case of SCs based on conductive polymers, or to ion partitioning, as in conventional ISEs, but to the amount of charge accumulated in the double layer. Nanostructured-based SCs have typically high capacitance values. This property greatly reduces the risk of polarization effects due to the small but non-zero currents required for the measurement. In addition, improvement in membrane adhesion is in general achieved thanks to the large surface area. This property is important to minimize the risk of water absorption, that will cause high sensitivity to osmolality variations and structural damages of the membrane, eventually leading to the mechanical failure by delamination.

All four combinations of nanostructures-substrates were investigated and compared. The CRC responses of platinum and gold nanostructures are shown in Figure 3.6a for platinum substrates and in Figure 3.6b for gold electrodes. The curves of three different samples for each stack sequence are reported to compare reproducibility. It is possible to observe that platinum nanoflowers SCs seem to offer a slightly more stable response with respect to gold nanocorals. In addition, the response of different sensors with the same stack spans in a much narrower potential range for platinum nanoflowers than for gold nanocorals. This is observed on both gold and platinum substrates. This property is important towards the development of calibration-free sensors, that is still one of the major concerns in current SC-ISEs technology.

In order to obtain quantitative comparison among different samples to corroborate previous discussion, the resistance, potential drift and capacitance values of the different SC-ISEs were computed from the CRC results. Their values are reported in Table 3.1. Five samples for each stack sequence were considered. The total resistance of the electrode can be determined from the potential jump simply using Ohm's law ($V=RI$). From the table, it is possible to see

3.3. Noble metal nanostructures for highly-stable solid-contact ISEs

Tabella 3.1 – The total resistance, potential drift and capacitance values of the different fabricated Li⁺ ISEs have been computed from the CRC measurements. Five samples for each stack sequence were fabricated and tested. Reprinted with permission from [10].

	R [kΩ]	dE/dt [mV/s]	C [μF]
Pt/ISM	146±76	1.80±0.29	2.5±0.1
Pt/PtNanoflowers/ISM	28±4	0.03±0.02	195.3±96.8
Pt/AuNanocorals/ISM	41±19	0.12±0.06	50.5±24.0
Au/ISM	108±54	0.76±0.43	9.5±6.7
Au/PtNanoflowers/ISM	51±11	0.07±0.05	113.7±96.9
Au/AuNanocorals/ISM	30±21	0.21±0.14	29.4±13.7

that the use of noble metal nanostructures significantly decreases the contact resistance both on gold and platinum substrates, thus enhancing charge transfer at the SC interface. In particular, a reduction of one order of magnitude is obtained with nanostructured SC. Platinum nanoflowers give the largest improvement in SC conductivity. The lowest resistance value is achieved when Pt/PtNanoflowers SCs are used. As expected the bare gold electrodes have a lower contact resistance with respect to the platinum ones since this metal is characterized by higher electrical conductivity. The potential drift is defined by the slope of the curve [41, 47]. The use of gold and platinum nanostructured SCs provides a slope reduction of one and two orders of magnitudes, respectively, with respect to ISMs directly deposited on the SPEs. In particular, when using platinum substrates, the potential drift decreases from 1.80±0.29 mV/s without nanostructured SCs down to 0.12±0.06 mV/s with gold nanocorals and 0.03±0.02 mV/s with platinum nanoflowers. The capacitance values of the SC can be deducted according to the following equation: $C = \frac{i}{dE/dt}$, where i is the applied current [35], as described in Chapter 2. The highest SC capacitance is achieved by depositing platinum nanoflowers (195.3±96.8 μF) on platinum electrodes. Gold nanocorals have a capacitance in the range of several tens of μF, which is still one order of magnitude larger than the bare SPEs. This value is comparable or slightly higher with respect to the one reported for the electrodeposited nanoporous gold in [60]. However, the main advantage of our approach is the fast one-step electrodeposition procedure adopted for electrode nanostructuration.

The significant increase in electrode capacitance with nanostructured SCs was corroborated also by *Cyclic Voltammetry* (CV). The CV measurements were performed in an aqueous solution containing the ferro/ferricyanide redox couple. From Figure 3.7, it is possible to see that the use of nanostructured SCs greatly improves the capacitive current of the system. In particular the highest capacity is achieved with platinum nanoflowers SCs, as found in the CRC measurements. In addition, the better CRC performance achieved on platinum substrates was also confirmed, as evident from the larger integral area of the voltammograms with respect to ISM on gold substrates.

In conclusion, the CV measurements and the resistance and capacitance values calculated from CRC confirm the improved stability of the nanostructured SC produced in this work that was evident from a first qualitative analysis of CRC graphs in Figure 3.6. Platinum nanoflowers

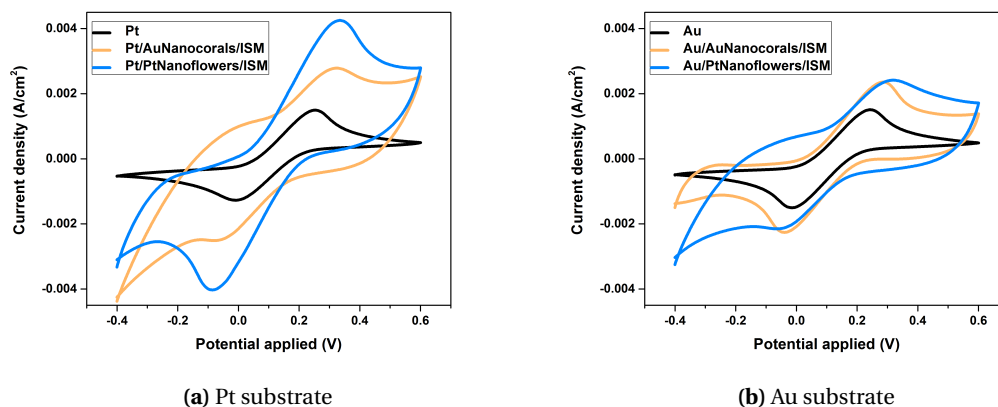


Figure 3.7 – Cyclic voltammograms in a 5 mM potassium ferro/ferricyanide solution of: a) Pt, Pt/PtNanoflowers and Pt/AuNanocorals SCs; b) Au, Au/PtNanoflowers and Au/AuNanocorals SCs. It is evident that electrode nanostructuring significantly increases the SC capacitance, as expected. (scan rate 100 mV/s) Reprinted with permission from [10].

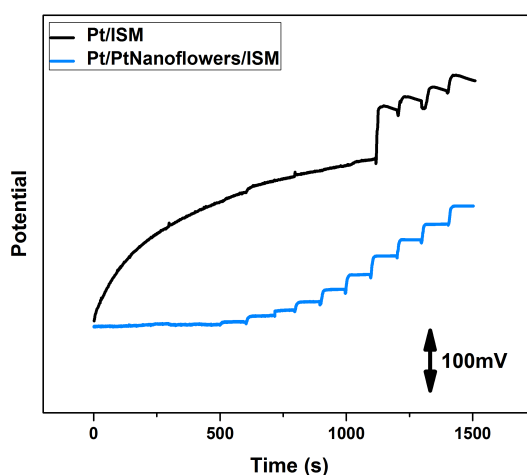


Figure 3.8 – Example of potentiometric time traces obtained during the calibration of Li^+ SC-ISEs with (blue curve) and without (black curve) nanostructured SC. The use of platinum nanoflowers provides a much more stable potential response. Reprinted with permission from [10].

seem to offer a slightly better performance than gold nanostructures in terms of potential stability and reproducibility, thus they will be the SC of choice in the following discussion, unless otherwise stated. By comparing the capacitance values of the different ISMs on the two substrates, it is also possible to state that in all cases platinum SPEs show a slightly higher capacitance with respect to the gold ones. Consequently, this substrate will be in general preferred in subsequent argumentation. The Pt/PtNanoflowers SC used in this work shows a much higher capacitance value with respect to the all-solid-state ISEs based on

other commonly used nanostructures, including carbon nanotubes [55], graphene [56, 57], reduced graphene oxides [68], graphene-polymer composites [92], fullerenes [89], but also of MoO₂ microspheres [94], platinum nanoparticles [59], gold nanodendrites [9] and nanoporous gold [60]. In addition its value is comparable to the capacitance of the SCs based on gold nanoclusters reported in [70]. Only [91] and [93] show higher capacitance values using porous carbon and carbon-black SCs, respectively.

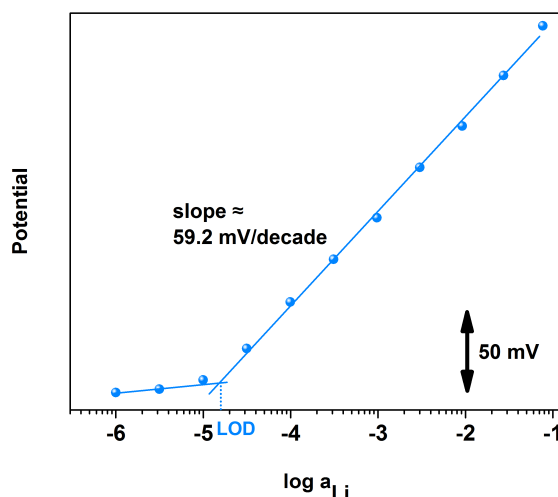


Figure 3.9 – Example of a typical calibration curve of Li⁺ ISEs with platinum nanoflowers as SCs. Reprinted with permission from [10].

Tabella 3.2 – Analytical parameters of Li⁺ SC-ISEs based on Pt/PtNanoflowers SCs. Reprinted with permission from [10].

	This work	Literature
Sensitivity [mV/decade]	58.7±0.8	59.8±1.4 [96]
LOD [M]	$(13 \pm 4) \times 10^{-6}$	5×10^{-6} [97]
Response time [s]	15-30	20 [97]
pH stability	from 4 to 12	from 4 to 12 [96]

3.3.3 Sensor calibration

The beneficial effect of electrode nanostructuring is also evident from the calibration time traces in Figure 3.8. Non-nanostructured electrodes (black and grey curves) show large potential instabilities and significant background signal. On the contrary, the ISE based on platinum nanoflowers offer a very smooth response (blue curve). Sharp steps are generated by successive increments in lithium concentration. In addition, a small increase in the background signal with time occurs in the presence of nanostructured SCs.

An example of a typical calibration curve computed from the potentiometric time trace is given in Figure 3.9 for an ISE with platinum nanoflowers as SC on a platinum SPE. A summary of all

sensor parameters are reported in Table 3.2. The sensor shows a near-Nernstian behaviour with a slope of 58.7 ± 0.8 mV/decade. It is important to notice that also the standard deviation is decreased by a factor of two with respect to the literature value, thus corroborating the good reproducibility of the system that was evident also from the CRC results. The LOD was computed according to IUPAC definition as the intersection of the linear portions of the curve [47]. Its value was found to be around 1.3×10^{-5} M. Although higher than in other papers [97], it is still satisfactory because well below the minimum effective concentration of the lithium drug (0.5 mM [98]). In addition, the response time of the sensor is always very short, as evident from the sharp steps in the calibration time trace of Figure 3.8.

The ISM thickness was varied by increasing the cocktail volume drop-casted on the electrode. As expected the increase in drop-casted solution leads to the formation of a thicker membrane until a maximum value is reached (Fig. 3.10). Above this saturation value the excess solution simply spreads around the electrode. The influence of ISM thickness on sensor performance was investigated. However, no significant effect of membrane thickness on Nernstian behaviour, LOD and selectivity was found. In general a solution volume of 10 μ L was drop-cast in this work, unless otherwise stated, in order to allow complete coverage of the electrode while limiting chemical consumption.

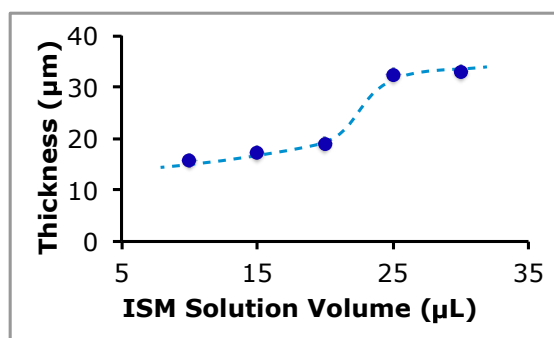


Figure 3.10 – ISM thickness as a function of the ISM cocktail volume drop-casted on the electrode. Reprinted with permission from [10].

3.3.4 Stability of potential response

The predictability of the sensor signal was investigated by comparing the potential developed by the system when exposed to a 0.01 M LiCl solution with the previously obtained calibration curve. The percentage difference between the potential value predicted from the calibration curve and the one measured in a constant concentration solution was found to be very small ($0.58 \pm 0.46\%$). A reversed sensor calibration was also performed in the range 10^{-5} M and 0.1 M (Fig. 3.11a). The curve corroborates previous results, proving the good stability and reversibility of the sensor response. In addition, potential drift over time was found to be very limited in the concentration range of interest, as evident from Figure 3.11b, that shows the trend of the potential value over time of two fabricated sensors when placed in a 1 mM LiCl solution for a long period of time.

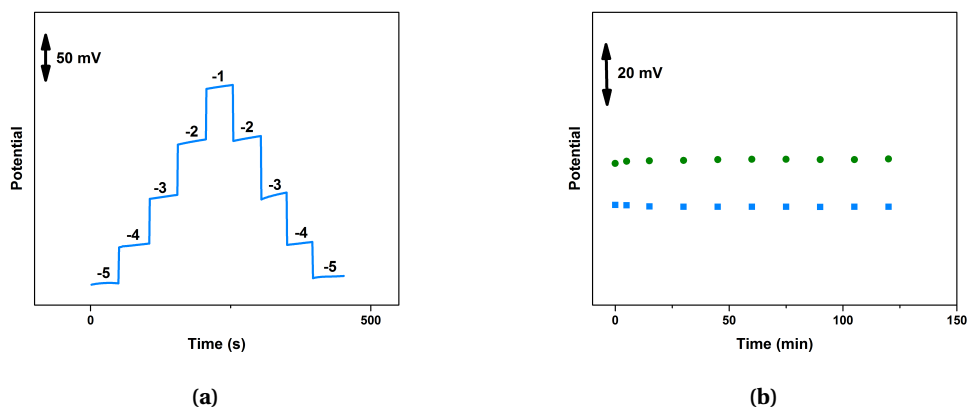


Figura 3.11 – a) Reversed calibration of Li^+ ISEs based on platinum nanostructured SCs between 10^{-5} M and 10^{-1} M (the logarithm of the concentration is reported above the corresponding potential step. b) Potential stability over time of two Li^+ ISEs based on platinum nanostructured SCs during immersion in a 3 mM LiCl solution. Reprinted with permission from [10].

3.3.5 Selectivity studies

The selectivity of the sensor was also investigated. Values comparable to the ones reported for conventional ISEs were always found. In addition, we achieve, to our knowledge, the highest selectivities towards Ca^{2+} ever reported for SC-ISEs. The results are reported in Section 4.1.3, in which different examples of applications of these nanostructured SC-ISEs in healthcare are reported and their performance is carefully evaluated.

3.4 Mixed gold and platinum nanostructured solid contacts

In the previous section we have shown simple and reproducible fabrication protocols for the deposition of gold and platinum nanostructures to obtain high-quality and highly stable SC-ISEs. In this paragraph, we propose for the first time the use of mixed gold and platinum nanostructured SCs to further improve the sensing performance. These devices show among the highest capacitance values reported in literature, while enabling a simple and fast (less than 6 minutes) deposition by electrochemical means. CV and CRC were employed to characterize the high performance and potential stability of these systems. The fabrication and calibration of Li^+ ISEs substantiate the possibility to use these novel SCs to build highly stable and accurate ion sensors.

3.4.1 Morphological characterization

SCs based on the deposition of platinum nanostructures on gold nanocorals and viceversa were fabricated and truly compared. Fig. 3.12 shows the SEM images of the two proposed

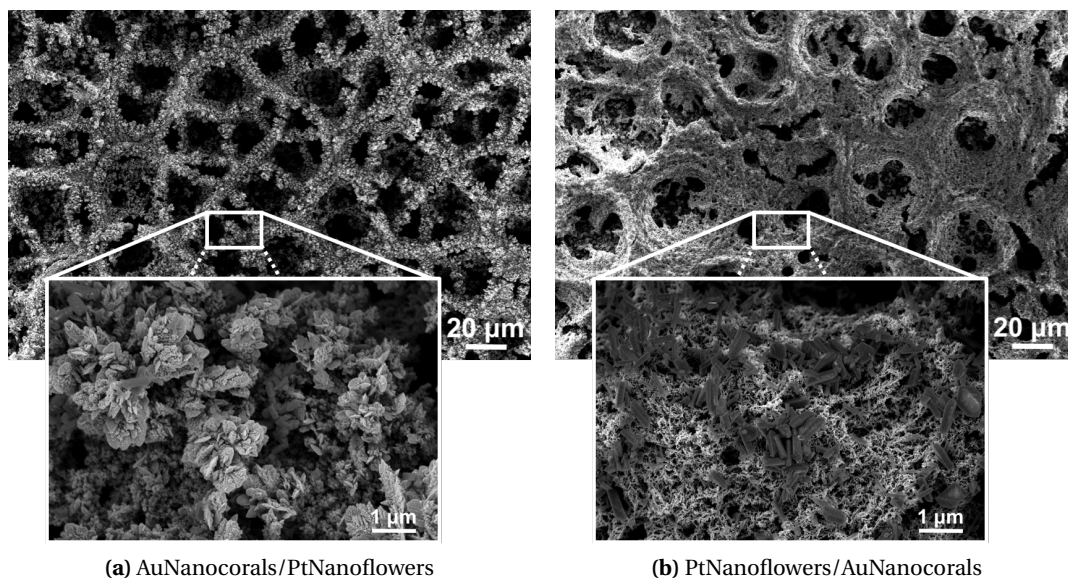


Figure 3.12 – SEM images of the proposed (a) AuNanocorals/PtNanoflowers and (b) PtNanoflowers/AuNanocorals SCs for portable and wearable ion-sensing applications. Reprinted with permission from [11]. ©[2018]IEEE

nanostructured SCs. As described in [95], the gold nanocorals organize in micropores (top part of Figure 3.12a). The successful deposition of platinum nanoflowers on top of the gold backbone is confirmed by the zoomed inset. From Fig. 3.12b, it is possible to observe that the deposition of gold nanostructures on platinum nanoflowers causes a small deformation of the gold micropores backbone. Despite these slight variations in morphology, the nanocorals-like features are maintained (zoomed inset in Fig. 3.12b).

3.4.2 Characterization by current reversal chronopotentiometry and cyclic voltammetry

The electrochemical behaviour of these two types of nanostructured SCs is investigated by means of CV and CRC measurements. Figure 3.13 shows the CVs of the two combinations of gold and platinum nanostructures proposed in this work (i.e. AuNanocorals/PtNanoflowers and PtNanoflowers/AuNanocorals SCs) in comparison with the ones of each single nanostructure and with the bare electrode. All curves were obtained in an aqueous solution containing ferro/ferricyanide as redox couple using platinum SPEs as substrates. In general, high capacitance values enable the achievement of more stable potential responses since the risk of polarization effects by small non-zero currents is greatly reduced. It is evident from the area under the curves that the use of mixed noble metal nanostructures significantly improves the SC capacitance with the respect to the single materials. In particular, the AuNanocorals/PtNanoflowers SC (pink curve) gives the highest capacitance value.

CRC was used to corroborate the CV results (Fig. 3.14). The measurements were performed

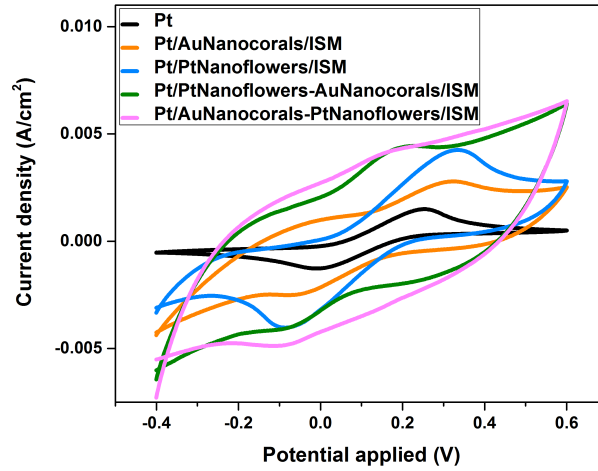


Figure 3.13 – CV measurements of the proposed AuNanocorals/PtNanoflowers (pink curve) and PtNanoflowers/AuNanocorals (green) SCs in comparison with the flat platinum electrode (black) and the previously developed AuNanocorals (orange) and PtNanoflowers (blue) SCs. All voltammograms were obtained in a 5 mM potassium ferro/ferricyanide solution at a scan rate of 100 mV/s. Reprinted with permission from [11]. ©[2018]IEEE

using a Li^+ ISM. The significant reduction in potential drift when nanostructured SCs are employed is clear. In order to obtain quantitative comparisons, the capacitance values of the different SCs were calculated from the CRC curves as $C = \frac{i}{dE/dt}$, where i is the applied current, as described in 3.3.2. As expected from the cyclic voltammograms, the highest capacitance, that is $288 \pm 39 \mu\text{F}$, is attained by the AuNanocorals/PtNanoflowers SC, followed by the PtNanoflowers/AuNanocorals stack with a value of $231 \pm 34 \mu\text{F}$. In both cases, the values are well above the ones reported in [10] for the single platinum nanoflowers ($195 \mu\text{F}$) or gold nanocorals ($51 \mu\text{F}$). In addition, these SCs offer a much higher capacitance than most of other nanostructured materials commonly used as SCs, including graphene [56, 57], graphene-polymer composites [92], reduced graphene oxides [68], carbon nanotubes [55], fullerenes [89], platinum nanoparticles [59], MoO_2 microspheres [94], gold nanodendrites [9] and nanoporous gold [60]. In addition their capacitance is larger or similar to the one of gold nanoclusters proposed in [70]. Only porous carbon [91] and carbon-black SCs [93] offer higher values, but a much more complicated protocol is required for their fabrication.

3.4.3 Sensor calibration

An example of a Li^+ calibration curve is given in Figure 3.15 for a AuNanocorals/PtNanoflowers SC. From the inset in Figure 3.15, it is possible to see that smooth calibration time traces and sharp steps are achieved, as expected from the high capacitance of these materials. The sensor response time is always very low, around 15-20 s. Quasi-Nernstian behaviour is always achieved in the linear range between 1.3×10^{-5} and 10^{-1} M. In conclusion, the use of

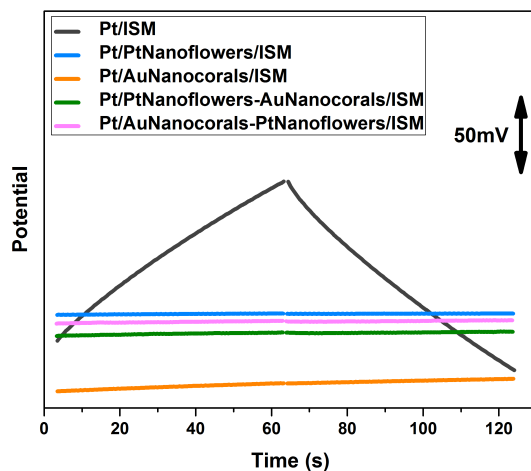


Figura 3.14 – CRC measurements of the proposed AuNanocorals/PtNanoflowers (pink curve) and PtNanoflowers/AuNanocorals (green) SCs in comparison with the flat platinum electrode (black) and the previously developed AuNanocorals (orange) and PtNanoflowers (blue) SCs. All curves were obtained with a Li^+ ISM in a 0.01 M LiCl solution applying a current of ± 5 nA for 60 s. Reprinted with permission from [11]. ©[2018]IEEE

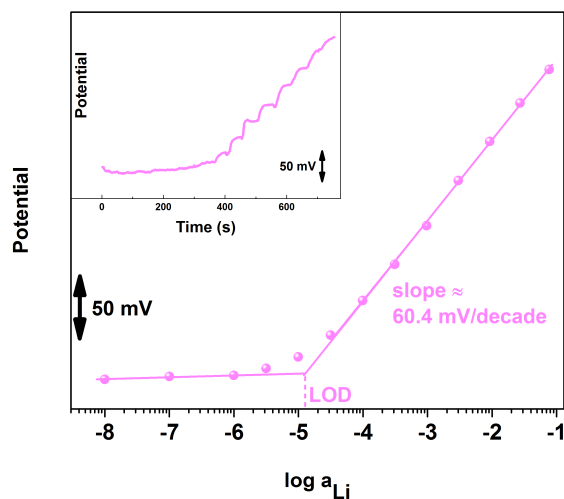


Figura 3.15 – Example of Li^+ calibration curve obtained with a Li^+ ISE based on a AuNanocorals/PtNanoflowers SC. The small inset shows the corresponding time trace. Reprinted with permission from [11]. ©[2018]IEEE

combined mixed noble metals nanostructures offers a simple and fast method to produce high capacitance and high performing ISEs for portable and wearable applications.

3.5 Fast electrodeposition procedures of platinum nanostructures on miniaturized electrodes

In recent years the great expansion of *Point-Of-Care* (POC) and wearable systems and the attempt to perform measurements in tiny spaces have also risen the need of increasing sensors miniaturization. In the previous paragraphs, fast constant potential electrodeposition techniques have been proven to be an efficient way to obtain conformal platinum and gold nanostructured layers on macro-electrodes. However, this technique is not effective on micro-electrodes. In this section, we investigate an alternative one-step deposition technique of platinum nanoflowers on micro-electrodes by LSV.

The effective deposition of platinum nanoflowers with similar properties to the ones deposited on macro-electrodes is confirmed by morphological analysis and by the similar roughness factor (~ 200) and capacitance ($\sim 18 \mu\text{F}/\text{mm}^2$). The electrochemical behaviour of the nanostructured layer is then tested in a SC Li^+ -selective micro-electrode and compared to the case of macro-electrodes. The sensor offers Nernstian calibration with same response time (~ 15 s) and a one-order of magnitude smaller LOD (2.6×10^{-6}) with respect to the macro-ISEs. Finally, sensor reversibility and stability in both wet and dry conditions is proven.

3.5.1 Morphological characterization

Two different LSV procedures have been investigated in this work to achieve a fast electrodeposition procedure of platinum nanostructures on miniaturized evaporated electrodes. In particular, two potential windows have been used: between 0 and -0.6 V for the procedure LSV1, between 0 and -0.8 V for LSV2. In addition, we have tested the difference in morphology when two subsequent identical deposition methods are applied on the same electrode. The SEM images of all resulting electrodes are shown in Figure 3.16. It is possible to notice that in the case of LSV1 a smaller quantity of platinum is deposited with respect to the others (Fig. 3.16a). In fact, as a lower amount of material is transferred on the substrate, the architecture of platinum nanostructures appear to be simpler and less developed, although the nanofeatures are already present. As the potential window is extended (3.16c) or a double deposition is performed (Fig. 3.16b) or both (Fig. 3.16d), a higher amount of platinum is deposited on the electrode and more complex nanoflower-shaped structures are formed. No big variations in morphology are evident among the three nanostructures. These results were confirmed by comparing the roughness factors of the different platinum architectures, obtained as the ratio between the electrochemical active area (calculated as described in [42]) and the geometrical area of the electrodes. A part from LSV1 which shows a roughness factor of about 102.9 ± 1.7 , all other nanostructures obtained by LSV attain very similar values (198.4 ± 0.3 for LSV1x2, 205.9 ± 0.1 for LSV2, 208.4 ± 1.5 for LSV2x2) to the one obtained on macro-electrodes by constant potential electrodeposition (201.8 ± 0.7). Thus, we can conclude that, despite the slight differences in morphology, the surface area of the different nanostructured layers are comparable. Consequently, only the faster single-step deposition methods will be further

used for the electrochemical characterization of the SC electrodes since the more complex ones do not offer enough advantages.

The following reactions can be involved in the platinum layer formation:

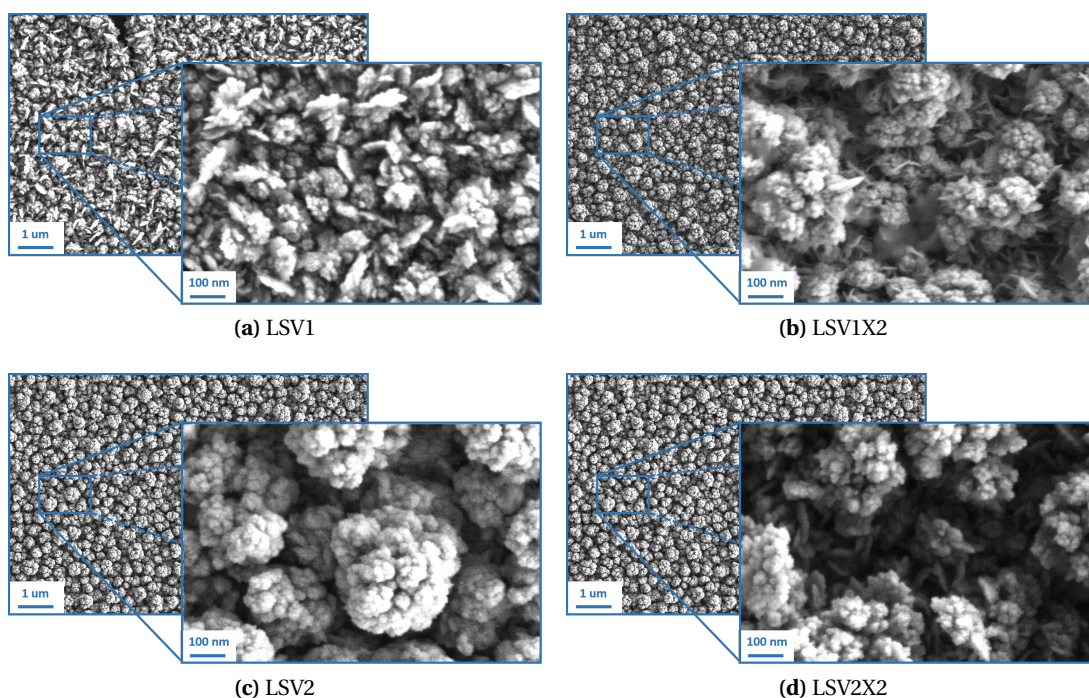
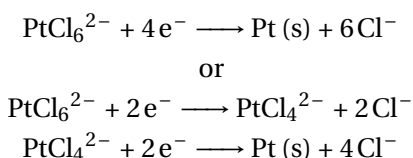


Figure 3.16 – SEM images of platinum nanostructures deposited by LSV with different voltage ranges: between 0 and -0.6 V for the procedures called LSV1 (a), between 0 and -0.8 V for LSV2 (c). The comparisons with the structures obtained with 2 subsequent depositions is given in (b) and (d). Reprinted with permission from [12].

3.5.2 Current reversal chronopotentiometry and solid-contact capacitance

The electrochemical behaviour of the platinum nanostructures fabricated on micro-electrodes were tested in a Li^+ ISEs. The schematic illustration of the device fabrication and working mechanism is given in Figure 3.17.

The obtained curves are reported in Figure 3.18 in comparison with the electrodes without nanostructured SC. It is possible to see that the potential drift is significantly lowered when the surface area of the electrode is increased. This is a consequence of the different ion-to-electron transduction mechanism exploited by nanostructured materials and of their hydrophobic

3.5. Fast electrodeposition procedures of platinum nanostructures on miniaturized electrodes

behaviour, which reduces the risk of water layer formation [35].

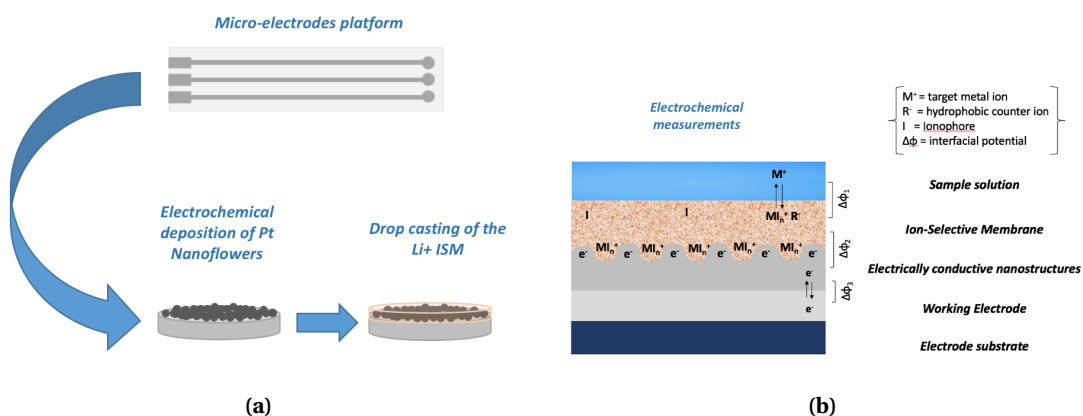


Figure 3.17 – (a) A schematic illustration of the fabrication of the Li^+ ISEs based on the one-step electrodeposition of platinum nanostructures on custom-made evaporated gold micro-electrodes. Their structure and working principle during electrochemical measurements is highlighted in (b). Reprinted with permission from [12].

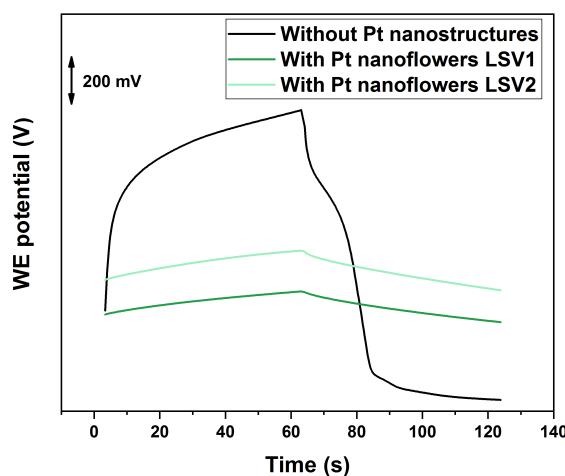


Figure 3.18 – CRC measurements of the different fabricated Li^+ ISEs on micro-electrodes without platinum nanostructures and with platinum nanoflowers deposited by LSV1 and LSV2. Reprinted with permission from [12].

The SCs capacitance of the different electrodes can be calculated using to the following equation: $C = \frac{i}{dE/dt}$, as described in the previous sections. The obtained values are reported in Table 3.3.

If we normalize the calculated capacitance by the area of the electrode, it is possible to notice that the obtained values are very close to the ones reported in [10] for similar structures

Tabella 3.3 – Potential drift and capacitance values obtained from the CRC measurements of the different fabricated Li^+ ISEs on micro-electrodes in comparison with the literature values on macro-electrodes. Reprinted with permission from [12].

	dE/dt [mV/s]	C [μF]	normalized C [$\mu\text{F}/\text{mm}^2$]
Without Pt Nanostructures (micro-electrodes)	1.02 ± 0.22	0.57 ± 0.17	4.35 ± 1.29
LSV1 (micro-electrodes)	0.23 ± 0.08	2.55 ± 0.41	19.39 ± 1.29
LSV2 (micro-electrodes)	0.18 ± 0.01	2.39 ± 0.19	18.15 ± 3.09
Literature (macro-electrodes)[10]	-	-	15.55 ± 7.71

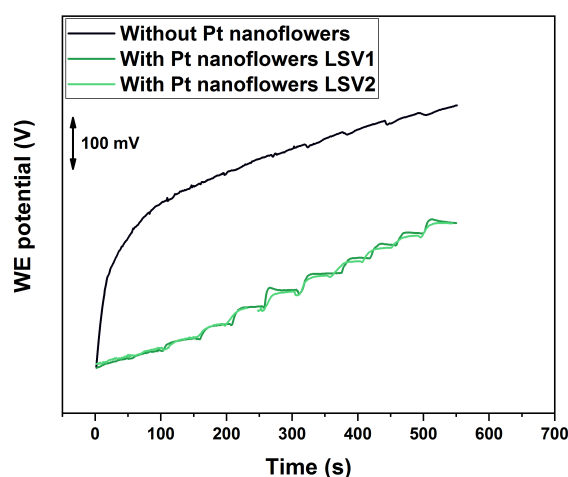


Figura 3.19 – Calibration time traces of lithium-ISE fabricated on different SCs.

deposited on macro-electrodes. This results confirms that the LSV procedure proposed in this work allows the formation of platinum nanostructures on micro-electrodes, with comparable results to the ones obtained on macro-electrodes by constant potential deposition. So, we can conclude that although LSV1 and LSV2 have some differences in morphology, as shown in Figure 3.16, the SC capacitance (which defines the stability of the electrode) is very similar. This is the most crucial property in ion-sensing as potential drift is the main issue related to the use of ISEs, especially on miniaturized electrodes.

3.5.3 Calibration of the lithium ion-selective electrodes

Lithium-ISEs were fabricated on the different SCs and calibrated between 10^{-7} M and 0.1 M by subsequent additions of LiCl. The resulted time traces are reported in Figure 3.19. It is evident that the presence of platinum nanostructures significantly improves the sensor

3.5. Fast electrodeposition procedures of platinum nanostructures on miniaturized electrodes

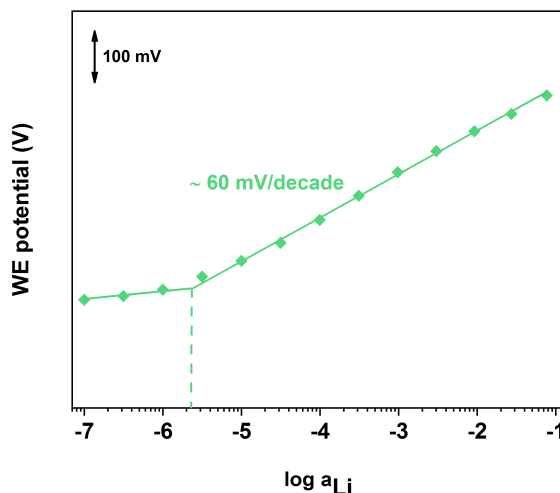


Figura 3.20 – Calibration curve of lithium SC-ISE with platinum nanostructures deposited by LSV2. Reprinted with permission from [12].

Tabella 3.4 – Sensor parameters obtained from the calibration curves of the different fabricated Li^+ ISEs on micro-electrodes in comparison with the literature values on macro-electrodes. Reprinted with permission from [12].

	Sensitivity [mV/decade]	LOD	Response time [s]
LSV1 (micro-electrodes)	61.7 ± 3.7	$(4.4 \times 10^{-6}) \pm 3.9 \times 10^{-6}$	15-30
LSV2 (micro-electrodes)	59.0 ± 1.0	$(2.6 \times 10^{-6}) \pm 0.5 \times 10^{-6}$	15-30
Literature (macro-electrodes)[10]	58.7 ± 0.8	$(13.0 \times 10^{-6}) \pm 4.0 \times 10^{-6}$	15-30

response. ISE without nanostructured SCs show enormous potential drift. As a consequence, the calibration steps are almost invisible. On the contrary, the curves obtained with platinum nanostructured-SCs (green lines) have clear and smooth features upon lithium addition.

From the potentiometric time traces given in Figure 3.19 it is possible to calibrate the sensors. An example is given in Figure 3.20 for the SC with platinum nanostructures deposited by LSV2. The sensor parameters obtained for all different micro-electrodes is given in Table 3.4 in comparison with the values reported in literature for macro-electrodes. From these results it is possible to conclude that all sensors offer Nernstian behaviour and short response time. In addition, the miniaturization of the electrodes reduces the LOD by half a order of magnitude with respect to the macro-electrodes in the case of LSV1 deposition. In the case of LSV2 deposition, the improvement in the LOD is even higher (one order of magnitude), while the standard deviation is significantly reduced (almost a half-order of magnitude). This can be explained by considering the higher surface area of these nanostructures, as discussed previously.

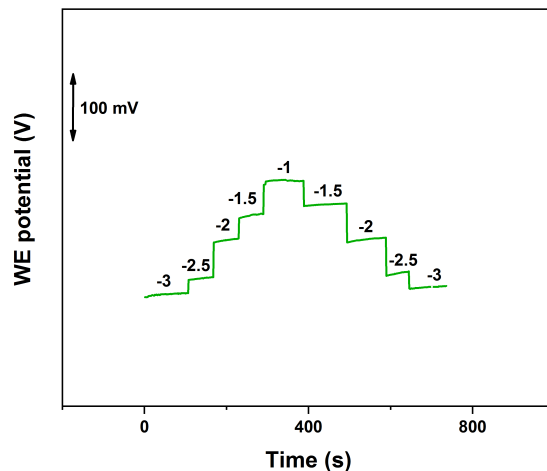


Figura 3.21 – Reversed calibration between 10^{-3} and 10^{-1} M of for a Li^+ SC-ISE on micro-electrodes. Platinum nanoflowers were deposited by LSV2. Reprinted with permission from [12].

3.5.4 Reversibility and lifetime studies

Sensors reversibility was proved by performing a forward and backward calibration between 10^{-3} and 10^{-1} M, which is the range of interest in clinical applications. A typical response for a SC-ISE obtained by LSV2 deposition of platinum nanostructures is given in Figure 3.21. It is evident that the device offers a stable and reversible response in the detection range.

Another important parameter in ion-sensing is the lifetime of the electrodes. In particular, it has been found in many articles [35, 41, 99, 100] that the sensor performance significantly lowers when the sensor is kept in solution for a long period of time. Figure 3.22 shows the comparison among calibration traces obtained from the freshly prepared sample and the ones after 40 days of storage in dry or in wet conditions. It is possible to notice that the sensor response remains almost the same, with smooth and sharp steps and Nernstian response in all cases (Table 3.5). Also after 40 days of storage in solution, the sensor slopes and LOD decrease by less than 5 %. This property is crucial in on-line applications where continuous exposure to wet conditions is needed.

Tabella 3.5 – Sensor parameters obtained from the calibration traces in Figure 3.22 for the freshly prepared Li^+ SC-ISE and the ones after 40 days of storage in dry and then in wet conditions. Reprinted with permission from [12].

	sensitivity [mV/decade]	LOD	response time [s]
As prepared	59.1	2.7×10^{-6}	~15 s
After 40 days in dry	59.0	2.7×10^{-6}	15-20
After 40 days in wet	56.5	2.8×10^{-6}	15-40

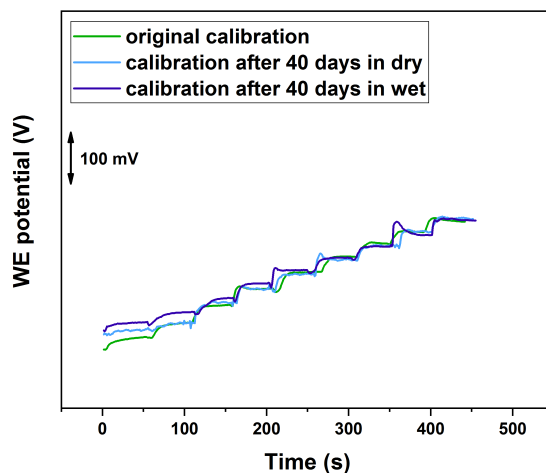


Figure 3.22 – Calibration traces obtained from the freshly prepared Li^+ SC-ISE (green) and the ones after 40 days of storage in dry (light blue) and then in wet (dark blue) conditions. Platinum nanoflowers were deposited by LSV2. Reprinted with permission from [12].

3.6 Summary

In Section 3.3, we have presented the development of all-solid-state Li^+ ISEs exploiting noble metals nanostructures as ion-to-electron transducers. In particular, gold nanocorals deposited in a fast and conformal one-step electrochemical deposition process are used for the first time as SCs and compared with similarly obtained platinum nanoflowers. Conformal deposition and improved surface area were demonstrated by means of SEM. The nanostructures performance on different substrate electrode materials and the influence of the conditioning procedures were deeply investigated. Electrochemical measurements proved the reduced charge transfer resistance, large capacitance, exceptional potential stability and excellent analytical performance of the sensors. All selectivity values are found to be very close to the ones reported for conventional ISEs. In addition, the highest selectivity towards Ca^{2+} ever obtained for Li^+ SC-ISEs is achieved.

In the following section we combine the gold and platinum nanostructures described in Section 3.3 to fabricate mixed gold and platinum SCs. With their large double layer capacitance, high surface area and great hydrophobicity, these SCs enable the realization of a stable potential response and accurate analysis. The electrode nanostructuration requires less than 6 minutes thanks to the simple and fast electrochemical deposition procedure. A quasi-Nernstian response with a slope of 60.4 mV/decade in the range of interest is obtained when employing these materials in Li^+ ISE. Despite the interesting outcomes, in the following experiments single layers SCs will be used to reduce the fabrication time, as the analytical performance is overall similar to the one of multi-layers.

In Section 3.5, we have described the development of a simple and efficient electrodeposition

procedure for miniaturized electrodes based on LSV, as the classical deposition based on the application of a constant potential is suitable only on macro-electrodes. Two potential windows and successive depositions are investigated and compared. Single-step procedures produce similar morphological features while allowing a simpler fabrication protocol. Although the two LSV depositions produce differently shaped platinum nanoflowers, when used to fabricate a SC-ISE, their electrochemical behaviour is very similar. The capacitance values of the two structures obtained by CRC measurements is almost equal. Furthermore, the value is very close to the one reported in literature for platinum nanostructures on macro-electrodes, which is a highly notable result. All sensors show short response time (~ 15 s) and Nernstian calibration with one-order of magnitude lower detection limit (2.6×10^{-6}) with respect to the micro-electrodes values. Finally, sensor reversibility and stability both in wet and dry conditions are also confirmed. These results demonstrate the possibility to use this exceptional platinum nanomaterial also for applications where electrode miniaturization is critical.

3.7 Main contributions and conclusions

The realization of stable and reproducible SC-ISEs for portable and wearable applications is still a challenge as many unresolved issues still need to be addressed, like biocompatibility, potential stability and reproducibility. This chapter summarizes the research on the production of efficient SCs based on noble metal nanostructures. The main contributions are:

- the fabrication of highly stable all-solid-state Li^+ SC-ISEs exploiting gold and platinum nanostructures by fast electrodeposition procedures;
- a detailed characterization and comparison between gold and platinum nanostructures in terms of morphology and electrochemical behaviour;
- the study of substrate influence, reversibility and stability over time;
- the combination of gold and platinum nanostructures to further improve the SC capacitance, and thus potential stability;
- the development of an alternative fast electrodeposition procedure of platinum nanoflowers on miniaturized sensors.

This technology opens up interesting perspectives in tackling some unresolved aspects of ISEs, like biocompatibility, long-term storage and response stability, for remote monitoring of ions.

Use of nanostructured solid-contact ISEs in healthcare for sweat analysis

This chapter shows the use of the previously discussed SC-ISEs technology in sweat sensing for healthcare. Three areas of applications are tested in this thesis, but the same technology could be easily extended to others. The first section is dedicated to lithium drug monitoring in perspiration for people suffering from psychiatric disorders. Non-invasive monitoring via perspiration analysis is proposed for the first time to avoid the need of frequent check-ups in hospital to optimize and maintain the lithium dose of the patient. Then, the monitoring of heavy metal contamination in people exposed to risky environments is proposed. In the last section, the detection of sweat sodium and potassium is reported to control physical exercise and hydration.

This chapter is divided in three main sections, one for each application: lithium sensing, lead detection and physical exercise monitoring. In all cases, the analytical performance of the all-solid-state ISEs is tested both in aqueous solution and in artificial sweat. The selectivity, reversibility and stability of the ISEs is studied. The integration of these sensors on a flexible electrochemical platform and in a fully wearable system will then be presented in Chapters 5 and 6, respectively.

4.1 Lithium monitoring in mood disorders

4.1.1 Motivation

Lithium represents the most widely used mood stabilizer in psychiatric disorders [101]. Despite its narrow therapeutic window and possible severe side effects, it is still the main drug to treat people suffering from *Bipolar Disorder* (BD). [13]

BD is a potentially mortal condition, which cannot be treated, but only controlled with specific drugs. It affects every year 60 million people worldwide (according to the World Health Organization) and 2.6% of the adult population in the U.S.A. (National Institute of Mental Health)

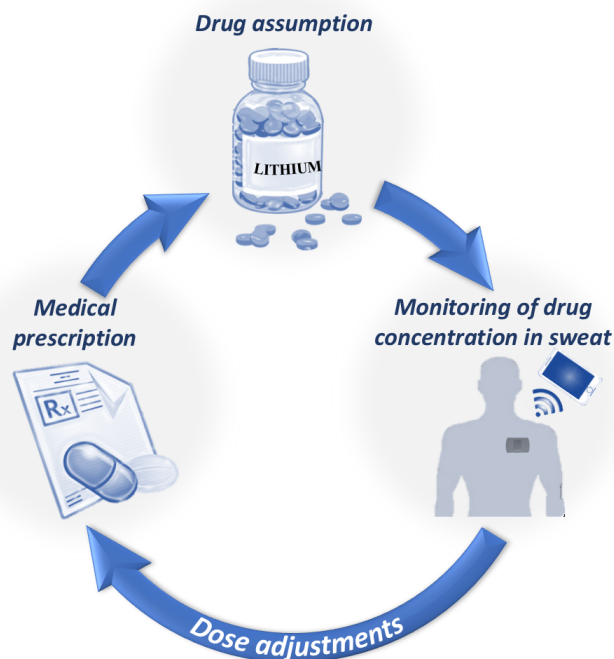


Figura 4.1 – Scheme of the proposed non-invasive approach for Therapeutic Drug Monitoring (TDM) of lithium in sweat. Reprinted with permission from [13]. ©[2018]IEEE

[11]. It is characterized by episodes of depressed and maniac mood, separated by periods of normal mood. Maniac and depressed conditions can cause insomnia or hypersomnia, excessive weight loss/gain, suicidal thoughts, aboulia [102, 103]. The risk of suicide is 30 times higher than in general population [104]. Consequently, after diagnosis, there is an urgent need of stabilization therapy [105]. Unfortunately, the therapeutic range of this compound is very narrow (0.5-1.5 mM) [98]. Moreover, dietary variations, interaction with other medicines as well as individual variability have a strong effect on the determination of the right dose [106]. The consequences of overdose can be extremely severe. They include drowsiness, ataxia, myoclonic twitching and chronic toxicity that can lead to irreversible damages to kidneys, liver and brain, and eventually to death [106]. Hence, Therapeutic Drug Monitoring (TDM) is crucial to optimize the dose for each patient [107]. More specifically, lithium concentration in serum must be controlled at least every week (standardized 12h or 24h Li^+ serum concentration) at the beginning of the treatment or after any change in the dose. The time interval between subsequent check-ups can be enlarged only in absence of any complications. On the contrary, the frequency of serum lithium analyses should be increased accordingly. Check-ups every three months must be performed during maintenance [101].

Lithium quantification in clinical laboratories is routinely performed by atomic absorption spectrometry, flame emission photometry or conventional ISEs [108]. The possibility to use colorimetry [98] and photometry [109, 110] has also been reported in literature [108].

Obviously, all these techniques require highly qualified personnel and expensive equipment. In this regard, all-solid-state SC-ISEs constitute ideal candidates for the development of low-cost and easy-to-use sensors for decentralized monitoring of lithium that would avoid frequent check-ups in hospital to the patients. Novell et al. have reported the fabrication of a paper-based Li^+ ion-selective sensor using carbon nanotubes as SCs [96]. Coldur et al. have fabricated a miniaturized Li^+ ISE with improved selectivity using a graphite composite to achieve ion-to-electron transduction [97]. In the following years they have also reported the determination of lithium under flowing conditions towards the development of automatic and LOC analytical devices [111]. All these sensing systems open up new interesting perspectives, but some limitations must still be tackled, including stability, durability, biocompatibility, toxicity, reproducibility and simplicity of the fabrication process.

Other possible applications of lithium sensors outside healthcare may also arise from the expanding use of lithium-ion batteries that is likely to bring greater environmental exposure through leaching of landfill [112].

In this work a novel approach for non-invasive decentralized monitoring of lithium drug concentration through sweat analysis is proposed for the first time. Chromatographic measurements have demonstrated the correlation between the amount of lithium extracted in sweat and the one present in serum [113]. In particular, the concentration in sweat is about three times higher than the one in blood (2.4 mM - 4.5 mM). Sweat offers several advantages over serum: it is readily accessible without the need of syringes and of invasive procedures, it is highly abundant and can be reproduced artificially following specific standards. A scheme of the proposed non-invasive approach for TDM of lithium in sweat is given in Figure 4.1 [13].

An all-solid-state ISE with a nanostructured SC is used to detect lithium ions in sweat. The sensor offers near-Nernstian behaviour (57.6 ± 2.1 mV/decade) in the concentration range of interest. In addition, it shows fast response (15-30 s), good reversibility and small potential drift over time. A wide pH stability window (pH 4-12) is also proved.

In this chapter the characterization of the performance of the SC lithium sensor in terms of analytical parameters, selectivity and stability in water solution and in artificial sweat will be described. The effect of conditioning will also be investigated. The realization of a fully wearable sensors will then be described in Chapters 5 and 6.

4.1.2 Experimental methods

The experimental details of the fabrication and characterization of Li^+ ISEs are reported below.

Materials

NaCl and NH_4Cl were purchased from Applichem GmbH (Germany). DL-Lactic acid, pyruvic acid and urea were purchased from Acros (United States). Uric acid was purchased from Alfa

Aesar (United States). All other chemicals were purchased from Merck (Germany) [14].

ISM fabrication

The sensors were fabricated as described in Section 3.2.

Artificial perspiration

Artificial sweat was prepared according to the composition reported in Table 4.1 [114].

Tabella 4.1 – Composition of the artificial perspiration solution used in this work.

Compound	Concentration
NaCl	0.34 M
NH ₄ Cl	0.33 M
Acetic acid	0.08 M
DL-Lactic acid	0.20 M
Ascorbic acid	10 μ M
Glucose	0.17 mM
Uric acid	59 μ M
Pyruvic acid	0.18 mM
Glutamic acid	0.37 mM
Urea	10 mM

Morphological and electrochemical characterization

The sensors were characterized as described in Section 3.2.

4.1.3 Experimental results and discussion

All potentiometric measurements were performed using an Autolab potentiostat (Metrohm, Switzerland) controlled by a Nova 1.11 software in a two-electrodes cell setup. A double junction Sension+ 5044 RE (Hach, United States) for use with ISEs was employed in all measurements [11].

Calibration in water

In Section 3.3 we have reported the development and comparison of different nanostructures SCs for all-solid-state ISEs with a one-step electrodeposition of noble metals. This technology offers several advantages over carbon-based SCs and conductive polymers, including fast deposition, biocompatibility and non-toxicity. We proved that these systems have enhanced analytical capabilities in aqueous solutions. While in Section 3.3 we wanted to highlight the SC technology, in this paragraph we focus on their application for lithium monitoring

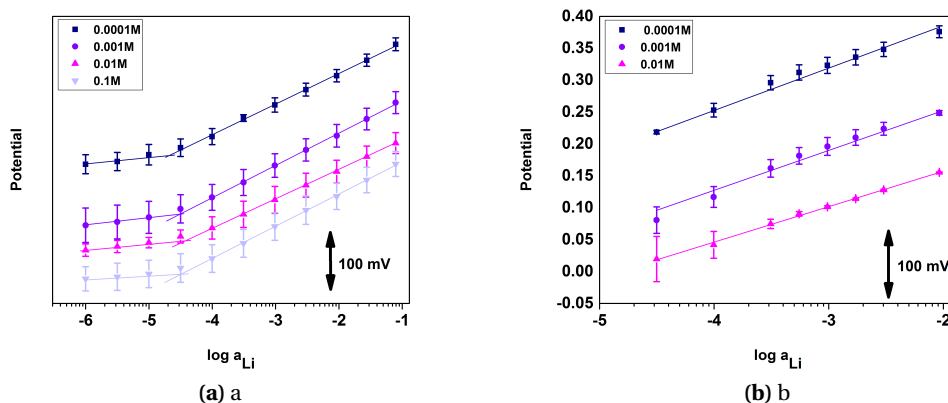


Figura 4.2 – Calibration curves of Li^+ ISEs based on platinum nanostructured SCs after conditioning at different concentrations: a) long range calibration range (between 10^{-6} M and 0.1 M); b) short range calibration around the therapeutic window values. Reprinted with permission from [10].

in healthcare. Platinum nanostructures deposited on platinum substrates were chosen as preferred SCs due to their higher performance and fast deposition procedure.

An example of a typical calibration curve computed from the potentiometric time trace has already been reported in Figure 3.9. The sensor shows a near-Nernstian behaviour with a slope of 58.7 ± 0.8 mV/decade and a LOD of about 1.3×10^{-5} M.

The effect of conditioning concentration on the sensor was also investigated. Figure 4.2a shows the calibration curves between 10^{-7} M and 0.1 M after conditioning at different concentrations for 24 hours. It is possible to conclude that lower concentrations bring the membrane to higher potential ranges, on the contrary to what could be expected. No significant effect on the LOD was found. However, if we repeat the calibration in a narrow concentration range close to the therapeutic window values, the conditioning concentration is found to have a major role in sensor response, as evident from Figure 4.2b. In particular, it is possible to conclude that the 0.01 M LiCl solution improves the linearity of the system and greatly reduces standard deviation, providing improved prediction accuracy. Consequently, this will be the conditioning concentration of choice in following discussion.

Tabella 4.2 – Selectivity coefficient of Li^+ ISEs based on platinum nanostructured SCs for different interfering ions obtained by SSM and FIM in comparison with the highest literature values [10].

	$\text{Log } K_{\text{Li}^+, \text{int}}$			
	K^+	Na^+	NH_4^+	Ca^{2+}
SSM	-2.38 ± 0.25	-2.67 ± 0.23	-2.97 ± 0.21	-3.90 ± 0.08
FIM	-2.56 ± 0.12	-2.55 ± 0.17	-3.08 ± 0.16	-4.01 ± 0.05
Literature by SSM	$-3.34[96]$	$-3.11[96]$	$-3.29[96]$	$-3.36[115]$
Conventional ISE by FIM	$-2.3[116]$	$-2.5[116]$	$-3.1[116]$	$-4.3[116]$

Interference studies

The selectivity of the sensor was investigated by comparing different methods. The values obtained by the SSM and the FIM (see Section 2.5.4) are reported in Table 4.2 in comparison with the highest values reported in literature both for conventional and all-solid-state Li^+ ISEs. For the SSM the procedure described in [117] was used to achieve unbiased selectivity values. Entire calibration curves were taken for each ion to determine their Nernstian range. In the FIM a fixed interfering ion activity of 2.8×10^{-2} was used during all sensor calibrations. To our knowledge, no FIM values for Li^+ SC-ISEs have been reported in literature yet [10].

The Li^+ ISEs presented here show the highest selectivity towards Ca^{2+} ever obtained for SC-ISEs. As expected the lowest selectivity coefficients are the ones for the smallest ions, K^+ and Na^+ , since they have similar dimensions to Li^+ ions, thus giving larger interference. In particular, selectivity values of about 1:450 and 1:180 are achieved in this work for K^+ and Na^+ , respectively. Although lower, than in other works [96], this performance is still acceptable. The selectivity versus NH_4^+ ions is very similar to the highest value reported in literature. In conclusions, all selectivity values are very similar to the ones reported for conventional ISEs.

Testing in artificial sweat

As reported in [11], for the first time we have used these sensors to monitor lithium levels in sweat. The great performance of the fabricated devices in this biological fluid is demonstrated, proving the feasibility of lithium drug monitoring through perspiration analysis.

An example of a typical calibration curve obtained in a perspiration solution is given in Figure 4.3. The corresponding time trace is reported in the small inset. It is possible to observe that very stable and smooth time responses were obtained, with sharp steps after every subsequent lithium addition.

A summary of all analytical parameters and statistics is given in Table 4.3 in comparison with the best values reported in literature. It is possible to notice that the slope of the calibration curve is 57.6 ± 2.1 mV/decade, which demonstrates the near-Nernstian behaviour of the sensor. The higher standard deviation with respect to [10] can be explained by considering that in the present work the calibration is performed in sweat, in the presence of more interactions in solution. The LOD is computed as the intersection of the linear portions of the calibration curve, as prescribed by IUPAC definitions [47]. Although higher with respect to the ones reported in literature for aqueous solutions, this value is still in the concentration window of interest for lithium drug in sweat, that is around three times the corresponding amount in serum [113] (2.4-4.5 mM). In addition, the response time in sweat does not increase with respect to the one obtained in simple LiCl aqueous solutions.

The strongest interference in Li^+ measurements is typically due to sodium ions because of the similar dimensions of this element. The high selectivity of the nanostructured sensors used in this work was already demonstrated in aqueous solution in the previous subsection

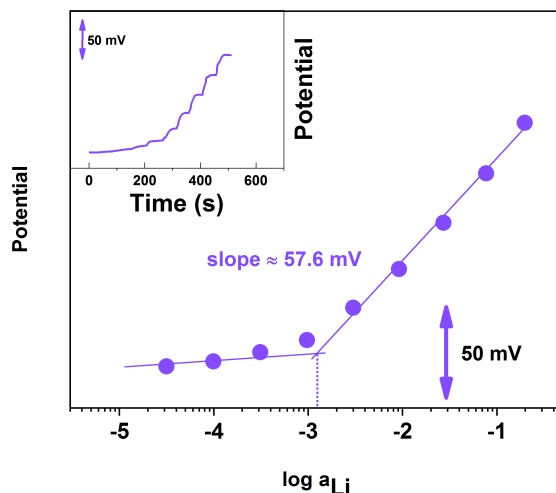


Figure 4.3 – Calibration curve of a Li⁺ SC-ISE in sweat. The inset shows the corresponding time trace. Adapted with permission from [14]. ©[2018]IEEE

Tabella 4.3 – Analytical parameters in sweat of a Li⁺ ISEs based on platinum nanostructured SCs [14].

	Sensitivity [mV/decade]	LOD
Our Li ⁺ sensor (water solution)	58.7±0.8	$(13.0 \pm 4.0) \times 10^{-6}$
Our Li ⁺ sensor (artificial sweat)	57.6 ± 2.1	$(13.5 \pm 2.1) \times 10^{-4}$
Literature Li ⁺ sensors (water solution)	59.8±1.4 [97]	5×10^{-6} [111]

towards all most important ions (Na⁺, K⁺, Ca²⁺, Mg²⁺, NH₄⁺) using both the SSM and FIM. The quasi-Nernstian calibration obtained in the present study in the presence of a large amount of sodium ions and of several other compounds in sweat confirms our previous findings.

An important element to allow proper measurements in sweat is sensor stability over sweat pH, since the acidity of perspiration is subjected to personal and environmental variability. The typical sweat pH value ranges from 4.5 to 7 [6]. The stability window versus pH of the sensor was measured by exposing the sensor to sweat at a constant lithium concentration of 10⁻² M, but with different acidity. The sensor response is stable in the window of pH 4-12, thus proving the suitability of the fabricated ISE for sweat analysis. This property is extremely important to allow simple data interpretation and offers an important advantage over other pH-sensitive techniques.

The potential shown by the sensor when exposed to a constant concentration of lithium ions in sweat was compared to the value obtained by the calibration curve to analyze the predictive capability of the sensor. A percentage difference smaller than 4% was always found, thus corroborating the good stability of the sensor.

The dynamic response of the sensor in the perspiration solution was investigated by per-

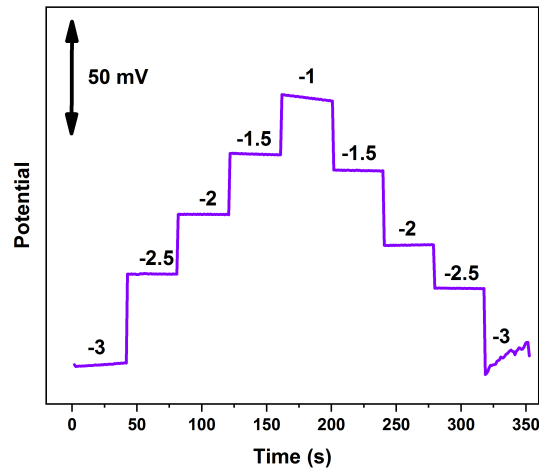


Figura 4.4 – Reversed calibration in the range $10^{-3} - 10^{-1}$ M of a Li^+ SC-ISE in sweat. Adapted with permission from [14]. ©[2018]IEEE

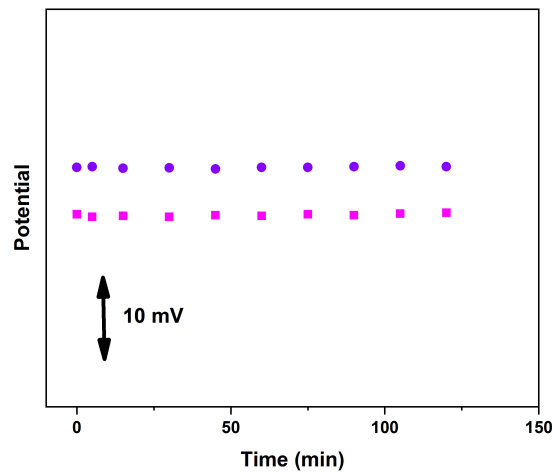


Figura 4.5 – Sensor stability over time when exposed to sweat with 10 mM NaCl. The two curves correspond to the responses of two distinct electrodes. Adapted with permission from [14]. ©[2018]IEEE

ming a reversed calibration in the range $10^{-3} - 10^{-1}$ M. The resulting curve is reported in Figure 4.4. It is possible to see that the fabricated all-solid-state ISEs offer an exceptional potential stability and reversibility in sweat. Moreover, the small potential drift is evident also from the potential measurements over a prolonged period of time when the sensor is placed in perspiration solution with a constant lithium concentration (Fig. 4.5). A concentration of 0.01 M LiCl in sweat was used for this experiment.

Based on these results, the integration of this sensor in a wearable smart patch for sweat analysis will certainly offer a new promising and non-invasive approach for home-monitoring of lithium drug therapy directly on the skin.

4.1.4 Summary

In this section, the novel idea of monitoring lithium drug concentration by non-invasive means through sweat analysis directly on the skin is proposed. The feasibility of lithium ions detection in perspiration solution is proved. A quasi-Nernstian (57.6 ± 2.1 mV/decade) calibration curve is obtained in the concentration range of interest for this application. Furthermore, we demonstrate that the fabricated sensors offer good reversibility and pH stability (pH 4-12) in sweat. A very short response time (15-30 s) and small potential drift are also achieved. The integration of these sensors in a wearable smart patch will certainly represent an important step towards a better personalized healthcare and a new non-invasive way for decentralized monitoring of lithium drug therapy for people suffering from BD.

4.2 Monitoring of heavy metal contamination

4.2.1 Motivation

Sweat is a promising alternative sample also in the field of xenometabolics, that is the investigation of the presence of metals in the organism due to absorption from the external environment [25]. The main sources of xenometals are food and dermal absorption [118]. Among them, lead and arsenic are one of the most harmful because of their known carcinogenic effect and their heavy repercussions on several body systems. The first one is especially dangerous for the brain. Acute lead poisoning can cause pain, tingling and numbness, memory and behavioural problems. All these effects can be permanent.

Lead is a trace metal in sweat in normal conditions. It can enter the human body through contaminated food, water or environment. This very toxic and dangerous element can be found in lead-based paintings, gasoline products, dust, contaminated food. Once ingested, poisoning is not immediate, but occurs over several months or even years.

Interestingly, it has been shown in some papers that lead is excreted in sweat in same or even larger amount than in urine or in blood [119–121]. While normal sweat levels should be below $283 \mu\text{g/L}$ (that correspond to about $1.4 \mu\text{M}$), in exposed workers the amount can reach values around $17\,700 \mu\text{g/L}$ ($\sim 85.4 \mu\text{M}$) [119]. Lead adsorption might come from skin adsorption when the cleaning protocols are not sufficient.

Hence, perspiration analysis could represent not only an equivalent, but even a better sample biofluid than blood for monitoring of lead absorption compared to the most commonly used urine and blood.

Current research on solid-state Pb^{2+} ISEs is very limited. The use of a thick PVC membrane with lead ionophore III is reported in [122]. The authors propose the use of non-functionalized porous glassy carbon leaded with the membrane cocktail for the detection. Picomolar detection is achieved with this technology, with reduced deterioration. A new membrane cocktail is proposed in [123]. Nanomolar detection and good analytical performance is obtained. The most complete characterization of a solid-state Pb^{2+} ISE is given in [124]. In this paper, they employ for the first time poly(2-methoxy-5-(2-ethylhexyloxy)-p-phenylene vinylene) (MEH-PPV) as SC. The good ion-to-electron transduction is proved by CRC and *Electrochemical Impedance Spectroscopy* (EIS). The sensors show Nernstian response and subnanomolar LOD with no water film formation.

All the Pb^{2+} ISEs reported in literature are tested for their application in water quality monitoring. In this work, we propose for the first time the use of our nanostructured SC-ISEs to monitor heavy metal contamination in people exposed to risky environments through the analysis of their sweat. In particular, we will use lead as example heavy metal ion.

As for the other ions, this section focuses on the characterization of the analytical parameters, selectivity and stability in water solution and in artificial sweat, while the integration on a flexible and wearable system is described in the following chapters.

4.2.2 Experimental methods

The experimental details of the fabrication and characterization of Pb^{2+} ISEs are reported below.

Materials

All chemicals were purchased from Merck (Germany).

ISM fabrication

The sensors were nanostructured as described in Section 3.2. 100 mg of membrane cocktail were prepared in 1 ml of THF with the following composition: 1% of tert-Butylcalix[4]arene-tetrakis(N,N-dimethylthioacetamide) (Lead ionophore IV), 0.44% of Sodium tetrakis[3,5-bis(trifluoromethyl)phenyl]borate (NaTFPB), 32.52% of PVC, 65.04% of 2-Nitrophenyl octyl ether (o-NPOE) and 1% of Tetradodecylammonium tetrakis(4-chlorophenyl)borate (ETH500). A 10 μl drop of membrane cocktail was drop-cast on the electrodes and left to dry overnight. The sensors were conditioned in 10 mM $\text{Pb}(\text{NO}_3)_2$ unless otherwise stated.

Artificial perspiration

Artificial sweat was prepared as described in Section 4.1.2.

Electrochemical characterization

The sensors were characterized as described in Section 3.2.4.

4.2.3 Experimental results and discussion

Calibration in water

Ten samples were prepared and calibrated after a one day conditioning in a 1 mM or in a 10 mM $\text{Pb}(\text{NO}_3)_2$ solution. An example of a typical calibration curve is given in Figure 4.6 after conditioning in 1 mM $\text{Pb}(\text{NO}_3)_2$. The effect of different concentrations of the conditioning solutions on the sensor performance was investigated. The resulting analytical parameters are reported in Table 4.4.

Despite the difficulty to realize the lead membrane, in terms of suitable percentage weights for the cocktail ingredients, we reached out good results for the sensitivity and LOD. All calibrated samples showed smooths and quasi-linear curves, close to the theoretical value, exhibiting a Nernstian slope of 24.3 ± 3.9 mV/decade at low conditioning and 29.5 ± 4.9 mV/decade at high conditioning. Despite the sensitivity is close to the theoretical value in both cases, the conditioning has a strong effect on the value of the LOD. In particular, a LOD lower of about a half-decade (9.31×10^{-7}) is achieved at low conditioning concentration with respect to the one at high $\text{Pb}(\text{NO}_3)_2$ concentration (5.17×10^{-6}). As expected, the conditioning is crucial to achieve the best LOD.

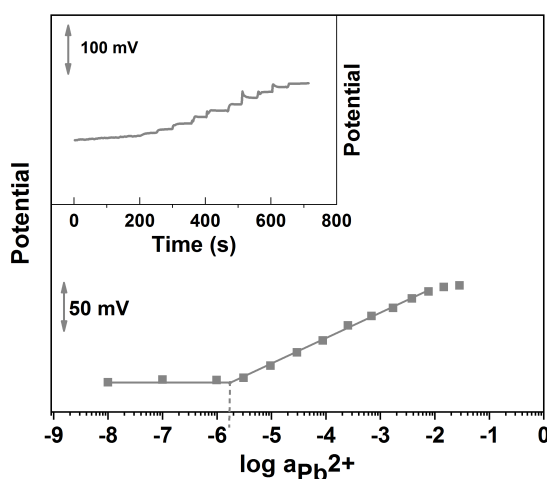


Figure 4.6 – Calibration curve of a Pb^{2+} SC-ISE in aqueous solution. The inset shows the corresponding time trace.

Tabella 4.4 – Effect of conditioning concentration on the analytical parameters of Pb^{2+} SC-ISEs.

	Sensitivity [mV/decade]	LOD
Conditioning in 1 mM $\text{Pb}(\text{NO}_3)_2$	24.3 ± 3.9	$(9.31 \pm 5.57) \times 10^{-7}$
Conditioning in 10 mM $\text{Pb}(\text{NO}_3)_2$	29.5 ± 4.9	$(5.17 \pm 1.44) \times 10^{-6}$

Interference studies

The selectivity of the sensors was investigated by interference studies. Both SSM and FIM (see Section 2.5.4) were tried for the determination of the selectivity coefficients. However, the second method was found to be not suitable for a proper determination of the coefficients. The obtained SSM coefficients allow us to conclude that our sensor is very selective towards lead ions, although the obtained values are slightly higher than the lowest ones reported in literature.

Tabella 4.5 – Selectivity coefficient of Pb^{2+} ISEs based on platinum nanostructured SCs for different interfering ions obtained by SSM and FIM in comparison with the literature values.

	$\text{Log } K_{\text{Pb}^{2+}, \text{int}}$					
	K^+	Na^+	NH_4^+	Mg^{2+}	Ca^{2+}	Li^+
This work by SSM	-1.64 ± 0.90	-2.89 ± 0.68	-2.76 ± 0.13	-3.76 ± 0.54	-4.28 ± 0.44	-2.9 ± 0.43
Literature by SSM	-5.6 [123]	-5.8 [123]	-2.12 [123]	-6.2 [123]	-6.2 [124]	-5.6 [123]
Conventional ISE by SSM	-4.3 [125]	-3.5 [125]	n.a.	-5.0 [125]	-4.8 [125]	-3.5 [125]

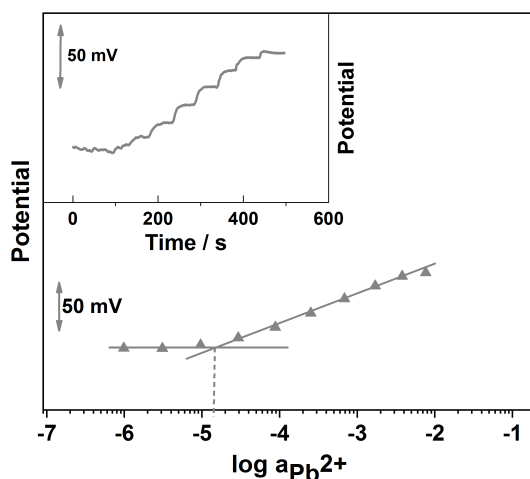


Figura 4.7 – Calibration curve of a Pb^{2+} SC-ISE in sweat. The inset shows the corresponding time trace.

4.2. Monitoring of heavy metal contamination

Tabella 4.6 – Analytical parameters in artificial sweat of a Pb^{2+} ISEs based on platinum nanostructured SCs.

	Sensitivity [mV/decade]	LOD
Our Pb^{2+} sensor (water solution)	24.3 ± 3.9	$(9.31 \pm 5.57) \times 10^{-7}$
Our Pb^{2+} sensor (artificial sweat)	28.9 ± 1.64	$(14.30 \pm 5.13) \times 10^{-6}$
Literature Pb^{2+} sensors (water solution)	29.1 ± 0.8 [124]	6.3×10^{-10} [124]

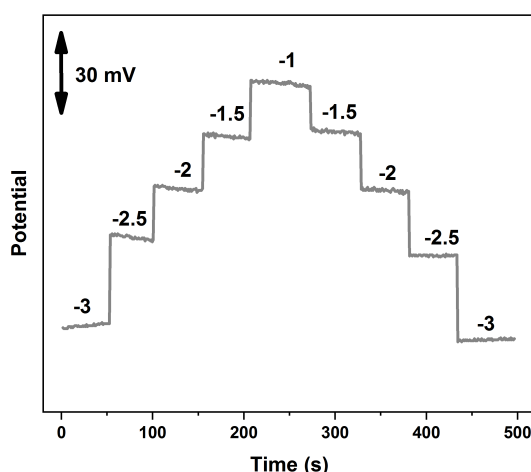


Figura 4.8 – Reversed calibration in the range $10^{-3} - 10^{-1}$ M of a Pb^{2+} SC-ISE in sweat.

Testing in artificial sweat

In this section we propose for the first time the monitoring of heavy metal contamination, in particular of lead, in sweat. A good analytical performance is proven.

The calibration curve of a Pb^{2+} SC-ISE in sweat after a one day conditioning in 1 mM $\text{Pb}(\text{NO}_3)_2$ is given in Figure 4.7. The corresponding time trace from which the curve was calculated is reported in the small inset on the top left corner. Sharp steps and stable responses are achieved after each lead addition.

A summary of the analytical parameters obtained from the calibration curves of five different samples is given in Table 4.6. A quasi-Nernstian slope is achieved with a LOD of about $(14.30 \pm 5.13) \times 10^{-6}$. As expected, this value is higher than the one obtained in aqueous solution ($(0.93 \pm 5.56) \times 10^{-6}$) due to the presence of a much larger number of interactions in the artificial sweat. On the contrary the sensitivity values are comparable and even slightly better than the ones reported in water solution. The LOD is slightly higher with respect to the one reported in literature in water, but it is still falling in the detection range of interest. However, some improvements might be required to achieve higher accuracy. This can be done by proper tuning of the conditioning procedure or by slight variations of the membrane

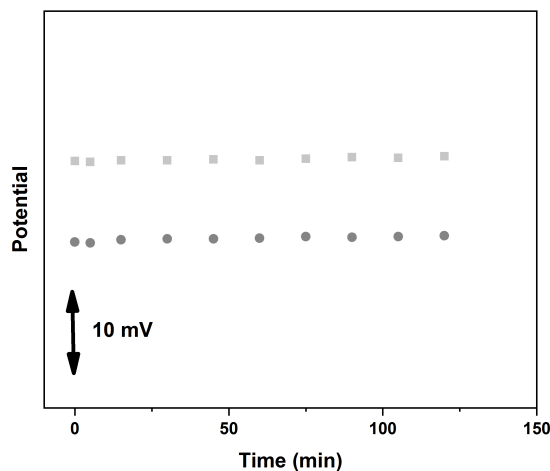


Figura 4.9 – Sensor stability over time when exposed to sweat with 1 mM $\text{Pb}(\text{NO}_3)_2$. The two curves correspond to the responses of two distinct electrodes.

cocktail composition.

Sensor reversibility was proved by subsequent increases and decreases of ion concentration over time between 10^{-3} and 10^{-1} M $\text{Pb}(\text{NO}_3)_2$ in artificial sweat (Figure 4.8). The obtained curve has sharp steps with similar potential values for a given concentration.

The stability of the sensor potential over a prolonged period of time was also proved, as reported in Figure 4.9. A 1 mM 10^{-1} M $\text{Pb}(\text{NO}_3)_2$ in artificial sweat was used for the measurement.

4.2.4 Summary

In this section, the monitoring of the exposure to heavy metal contamination through sweat analysis in people exposed to risky environments is proposed for the first time. It was proved that lead detection in artificial sweat is possible with good analytical results ($\text{LOD} \approx (14.30 \pm 5.13) \times 10^{-6}$), excellent reversibility and small potential drift over time. These results certainly open interesting perspectives in the non-invasive monitoring of heavy metal contamination directly on the skin.

4.3 Monitoring of physical exercise

4.3.1 Motivation

Perspiration is a crucial element of our thermoregulatory system, especially during sport activity. However, athletes lose water and electrolytes while sweating. Therefore, a proper replacement through food and beverages is crucial for a normal body function [126].

The centres for Diseases control and Prevention recommends an average sodium intake for children over 2 years old and adults lower than 2300 mg per day. Nonetheless this value strongly depends on the level of sport activity. Both a low and a high sodium intakes could be harmful for the body. A low amount of sodium could cause cells inflammations, that might lead to chronic headaches, fatigue, nausea, seizures or decreased consciousness. On the contrary, a excess of this electrolyte may produce higher water retention, which could result in high blood pressure, hypernatremia (that is a high concentration of sodium in the blood) and eventually kidney failure. In fact kidney filter out excess sodium and other toxins from our body. If the amount of sodium is higher than their filtering capability, this salt will accumulate in the blood, causing hypernatremia and kidney failure [126–128].

This disease might be treated by restoring the sodium balance by uptake of proper fluids. If high blood concentrations are not treated properly, confusion and muscles spasms might arise, ultimately leading to death [126–128].

According to the research reported in [127], sodium ion concentration in sweat is up to 70 mM in normal conditions. This values is lowered to 40 mM in infants. There is no significant difference with age or sex. Adults with chronic bronchitis or bronchiectasis exhibit the same range. Another work [126] showed that thermoregulatory strain increases sweat production in order to promote evaporative cooling and induce homeostatic thermoregulation. Sweat composition was found to be in the range 12-105 mM. In [128], 157 experiences runners (141 men and 16 women) completed a marathon race at $24.4 \pm 3.2^{\circ}\text{C}$ and $27.7 \pm 4.8\%$ of humidity. Sweat patches were put on the athletes' harm of collect the samples. Photoelectric flame photometry was used to determine the concentration of sodium. Values between 7 and 95 mM were found.

It is possible to conclude that literature does not set a common value of sodium concentration in perspiration. Slightly different ranges have been found in different works as a consequence of the different types of patients and environments. In general, a mean sodium concentration of about 50 -60 mM can be considered [128, 129].

Potassium is another key electrolyte for our body balance. Low potassium levels could cause muscles cramping and cardiovascular problems. Consequently, a proper diet must be planned, especially in people experiencing often cramps during workouts. In addition, this mineral reduce the risk of blood clotting and help the maintenance of pH balance and blood pressure. Furthermore, it is responsible for carrying nutrients to the cells, protecting the stomach lining from damages due to acids. At last, it promotes heart and bones health and regulates the muscular and nervous systems [128, 129].

Almost 70% of the potassium in our body is found in our bodily fluids like plasma, blood and sweat, while the remaining amount is stored in our bones. Hard exercise can cause high potassium loss through perspiration. Consequently, it is crucial to control the level of this mineral, especially in people doing intense physical activity [128, 129].

Only a few examples of potassium monitoring in sweat are reported in literature. An example is the already mentioned work on experienced runners [128]. Potassium levels around 3 and 8 mM have been found.

It is well known that sweat rate and composition varies considerably within and among individuals. Although some tests have already been performed on athletes to determine sweat water and electrolytes losses during physical exercise, no concrete relationship between sweating levels and sodium or potassium intake has been established so far. The individual's sweating depends on genetics, body temperature and activity. Despite this, the monitoring of sodium levels is important in people with health concerns or doing intense physical activity [128, 129].

4.3.2 Experimental methods

The experimental details of the fabrication and characterization of K⁺ and Na⁺ ISEs are reported below.

Materials

All chemicals were purchased from Merck (Germany).

ISM fabrication

The sensors were nanostructured as described in Section 3.2. 100 mg of membrane cocktail were prepared in 1 ml of THF with the following compositions: 1% of valinomycin (Potassium ionophore I), 0.50% of Potassium tetrakis(4-chlorophenyl)borate, 33.00% of PVC and 65.50% of Bis(2-ethylhexyl) sebacate (DOS) for the K⁺-selective membrane; 0.7% of Sodium ionophore X, 0.2 wt% Potassium tetrakis(4-chlorophenyl)borate, 33.00% of PVC and 66.10 wt% 2-Nitrophenyl octyl ether (o-NPOE). A 10 µl drop of membrane cocktail was drop-cast on the electrodes and left to dry overnight. The sensors were conditioned in 10 mM KCl and NaCl, respectively, unless otherwise stated.

Artificial perspiration

Artificial sweat was prepared as described in Section 4.1.2.

Electrochemical characterization

The sensors were characterized as described in Section 3.2.4.

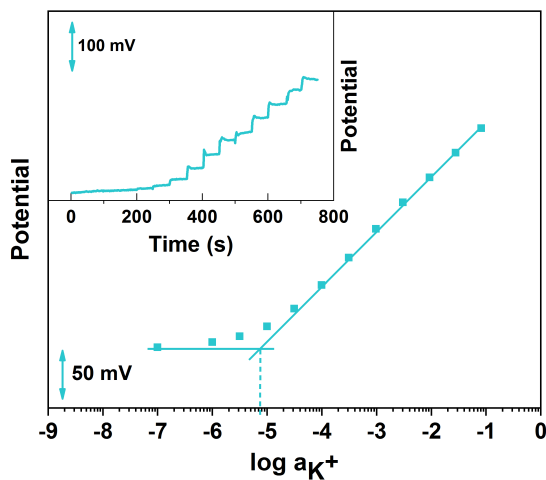


Figura 4.10 – Calibration curve of a K^+ SC-ISE in aqueous solution. The inset shows the corresponding time trace.

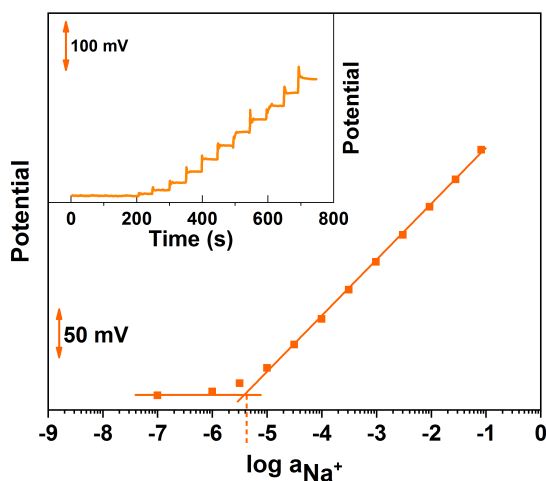


Figura 4.11 – Calibration curve of a Na^+ SC-ISE in aqueous. The inset shows the corresponding time trace.

4.3.3 Experimental results and discussion

Calibration in water

Both Na^+ and K^+ ISEs with platinum nanostructured SCs were fabricated as described in the previous section. After a proper conditioning, the sensors were calibrated by subsequent additions of NaCl and KCl in water solution. An example of a typical calibration curve for a K^+ and a Na^+ ISEs is reported in Figure 4.10 and 4.11 after conditioning in 10 mM KCl and NaCl,

Capitolo 4. Use of nanostructured solid-contact ISEs in healthcare for sweat analysis

respectively. The small inset on the top left reports the corresponding time trace from which the calibration curves were computed.

Tabella 4.7 – Effect of conditioning concentration on the analytical parameters of K^+ SC-ISEs.

	Sensitivity [mV/decade]	LOD
Conditioning in 1 mM KCl	56.1 ± 4.4	$(3.83 \pm 0.76) \times 10^{-6}$
Conditioning in 10 mM KCl	56.4 ± 0.27	$(10.30 \pm 5.32) \times 10^{-6}$

Tabella 4.8 – Effect of conditioning concentration on the analytical parameters of Na^+ SC-ISEs.

	Sensitivity [mV/decade]	LOD
Conditioning in 1 mM NaCl	56.7 ± 0.4	$(7.77 \pm 6.32) \times 10^{-6}$
Conditioning in 10 mM NaCl	56.9 ± 0.8	$(14.90 \pm 7.33) \times 10^{-6}$

As discussed in the previous section for the other ions, the conditioning procedure is crucial to ensure proper functioning in the range of interest. For this reason, two conditioning concentrations were tested and compared for both ions: a one day conditioning in a 1 mM solution of target analyte was performed on 5 samples, while a 10 mM solution was used for the others.

The computed analytical parameters obtained with different conditioning concentrations are reported in Table 4.7 for K^+ SC-ISEs and 4.8 for Na^+ SC-ISEs. Both ISEs show near-Nernstian slope (~ 56 -57 mV/decade). No significant effect of the conditioning procedure on the sensitivity values and its standard deviation is found. On the contrary, the LOD is evidently affected by the concentration of the conditioning solution both for K^+ and Na^+ SC-ISEs. In particular, the LOD is about half a decade smaller with reduced standard deviation values when a low concentration solution is used. Consequently, this conditioning procedure will be preferred in subsequent experiments unless otherwise stated.

Tabella 4.9 – Selectivity coefficient of K^+ ISEs based on platinum nanostructured SCs for different interfering ions obtained by SSM and FIM in comparison with the literature values.

	Log $K_{K^+,int}$				
	Na^+	NH_4^+	Mg^{2+}	Ca^{2+}	Li^+
This work by SSM	-1.83 ± 1.22	-1.16 ± 1.31	-2.41 ± 1.32	-7.49 ± 0.47	-2.61 ± 1.10
Literature by SSM [60]	-4.7	-2.0	-6.7	-7.8	-4.6
This work by FIM	-1.80 ± 0.07	-1.68 ± 0.10	-3.32 ± 0.04	-	-1.91 ± 0.39
Literature by FIM [4, 55]	-4.6	-2.1	-3.9	-4.6	-3.6
Conventional ISE by FIM [130]	-4.1	n.a.	-5.2	-5.7	n.a.

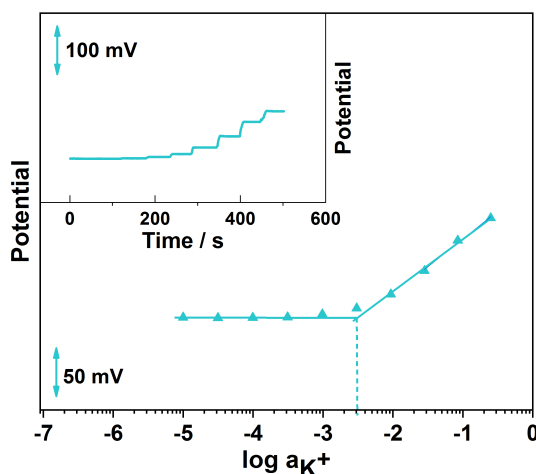
Tabella 4.10 – Selectivity coefficient of Na^+ ISEs based on platinum nanostructured SCs for different interfering ions obtained by SSM and FIM in comparison with the literature values.

	$\text{Log } K_{\text{Na}^+, \text{int}}$				
	K^+	NH_4^+	Mg^{2+}	Ca^{2+}	Li^+
This work by SSM	-2.38 ± 0.25	-2.97 ± 0.21	-4.97 ± 0.39	-3.4 ± 0.08	-2.67 ± 0.23
Literature by SSM [131]	-4.8	-4.9	-3.3	-3.2	-3.0
This work by FIM	-2.20 ± 0.12	-1.89 ± 0.13	-3.56 ± 0.16	-	-2.58 ± 0.06
Literature by FIM [132]	-1.8	n.a.	-3.8	-3.5	-3.1
Conventional ISE by FIM [133, 134]	-3.63	-3.22	-4.67	-3.11	-3.20

Interference studies

As for the other ions, the selectivity of the sensor was investigated by comparing different methods. The values obtained by the SSM and the FIM (see Section 2.5.4) are reported in Table 4.9 and 4.10 in comparison with the highest values reported in literature both for conventional and all-solid-state K^+ and Na^+ ISEs. For the SSM the procedure described in [117] was used to achieve unbiased selectivity values. Entire calibration curves were taken for each ion to determine their Nernstian range. In the FIM a fixed interfering ion activity of 2.8×10^{-2} was used during all sensor calibrations.

High selectivity is achieved both for Na^+ and K^+ ISEs against all most common ions. With the exception of a few values, in general both SSM and FIM coefficients are comparable with the lowest literature values and with the ones of conventional ISEs. As expected, the highest interference is due to Na^+ and K^+ for K^+ and Na^+ ISEs, respectively. This is due to the similar dimensions of the ions.

**Figura 4.12** – Calibration curve of a K^+ SC-ISE in sweat. The inset shows the corresponding time trace.

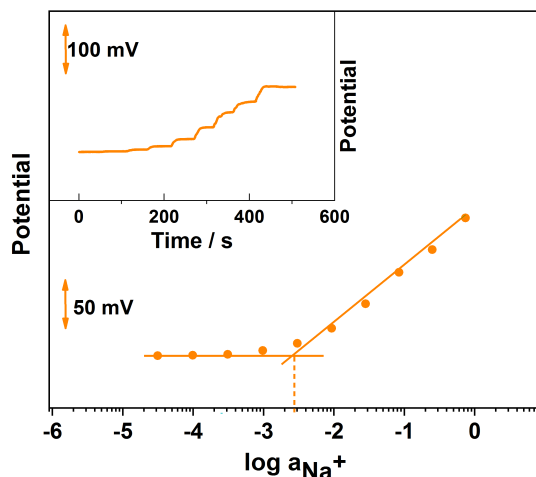


Figura 4.13 – Calibration curve of a Na⁺ SC-ISE in sweat. The inset shows the corresponding time trace.

Tabella 4.11 – Analytical parameters in artificial sweat of a K⁺ ISEs based on platinum nanostructured SCs.

	Sensitivity [mV/decade]	LOD
Our K ⁺ sensor (water solution)	56.1±4.4	$(3.83 \pm 7.64) \times 10^{-6}$
Our K ⁺ sensor (artificial sweat)	55.1±0.9	$(3.10 \pm 0.10) \times 10^{-3}$
Literature K ⁺ sensors (water solution)	58.1 [4]	4.10×10^{-6} [4]

Tabella 4.12 – Analytical parameters in artificial sweat of a Na⁺ ISEs based on platinum nanostructured SCs.

	Sensitivity [mV/decade]	LOD
Our Na ⁺ sensor (water solution)	56.7±0.41	$(7.77 \pm 6.32) \times 10^{-6}$
Our Na ⁺ sensor (artificial sweat)	58.8±1.4	$(4.13 \pm 0.23) \times 10^{-3}$
Literature Na ⁺ sensors (water solution)	59.4 [132]	3.16×10^{-6} [132]

Testing in artificial sweat

Figures 4.12 and 4.13 shows the calibration curve of a K⁺ SC-ISE and Na⁺ in sweat after a one day conditioning in 1 mM KCl and 1 mM NaCl, respectively. The corresponding time trace from the calibration curves were obtained are reported in the small inset on the top left corner of each graph. Sharp steps and stable responses over time are achieved in both cases after analyte addition.

A summary of the analytical parameters obtained from the calibration curves of five different samples is given in Tables 4.11 and 4.12. In both cases, quasi-Nernstian slopes are attained by the sensors. The presence of more interactions in artificial sweat with respect to aqueous

solutions results in a slightly higher standard deviation for the sensitivity for Na^+ ISEs, while no effect is evident on K^+ ISEs.

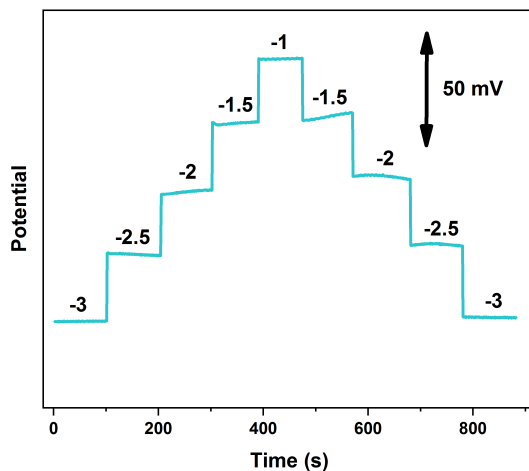


Figura 4.14 – Reversed calibration in the range $10^{-3} - 10^{-1}$ M of a K^+ SC-ISE in sweat.

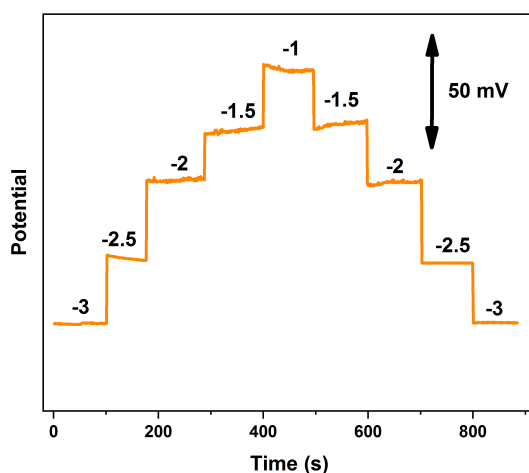


Figura 4.15 – Reversed calibration in the range $10^{-3} - 10^{-1}$ M of a Na^+ SC-ISE in sweat.

On the contrary, the LOD is highly affected by the presence of other compounds in solution. In particular, a reduction of about three orders of magnitude is observed when measuring in artificial sweat with respect to aqueous solution. The LODs in water solution for both K^+ ($(3.83 \pm 7.64) \times 10^{-6}$) and Na^+ ($(7.77 \pm 6.32) \times 10^{-6}$) are similar to the ones reported in literature. No values in artificial sweat have been found for comparison. However, the obtained values ($(4.67 \pm 1.16) \times 10^{-3}$ K^+ and $(4.13 \pm 0.23) \times 10^{-3}$ for Na^+) are below the average physiological

concentration ranges (51 mM for Na^+ and 5.5 mM for K^+). Some improvements might be useful to improve the measurement accuracy, especially for K^+ sensors. In this regard, the conditioning procedure might be properly tuned to lower further the LOD.

The sensor calibrations forward and backward for both ISEs are reported in Figures 4.14 and 4.15 between 10^{-3} and 10^{-1} M KCl and NaCl solutions. Sharp steps and similar potential levels are attained in both cases.

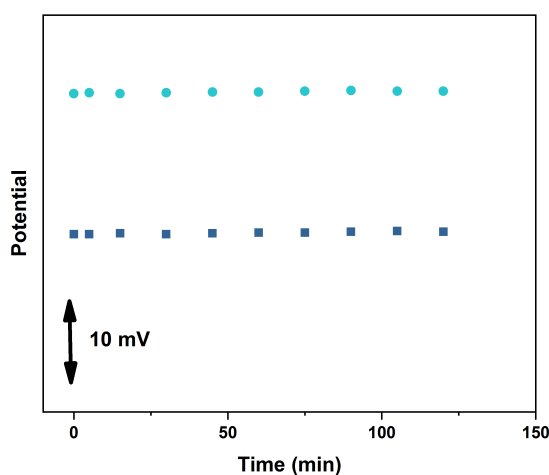


Figura 4.16 – Sensor stability over time when exposed to sweat with 10 mM KCl. The two curves correspond to the responses of two distinct electrodes.

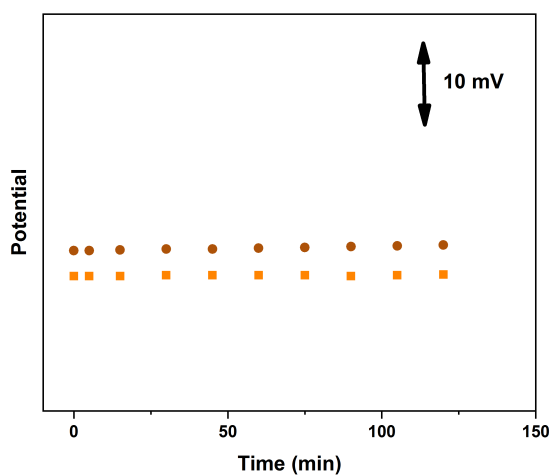


Figura 4.17 – Sensor stability over time when exposed to sweat with 10 mM NaCl. The two curves correspond to the responses of two distinct electrodes.

The stability of the K^+ and Na^+ ISEs over time was also tested with good results, as proved by Figures 4.16 and 4.17. A 10 mM KCl and NaCl solutions are respectively used for the measurements.

4.3.4 Summary

In this section, the proposed nanostructured SC-ISEs are successfully used for the detection of potassium and sodium in artificial sweat for monitoring of physical exercise. The sensors offer Nernstian response, with LODs below the average physiological concentration ranges ($(4.67 \pm 1.16) \times 10^{-3} K^+$ and $(4.13 \pm 0.23) \times 10^{-3}$ for Na^+). The potential signals show high reversibility and stability over a prolonged period of time in both cases.

4.4 Main contributions and conclusions

This chapter describes the use of the developed nanostructured SC-ISEs in sweat sensing for healthcare. Four target ions have been chosen for different applications. The main contributions are:

- the development for the first time of an efficient lithium sensors for TDM in sweat of people suffering from psychiatric disorders;
- the fabrication of a novel lead sweat sensor to control heavy metal contamination in people exposed to risky environment;
- the realization of sodium and potassium ISEs for physical exercise monitoring via perspiration analysis;
- calibrations both in water and artificial sweat were performed in all cases;
- quasi-Nernstian responses were always found;
- the effect of the conditioning concentration was investigated to optimize sensor performance;
- the selectivity of each ISE was analyzed by comparing the coefficients obtained by SSM and the FIM;
- good values were found for every sensor in comparison with the literature ones;
- reversibility and potential stability over a prolonged period of time was proved for all four ions in artificial perspiration.

In this work, the monitoring of lithium drug via sweat analysis is proposed for the first time to optimize and maintain the patients' dose without the need of hospitalization. The feasibility

Capitolo 4. Use of nanostructured solid-contact ISEs in healthcare for sweat analysis

of the measurement is proved by testing in artificial perspiration. Similarly, we propose an innovative method to monitor the exposure to heavy metals of people in risky environments. The lead concentration is measured in artificial sweat with great analytical performance. Finally, the monitoring of sodium and potassium in artificial perspiration is also proven.

Fabrication of a flexible electrochemical platform

Conventional macroscopic and rigid electrochemical cells are hard to be used in wearable sensors. Conformability and miniaturization are indeed two essential components to ensure proper wearability, higher electrodes density and smaller samples volumes. The fabrication of an electrochemical multi-sensing platform on a flexible substrate is a convenient solution to address these challenges. However, its realization involves the addressing of several challenges, like high mechanical resistance, elevated signal-to-noise ratio and absence of exfoliation issues.

In this chapter, the design and fabrication of a flexible multi-sensing platform by means of lithographic processes are described. The good electrochemical performance of the electrochemical cells is proved. The realization of different flexible REs by proper modification of the electrode surface is also discussed. Finally, an integrated temperature sensor is fabricated and calibrated.

5.1 Microfabrication of a flexible integrated platform

The design of an electrochemical sensing platform must consider several aspects depending on the specific application. The geometry and placement of the electrodes must be carefully conceived to ensure optimal functionality. The process flow must be compatible with the proposed materials and design, while enabling high reproducibility.

In the Section 5.1.1, the main design constraints are discussed. In the following one, the design of the first platform prototype is described. In the third part, a detailed explanation of the steps of the process flow is given.

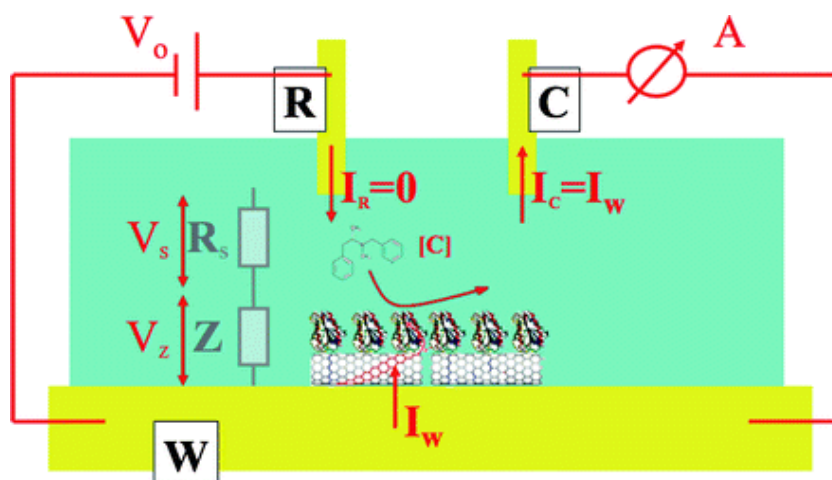


Figura 5.1 – Working principle of a three-electrodes electrochemical cell with nano-biostructures. Reprinted with permission from [15].

5.1.1 Design constraints

Electrode geometry

It is well known that electrode geometry strongly affects the sensing performance [135]. In particular, square electrodes produce border effects, causing a reduction of the effective active surface area of the sensor. Consequently, round geometries are considered in this work to achieve optimal signal distribution.

The WE area is a key property of the electrodes. Smaller electrodes ensure a reduction of the signal-to-noise ratio. Moreover, they are more difficult to be functionalized as very small amounts of fluids must be dispensed. In addition, smaller dimensions results very often in smaller contacts pitches, that lead more easily to crosstalk from the neighbouring wires. Therefore, in this work a WE diameter of 4 mm (electrode area of 12.56 mm^2) is chosen initially to have a surface area similar to the SC-ISEs fabricated on rigid substrates (described in Chapters 3 and 4). Afterwards, smaller dimensions will be tested to enable further miniaturization.

The RE geometry is less crucial than the one of the WEs. In general, larger dimensions should lead to more stable signals. However, this must be a trade-off with miniaturization to ensure good wearability of the sensors. In this work, we will consider initially macro REs with diameters of 4 mm [136].

In our experiments, a two-electrodes setup is used as the current flowing during the potentiometric measurements is negligible. Consequently, there is no need to use a *Counter Electrode* (CE) to collect the current.

Electrodes placement

The proper placements of the electrodes on the platform is essential to achieve reliable measurements. It is evident from Figure 5.1 that the effective voltage between the WE and the RE is $V_z = V_0 - V_s$, where V_0 is the potential applied by the potentiostat and V_s is the IR drop due to electrolyte solution. It is important to minimize this voltage drop V_s in order to control carefully the energy provided to the electrochemical cell. This is achieved by ensuring that the RE does not conduct any current ($I_R = 0$) to avoid polarization phenomena. During the platform design, it is possible to minimize this effect by reducing the distance between the WE and the RE. In this way, the resistance of the electrolyte between the two electrodes is lowered, thus reducing the contribution of V_s [15].

In addition, the placement of all electrodes must be carefully considered in order to maximize the sensor density and avoid waste of space on the platform.

Experimental setup constraints

It is important to consider a design that is compliant with the electrochemical setup in solution. In fact, no microfluidics will be considered in the initial testing of the flexible platform. In addition, electrode nanostructuration is performed in solution. Consequently, it is important to leave a sufficient margin (around 8-10 mm) between the contacts pads and the electrodes to provide good isolation between the electrochemical platform and the circuitry.

The contacts pads must be designed according to the setup and connector type.

5.1.2 Design of the flexible platform prototype

The layouts considered in this work have been drawn using Tanner L-Edit EDA tool from Mentor Graphics.

Platinum was chosen as WE material because of its superior potentiometric properties, as shown in Chapter 3. The RE will be made of silver because it readily oxidizes with various states (Ag^+ , AgCl , AgO) with controlled relative quantities, thus maintaining a stable potential [14].

In the first design, the WEs and RE diameters are set to 4 mm (which correspond to an electrode area of 12.56 mm^2) in order to have a similar surface area with respect to the SC-ISEs fabricated on rigid substrates (see Chapters 3 and 4). In the next chapter, smaller dimensions will be tested and compared to enable further miniaturization.

The RE is placed in the middle of the design to ensure symmetry and reduce the unwanted effects discussed in Section 5.1.1.

The contacts pads have been designed according to the chosen card edge connector. A pitch

Capitolo 5. Fabrication of a flexible electrochemical platform

of 3.96 mm is used in the first design. The width of the contact pad and of the wires are 1 mm and 0.1 mm, respectively. The wire length is 17 mm.

The electrodes are placed in order to minimize signal crowding (non-uniform distribution of the signal) and crosstalk.

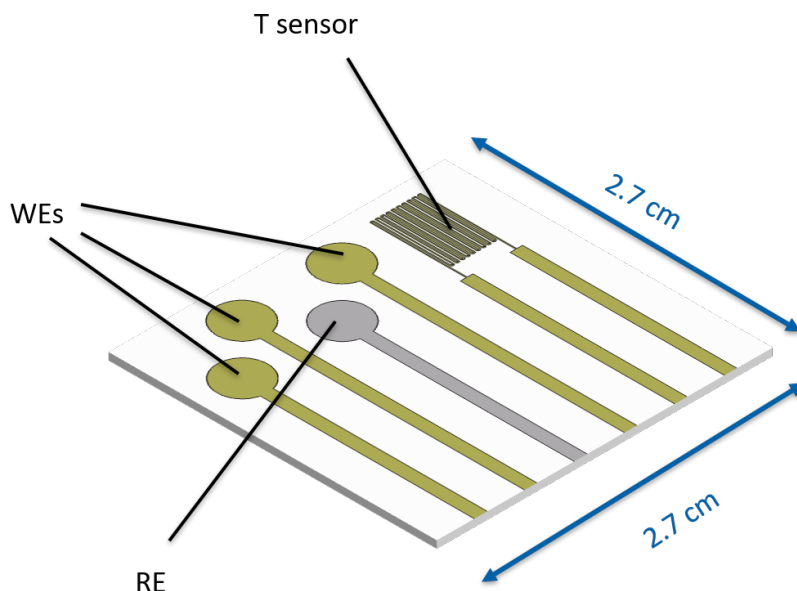


Figura 5.2 – Design of the complete wearable electrochemical multi-sensing platform fabricated in this work.

5.1.3 Process flow

After proper architecture design, the flexible electrochemical multi-sensing platform was fabricated in the CMI cleanroom facilities at EPFL. In this section, a detailed description of the process and challenges encountered is given.

Overview

The process flow for the microfabrication of the flexible electrochemical multi-sensing platform is shown in Figure 5.3. All experimental details are reported in Table 5.1. In this paragraph, a brief overview of the production steps is given, while in the next sections each stage is described in detail.

A silicon wafer is used as rigid substrate during the fabrication. A sacrificial Aluminum layer is deposited initially on a silicon test wafer in order to enable a simple anodic release of the platforms at the end of the manufacturing steps. A thin layer of *Polyimide* (PI) is then deposited to serve as flexible substrate material for the final platform. The patterning process

5.1. Microfabrication of a flexible integrated platform

involves two main lithographic steps followed by a lift-off to define the platinum and silver areas. Subsequently, after deposition of a PI passivation layer, a third lithography is performed to open the contacts and electrodes area, before the final anodic release.

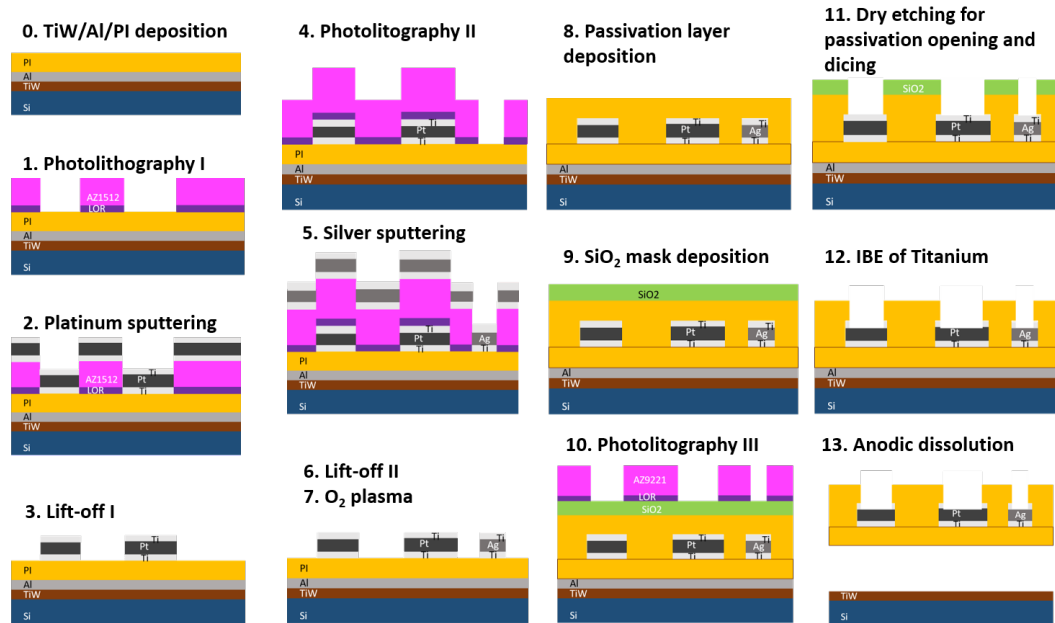


Figure 5.3 – Fabrication steps of the flexible electrochemical multi-sensing platform on a PI substrate.

Step 0: wafer and substrate preparation

A test 100/P/SS/01-100 silicon wafer is used during the fabrication. This acts only as rigid support and will be discarded at the end. A TiW/Al layer is deposited on top of it as this will be dissolved at the end of the process (step 9 of the process flow in Figure 5.3) to enable the release of the final platforms. A 10 μm PI film is then spin-coated on the surface and properly cured. This will be the substrate material of the final platform.

Step 1: photolithography I

Two lithographic steps are used to pattern the metal areas that will be defined after the lift-off process: the first lithography (step 2 of the process flow in Figure 5.3) will be used for the platinum WEs and contacts, while the second one (step 3 of the process flow in Figure 5.3) defines the silver RE.

Briefly, a light-sensitive material called *Photoresist* (PR) is spin-coated on top of the wafer. Direct laser writing is used to expose the desired region of the PR layer (eventually a mask can be fabricated for faster exposure). A solvent, called a developer, is then applied on the surface. In the case of a positive PR, the photo-sensitive material is degraded by light, causing

Capitolo 5. Fabrication of a flexible electrochemical platform

Tabella 5.1 – Detailed runcard for the fabrication of the flexible electrochemical multi-sensing platform.

Step	Process	Parameters
1. Substrate preparation		
<i>Equipment: DP 650, Sawatec LSM200, Heraeus T6060.</i>		
0.1	Wafer stock out	Test 100/P/SS/01-100 Si wafer
0.2	Wafer check	-
0.3	TiW deposition	150 nm
0.4	Al deposition	400 nm
0.5	PI spin-coating	PI 2611 10 μm
0.6	PI full-curing	295°C (1h)
1. Photolithography I		
<i>Equipment: EVG 150, MLA 150.</i>		
1.1	Wafer dehydration	160°C (180s) -22° (30s)
1.2	LOR coating	spin-coating LOR 5A (0.7 μm)
1.3	LOR bake	190°C (250s) -22° (30s)
1.4	PR coating	spin-coating AZ1512 (1.6 μm)
1.5	PR bake	100°C (90s) -22° (15s)
1.6	PR exposure	Dose: 130 mJ/cm ² . Defocus: -2°.
1.7	PR development	-
1.8	PR post-bake	100°C (60s) -22° (15s)
1.9	Inspection with OM	-
2. Platinum Sputtering		
<i>Equipment: DP 650.</i>		
2.1	O ₂ etching for substrate activation	5 s
2.2	Ti deposition	20 nm
2.3	Pt deposition	200 nm
2.4	Ti deposition	20 nm
3. Lift-off I		
<i>Equipment: Plade Solvent.</i>		
3.1	Remover 1165	more than 30h
3.2	Remover 1165 + US	5 min
3.3	IPA	90 s
3.4	Fast Fill Rinse	1 min
3.5	Trickle tank water bath	1 min
3.6	Spin rinser dryer	-
3.7	Inspection with OM	-
4. Photolithography II		
<i>Equipment: EVG 150, MLA 150.</i>		
4.1	Wafer dehydration	160°C (180s) -22° (30s)
4.2	LOR coating	spin-coating LOR 5A (0.7 μm)
4.3	LOR bake	190°C (250s) -22° (30s)
4.4	PR coating	spin-coating AZ1512 (1.6 μm)
4.5	PR bake	100°C (90s) -22° (15s)
4.6	PR exposure	Dose: 130 mJ/cm ² . Defocus: -2°.
4.7	PR development	-
4.8	PR post-bake	100°C (60s) -22° (15s)
4.9	Inspection with OM	-
5. Silver Sputtering		
<i>Equipment: DP 650.</i>		
5.1	O ₂ etching for substrate activation	5 s
5.2	Ti deposition	20 nm
5.3	Ag deposition	200 nm
5.4	Ti deposition	20 nm

5.1. Microfabrication of a flexible integrated platform

Step	Process	Parameters
6. Lift-off II		
<i>Equipment: Plade Solvent.</i>		
6.1	Remover 1165	more than 30h
6.2	Remover 1165 + US	5 min
6.3	IPA	90 s
6.4	Fast Fill Rinse	1 min
6.5	Trickle tank water bath	1 min
6.6	Spin rinser dryer	-
6.7	Inspection with OM	-
7. Oxygen plasma		
<i>Equipment: Tepla 300.</i>		
7.1	O ₂ plasma cleaning	200 W for 45 s
8. Passivation layer deposition		
<i>Equipment: VN652, Sawatec LSM200, Heraeus T6060.</i>		
8.1	Adhesion promotion for PI	VM-651 adhesion promoter
8.2	PI spin-coating	PI 2611 10 μm
8.3	PI full curing	295°C (1h)
8.4	Inspection with OM	-
9. SiO₂ mask deposition		
<i>Equipment: Pfeiffer Spider 600.</i>		
9.1	SiO ₂ deposition	300 nm
10. Photolithography III		
<i>Equipment: ACS 200, MLA 150.</i>		
10.1	HMDS priming	-
10.2	PR coating	spin-coating AZ9221 (2 μm)
10.3	PR bake	110°C (2min) -22° (15s)
10.4	PR exposure	Dose: 200 mJ/cm ² . Defocus: +1°.
10.5	PR development	-
10.6	PR reflow	100°C (10s) -22° (15s)
11. Dry etching for passivation opening and dicing		
<i>Equipment: STS Multiplex ICP</i>		
11.1	SiO ₂ etching	about 3 min
11.2	PI etching	about 17 min
11.3	Inspection with OM	-
12. IBE of titanium		
<i>Equipment: Nexus IBE350 from Veeco.</i>		
12.1	Ti etching	less than 2 min
12.2	Inspection with OM	-
13. Anodic dissolution		
<i>Equipment: portable power supplier.</i>		
13.1	Anodic dissolution	0.8 V for ≈ 24 h in 1 M NaCl
13.2	Cleaning in water and drying	
13.3	Inspection with OM	-

the dissolution of the regions that were exposed to the light. Only the unexposed regions will remain on the wafer. On the contrary, a negative PR is strengthened by light exposure, thus after development the exposed region will stay on the surface.

A properly designed bi-layer PR coating is preferred when a lift-off process is involved in order to achieve higher pattern resolution than with only one PR. In fact, a *Lift-Off Resist* (LOR) and a positive tone PR are deposited one after the other. Thanks to their different chemical properties, the LOR is preferably undercut during the process. The opening of these

undercuts in the LOR promotes the lift-off as the solvent can permeate more easily, facilitating the removal of the PR.

In our case we have used the AZ1512 HS as main positive tone PR, with a first layer of LOR 5A to facilitate the lift-off process. No vapor priming is required to enhance LOR adhesion on the silicon substrate. LOR 5A dissolves in alkaline solutions. It is recommended that its thickness is higher than the one of the deposited metal. Lithography experts usually suggest a thickness three times the one of the metal. The target metal stack is of 240 nm, thus an LOR thickness of 0.7 μm has been chosen. A 1.6 μm layer of AZ1512 was spin-coated on top (as the recommended thickness is about the double than the one of the LOR).

The lateral resolution of the lift-off depends on the PR thickness and reaches about 1 μm . The high concentration of the photoactive compound of the AZ 1512 HS maximizes the resist contrast according to the provider. The PR is then baked at 100 °C for 90 s.

Direct writing was chosen for PR exposure as this method offers more flexibility as the design of the platform is likely to be modified to adjust it to the specific needs. On the contrary, when a consolidated device is patterned, a mask is usually fabricated for batch processing.

A Heidelberg Mask Less Aligner (MLA) 150 is used for the exposure. This exploits a laser-diode emitting at 405 nm. The focusing is performed with a single writehead. The suggested dose and defocus angle for a specific PR type and thickness are tabulated by experts in CMI. Nevertheless, the conditions might be slightly adjusted according to the environmental conditions that might vary slightly. In our case a little over-exposure margin of about 30-40 % can be used to ensure proper patterning as the design does need extremely low resolution.

The exposure makes the PR soluble. Thus, a proper developer is put on the wafer surface for a controlled time to completely remove the exposed PR regions. If the development time is not sufficient some PR residues might remain in the trenches. On the contrary, unexposed areas might start to dissolve if a too long development time is used. After this process an hard-bake at 100 °C for 120 s is performed to enhance the PR stability and undercut the LOR.

Step 2: platinum sputtering

Several deposition techniques are available at CMI. These include evaporation, sputtering and electroplating. The first two are Physical Vapour Deposition (PVD) methods as the metal is grown by accumulation of gaseous material on a substrate. On the contrary, electroplating is an electrochemical process.

- **Thermal evaporation** is the controlled deposition of atoms on a substrate based on dislodgment from a source by means of target heating. This can be done by a high current flow (Joule effect) or by electron bombardment. In all cases, a very low pressure ($\sim 10 \times 10^{-6}$ mbar) is used. Consequently, high directionality and purity is achieved during the deposition [137, 138].

- **Sputtering** in general involves the formation of a plasma by a power supply. A plasma is a partially ionized, but neutral gas, with a large number of free carriers (ions and electrons). Because of their large density, they undergo electromagnetic interactions, that strongly affect the physical properties of the medium, which behaves like a fluid. As a consequence of the large amount of carriers, the plasma is highly conductive, typically with anisotropic behavior. The target is made of the material to be deposited and acts as the cathode since it is connected to the negative terminal of the *Direct Current* (DC) or *Radio Frequency* (RF) power supply. The RF method was invented to overcome the impossibility to deposit insulating material with the DC sputtering, that would need too high voltages to work and generate charge accumulation at the target surface. Sputtering ensures in general good adhesion and uniformity. However, the background pressure is much larger than in the case thermal evaporation ($\sim 10^{-2}$ mbar). Therefore, it is prone to more particle contamination and sidewall deposition due to the lower directionality [137, 138].
- **Electroplating** is based on a two-electrodes setup placed in solution. An electrical current is applied to induce the reduction of metal cations, that will form a thin film at the cathode. This is a low-cost technique as no vacuum or high temperatures are required. In addition, it provides high deposition rates and uniformity. However, only Cu and Ni can be electroplated at CMI and the PI substrate is not compatible with this method [137, 138].

In general, evaporation is preferred when a lift-off process is involved, as it avoids burning of the PR by the plasma. Indeed, this method is more directional with respect to sputtering because of the higher vacuum involved in the process, which ensure high conformability, directionality and little sidewall deposition. However, in our case the Ti/metal/Ti stack on the PI substrate has a poor adhesion on the substrate. Thus, an activation step to roughen the PI surface is needed. This is done before the sputtering deposition by a short oxygen plasma step directly in the chamber that will improve the adherence of the metal atoms on the PI. Therefore, in our case sputtering was used to ensure efficient metal deposition and anchoring to the substrate [137, 138].

A DP 650 sputtering tool was used in this work to deposit the metal layers. The procedure includes a 5 s activation step with oxygen plasma to enhance adhesion. A thin titanium layer is placed on top of the electrodes to protect the surface from oxidation during processing (this is especially important for the next lithography as silver is easily oxidized). A final etching step to remove this thin protection layer of titanium will then be added at the end of the process.

Step 3: lift-off I

After the metal sputtering, the full wafer is covered with metal, as illustrated in step 2 of Figure 5.3. The sample is placed in the Remover 1165 over weekend in order to completely dissolve the patterned resist, leaving behind the wanted design.

Capitolo 5. Fabrication of a flexible electrochemical platform

The LOR undercuts will promote the filtration of the solvent, facilitating the PR removal. Eventually, a ultra sonic bath can also be shortly used to further promote the process and to clean final residues. After lift-off completion, the substrate is cleaned by dipping the wafer in *Isopropanol* (IPA) for 90 s, followed by short dipping in two baths of deionized water. The sample is then dried with a Spin Rinser Dryer tool, before inspection at the Optical Microscope (OM).

Step 4-6: photolithography II, silver sputtering and lift-off II

The same procedure described in the previous paragraphs for the steps 2-4 are repeated for the deposition and patterning of the silver metal. A thin titanium layer is placed on top of the electrodes to protect the silver surface from oxidation during processing. A final etching step to remove this thin protection layer of titanium will then be added at the end of the process.

Step 7: O₂ plasma cleaning

A brief plasma oxygen cleaning at 200 W for 45 s is performed to remove possible lift-off residues that might cause lack of adhesion or contact.

Step 8 and 9: deposition of the passivation layer and of the etching mask

A surface pre-treatment with the VM651 from DuPont is performed to improve PI adhesion. Then, a 10 μm PI film is spin-coated on the surface and properly cured. This acts as a passivation layer.

A thin SiO₂ layer is deposited on top of the PI as this will be the mask in the subsequent etching steps for passivation opening.

Step 10: photolithography III

The PI passivation layer must be opened in the correspondence of the contacts and of the electrodes areas. This is done by dry etching using a SiO₂ mask. In order to do so, the SiO₂ must be etched according to the desired final design. This can be done by dry etching using a PR mask. For this reason, a PR is patterned on top of the stack at this stage.

In the first trials, an AZ1512 HS was used for this purpose. However, after development the thin oxide layers cracked due to the thermal stresses during the development process. For this reason, AZ9221 was chosen in the following batches to avoid oxide damaging as for this PR material a short reflow (10 s at about 100°C) is sufficient after development.

Step 11: passivation opening via dry etching

The patterning of the SiO₂ is done by dry etching with CF₄ chemistry at room temperature. Dry etching consists in removing material by exposing the sample to bombardment of ions, typically a plasma of reactive gases. A mask is used to give the desired pattern. In the case of SiO₂ etching, the PR mask deposited in step 10 is used. The etching rate is about 0.25 μm/min and the selectivity is 1:1. Thus, three minutes are more than enough to ensure proper opening of the mask.

Once the SiO₂ mask is patterned, the passivation can be opened by using a different dry etching procedure. This is based on O₂ chemistry at room temperature. The etching rate is larger than 1 μm/min, with a selectivity PI:SiO₂ larger than 50:1.

The etching of the PI passivation stops once the metal is reached. For this reason, the procedure can be used also for dicing of the platform: once the PI on top of the contacts and of the electrodes area is completely consumed the etching stops in those area; however, the process can be continued further to etch the metal-free areas in order to define trenches around the platforms for dicing; the etching will be completely finished once the aluminum is reached in the correspondence of the platforms border lines.

A period of about 17 minutes was found to be sufficient for complete etching until Aluminum.

Step 12: Ti etching

A thin titanium layer was put on top of the metal electrodes to protect the silver from oxidation. In order to remove this thin film and expose the desired metals, i.e. platinum and silver, another etching procedure must be performed.

A simple wet etching step was initially used for this purpose as in principle titanium is easily dissolved in HF. However, this method was found to be inefficient and not reproducible. For this reason, *Ion Beam Etching* was consequently used with better results.

The IBE procedure is based on milling with Argon ions. An RF generator is used to produce a plasma. A 3-grid optics system produces a single and uniform beam. A mechanical shutter separates the beam from the sample chamber. A Plasma Bridge Neutralizer is placed downstream to impinge electrons on the substrate and balance the accumulation of positive charges.

The substrate is typically loaded with a fixture angle of -5° or -10°. The sample is rotated to enhance uniformity. The energy can be properly tuned depending on the specific needs. High energy processes are evidently faster, but causes larger damage and give less control on the etched thickness. A medium energy process is used in this case.

The etching time is in general controlled with a Secondary Ion Mass Spectroscopy (SIMS). This system will record in real-time the secondary ions ejected from the sample surface during

etching. A mass analyzer enables the determination of the collected elements, thus providing information about the material currently being removed. In our case, plots of titanium, platinum and silver are acquired. When the platinum and silver signals start to increase, the etching of titanium can be considered completed and the process can be stopped. In our case, the procedure takes less than 2 minutes.

Step 13: anodic release

In the last step the electrochemical platform created on the PI substrate must be released from the support wafer. This is done by anodic dissolution of the initially deposited Aluminum layer. A two-electrodes electrochemical setup is used in a 1 M NaCl solution while stirring. The sample is connected to the positive pole, a platinum wafer to the negative one. A potential in the range of 0.8-0.9 V is applied.

The rate of dissolution strongly depends on the ability of the NaCl solution to access the Aluminum. For this reason, large separation lines between the platforms have been added in later designs. Indeed, once opened in step 11, they ensure easier permeation of the solution on the aluminum surface. The whole process takes about 24 h in optimal conditions.

5.1.4 Summary

In this section, the design constraints of a flexible electrochemical multi-sensing platform and their solutions are discussed. A complete overview of the developed cleanroom process and of the encountered challenges is given.

5.2 Characterization of the flexible WEs

In the previous section we have described the successful fabrication of a flexible multi-sensing electrochemical platform on a PI substrate. In this paragraph, its morphological and electrochemical characterization is reported to confirm proper functionality. External REs are used at this stage of the investigation.

5.2.1 Electrochemical tests

Different cleaning procedures were performed before using the platforms. Simple dipping in various solvents was found not to be sufficient to achieve a good electrochemical signal. The best method to obtain consistent results and good response was the electrochemical cleaning in 0.5 M H₂SO₄ by CV. The cycles were repeated until perfect overlapping of subsequent curves.

In Figure 5.4 the cyclic voltammograms of the cleaned flexible platinum electrodes in 5 mM potassium ferro/ferricyanide solution is reported. It is possible to conclude that the

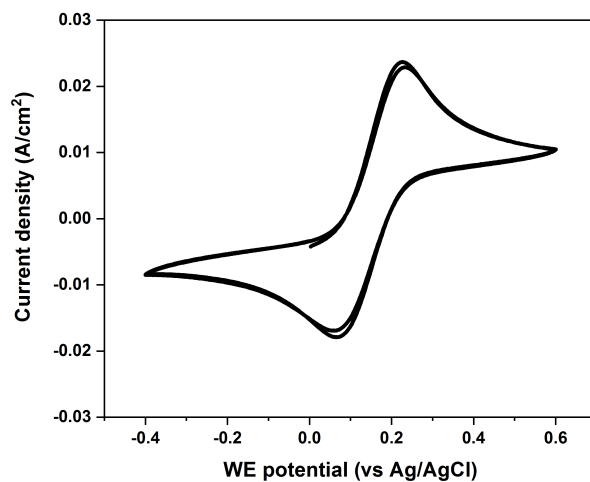


Figura 5.4 – Cyclic voltammograms of the flexible platinum electrodes in a 5 mM potassium ferro/ferricyanide solution.

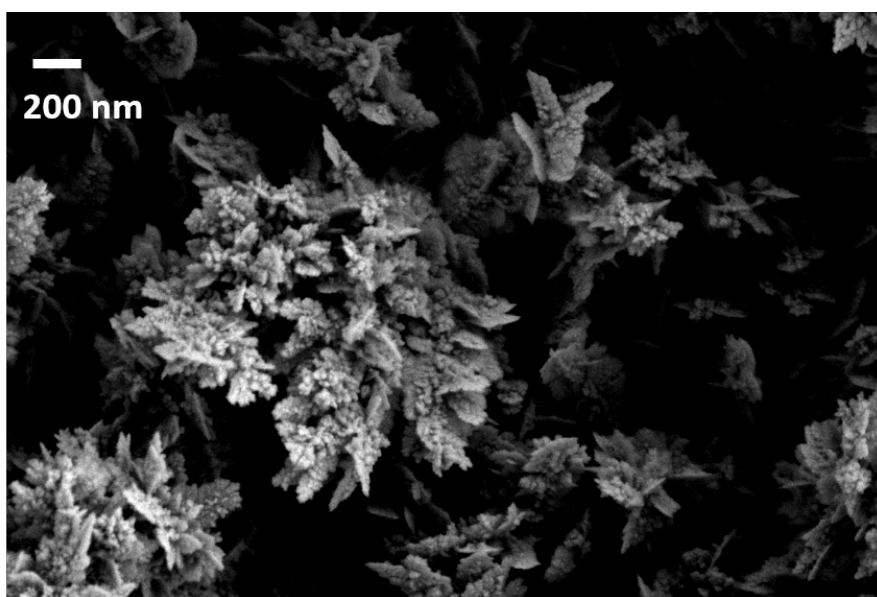


Figura 5.5 – SEM image of the platinum nanoflowers deposited on the flexible sensing electrodes.

electrochemical response after the electrochemical cleaning in H_2SO_4 is highly stable and reproducible.

The flexible platforms were also tested for the deposition of the platinum nanostructures developed in this work and discussed in the previous chapters. The same protocol was transferred on the custom-made sensors (we refer the reader to Chapter 3 for a detailed description of the fabrication procedure of this nanostructures). As for the voltammetric response, the cleaning procedure has a strong effect also on the potentiometric deposition of

the nanoflowers. In particular, the previously discussed electrochemical cleaning in H_2SO_4 is crucial to achieve a conformal and uniform platinum nanostructured layers on top of the WEs. If a proper cleaning procedure is performed prior to the deposition, the fabrication steps described in Chapter 3 were found to give similar results to the ones obtained on rigid substrates. This achievement is confirmed by SEM analysis (Fig. 3.12) and by the similar roughness factors (~ 200).

5.2.2 Bending tests

As these platforms are meant to be used in wearable systems, the effect of bending and unbending on the mechanical stability and electrochemical performance of the device must also be analyzed. In Figure 5.6 the electrochemical response of a flexible Li^+ ISEs during mechanical stress of the platform is given. It is possible to observe that the electrochemical response is practically stable during bending and unbending of 180° . In addition, no delamination phenomena were observed.

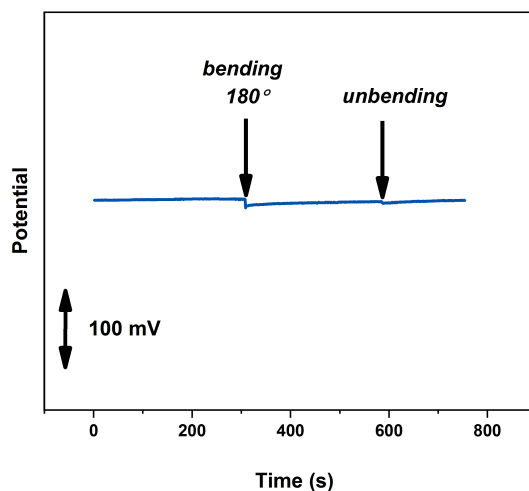


Figura 5.6 – Effect of bending on the potential response of the flexible Li^+ ISEs.

5.2.3 Summary

In this section the custom-made flexible platforms are tested. The cleaning procedure is found to have a crucial role to ensure reproducibility of the electrochemical signal and of the deposition of platinum nanoflowers. No significant influence of bending/unbending was recorded during potentiometric measurements.

5.3 Flexible all-solid-state REs

A stable RE is a crucial element in an electrochemical cell. This is especially true in potentiometric electrochemical sensors where accurate potential readings are fundamental. In this section, we describe the fabrication and testing of all-solid-state reference membranes on rigid electrodes. The same technology is then transferred on the custom-made flexible platform. [139, 140].

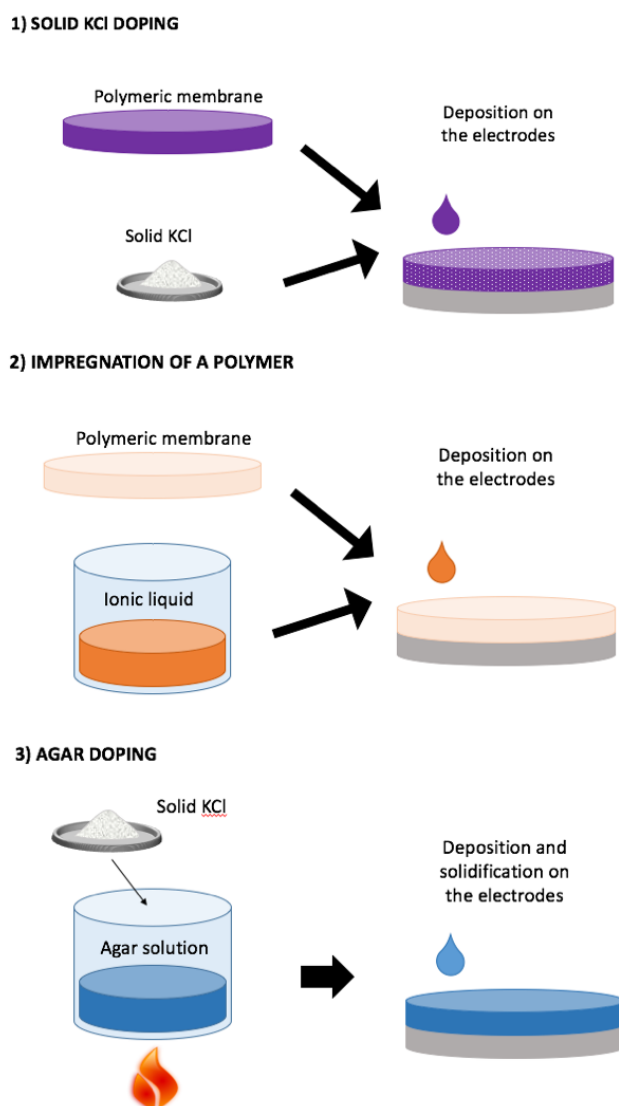


Figura 5.7 – Different strategies for the fabrication of reference membranes. Reprinted with permission from [16]. ©[2019]IEEE

5.3.1 Motivation

As discussed in the previous chapters, all-solid-state potentiometric ion-sensors have been extensively used for environmental monitoring and for measuring the concentration of electrolytes in different body fluids for personalized healthcare. However, the realization of adequate and stable REs still represents one of the most challenging issues that prevents their commercialization. Although various strategies have been proposed in literature, this problem is still far from a final solution.

The Ag/AgCl double junction RE is the most commonly used type of RE thanks to its excellent stability, simplicity and non-toxicity [139]. Due to its popularity, it is the most targeted RE for miniaturized systems. However, conventional liquid-filled REs are not suitable for the portable applications because of the difficult trapping of the solution in miniaturized electrodes and of the high sensitivity to temperature and pressure variations. In recent years, several attempts to build all-solid-state REs have been proposed in literature [35, 141]. In these systems a solid-state exchange membrane doped with KCl (or NaCl/AgCl) is used to replace the liquid junction of conventional REs. Different strategies have been proposed (Fig. 5.7), which include the impregnation of a polymer with Ionic Liquids (ILs) [90, 142], solid doping of agar [143, 144] or of a polymeric membrane [145, 146]. However, many challenges still need to be overcome, including the continuous leaching of the loaded ions and the influence of the sample solution on the interfacial potential [16].

In this section, we produce different REs membranes to characterize and compare their electrochemical behaviour in different conditions: Agar, *Polyvinyl Butyral* (PVB), PVC, Ionic-Liquid(IL)-doped PVC. The initial tests and comparisons of the membranes on rigid substrates are reported in Section 5.3.3. The best solutions are used to calibrate lithium ISEs. The influence of chloride concentration and of pH on their stability is investigated to help defining the best membrane for different applications. The transfer of the best technology on the flexible platform is then discussed in 5.3.4.

5.3.2 Experimental methods

The experimental details of the fabrication and characterization of different all-solid-state REs are reported below.

Materials

All chemicals were obtained from Sigma Aldrich. silver, platinum and gold rigid screen-printed electrodes with a diameter of 4 mm were obtained from DropSens (Spain). The custom-made flexible electrochemical platforms were fabricated as discussed in Section 5.1.

Electrode fabrication

The chemical chlorination was performed in a 50 mM FeCl₃ solution for 3 minutes.

The agar membrane was produced with 0.8 g of agar in 50 ml of 1 M KCl. After reaching the boiling temperature, the solution was cooled to 65 °C and then spread over the electrode. In all other cases 10 µl of membrane solution was drop-cast on the electrodes. The membrane cocktail compositions are the following: 79.1 mg of PVB and 50 mg of NaCl in ethanol for PVB; 0.4 g of PVC in NaCl saturated THF for PVC; 0.1 % of IL, 33 % of PVC powder, 66 % of Bis(2-ethylhexyl) sebacate in 0.5 mL of THF for the PVC membrane doped with the IL. 5 replicas were produced per sample type.

Li⁺ ISEs with nanostructured SCs were fabricated as described in Section 3. The calibrations were performed by subsequent LiCl additions.

Morphological and electrochemical characterization

A two-electrodes setup was used in all potentiometric measurements using a Double Junction (DJ) Ag/AgCl RE external to the platform and provided from Metrohm. This DJ is filled with 3M KCl and lithium acetate as internal and external solutions, respectively. CV was performed in a three-electrodes setup. SEM images were obtained with a Merlin microscope from Zeiss in SE mode using an *In Lens* detector.

5.3.3 Testing of different all-solid-state REs on rigid substrates

Different ion-exchange reference membranes are proposed and compared in this work to improve the performance of simple solid-state Ag/AgCl REs: solid-doped agar, solid-doped PVB, solid-doped PVC and IL-doped PVC. The fabricated REs are tested for the calibration of Li⁺ ISEs based on nanostructured SCs. A typical calibration example is given in Figure 5.8 for a IL-PVC RE. All calibrations are performed by subsequent LiCl additions. All sensors parameters obtained using different all-solid-state REs are given in Table 5.2 in comparison with a conventional DJ Ag/AgCl RE and with a chlorinated planar Ag/AgCl RE without exchange membrane.

It is worth to notice that PVB, PVC and IL-PVC REs exhibit quasi-Nernstian response. In particular, IL-PVC shows the closest behaviour to the DJ RE, with the smallest standard deviation. On the contrary, the slope obtained with the Ag/AgCl RE without membrane is almost double of the slope of the DJ RE. This can be explained considering that the bare Ag/AgCl RE is highly sensitive to the concentration of chloride ions in solution. Chlorides ions seem to have high permeability also in the agar membrane as the slopes obtained with this RE is double of the Nernstian value and its standard deviation is significantly large.

In order to confirm these hypotheses and better understand the behaviour of the different

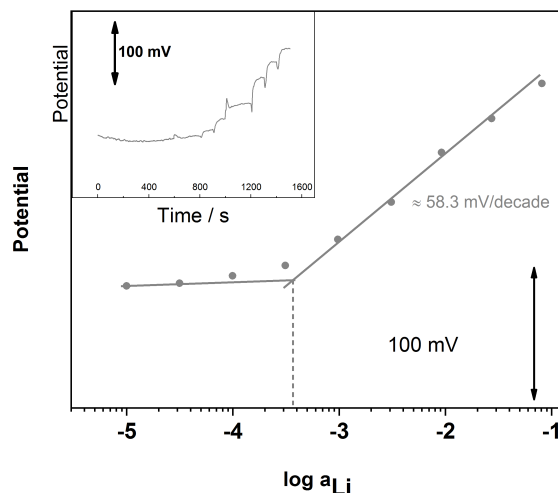


Figura 5.8 – Example of a calibration of a Li^+ ISE with a all-solid-state RE based on a IL-PVC membrane. The corresponding calibration time trace is given in the small inset. Adapted with permission from [16]. ©[2019]IEEE

Tabella 5.2 – Comparison of sensitivity and LOD values of a Li^+ SC-ISE when the calibration procedure is performed using different all-solid-state REs. The RE membranes were deposited on previously chlorinated silver REs [16].

	Sensitivity [mV/decade]	LOD
No membrane	108.8 ± 31.6	$(4.0 \pm 3.7) \times 10^{-4}$
PVB	63.9 ± 13.0	$(2.3 \pm 1.6) \times 10^{-4}$
Agar	112.9 ± 24.8	$(4.1 \pm 3.5) \times 10^{-4}$
PVC	54.5 ± 9.5	$(1.1 \pm 0.6) \times 10^{-4}$
IL-PVC	57.7 ± 0.9	$(1.1 \pm 0.3) \times 10^{-4}$
DJ	58.7 ± 0.8	$(0.7 \pm 0.3) \times 10^{-4}$

membranes, the variations of RE potential with increasing chloride concentration are also investigated. All results are given in Figure 5.9 for three replicas of each RE type. As expected, the potential of the planar RE without membranes greatly decreases with the addition of chlorides to the sample solution. This behaviour explains the high slope obtained during the calibration of the Li^+ ISEs.

The IL-PVC and PVB membranes have a limited drift until high concentrations are reached (10^{-2} - 10^{-1} M). The PVC membranes shows the most stable potential at low concentration. Only at high concentration they start to exhibit a sensitivity to chloride ions. The lowest permeability of the PVC membranes is probably due to the more compact structure with respect to the other all-solid-state REs (Fig. 5.10). On the contrary, the different agar samples show significant drifts in both directions with limited reproducibility. This behaviour can be justified by considering the low elastic modulus of this material, that makes it very permeable

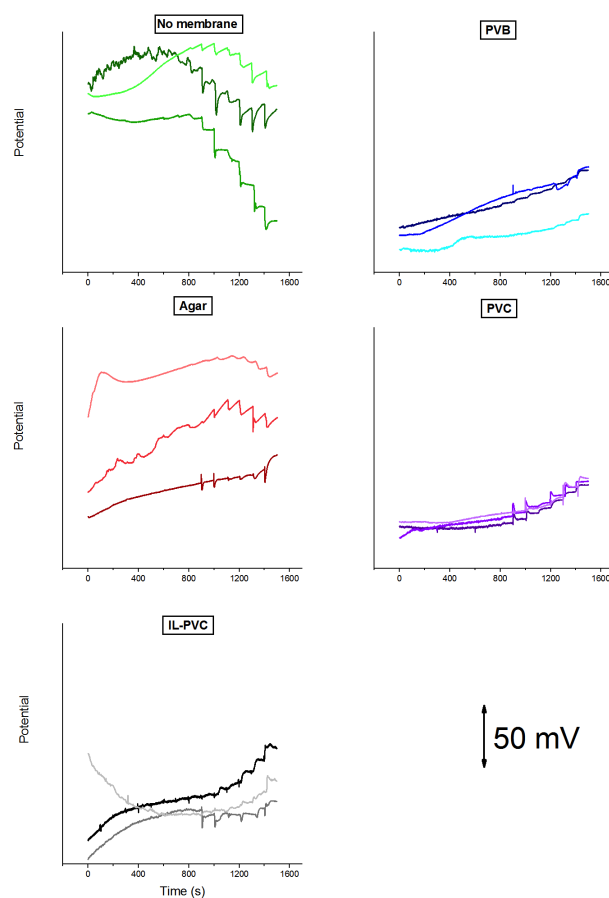


Figure 5.9 – Dependence of RE potential at increasing chloride concentrations from 10^{-9} up to 10^{-1} M by subsequent chloride additions every 100s (activity steps of a decade up to 10^{-6} M, half a decade up to 10^{-1} M). The responses of three different samples are reported per each RE type. Reprinted with permission from [16]. ©[2019]IEEE

and prone to detachments as evident in Figure 5.10.

The influence of pH on the RE potential is also analyzed. It is possible to observe from Figure 5.11 that in all cases the presence of a RE membrane drastically improves the stability at different pH and the reproducibility among different replicas. As for the previous tests, the agar membranes show the poorest behaviour. PVB, IL-PVC and PVC reference membranes drastically enhance the RE stability and reproducibility at different pH.

The RE electrodes were finally tested for voltammetric applications. The cyclic voltammograms of a gold screen-printed electrode in a 5 mM potassium ferro/ferricyanide solution are given in Figure 5.12 versus the different REs. All curves show similar peak-to-peak distance to the DJ RE. The only exception is represented by the agar membranes which have a slightly higher values, corroborating the previous discussion on its poorer behaviour. The PVC and PVB membranes confirm their good performance, with an almost identical response to the

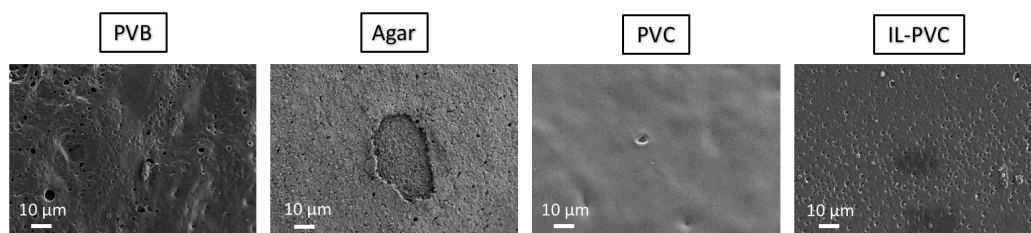


Figure 5.10 – SEM images of the different reference membranes. Reprinted with permission from [16]. ©[2019]IEEE

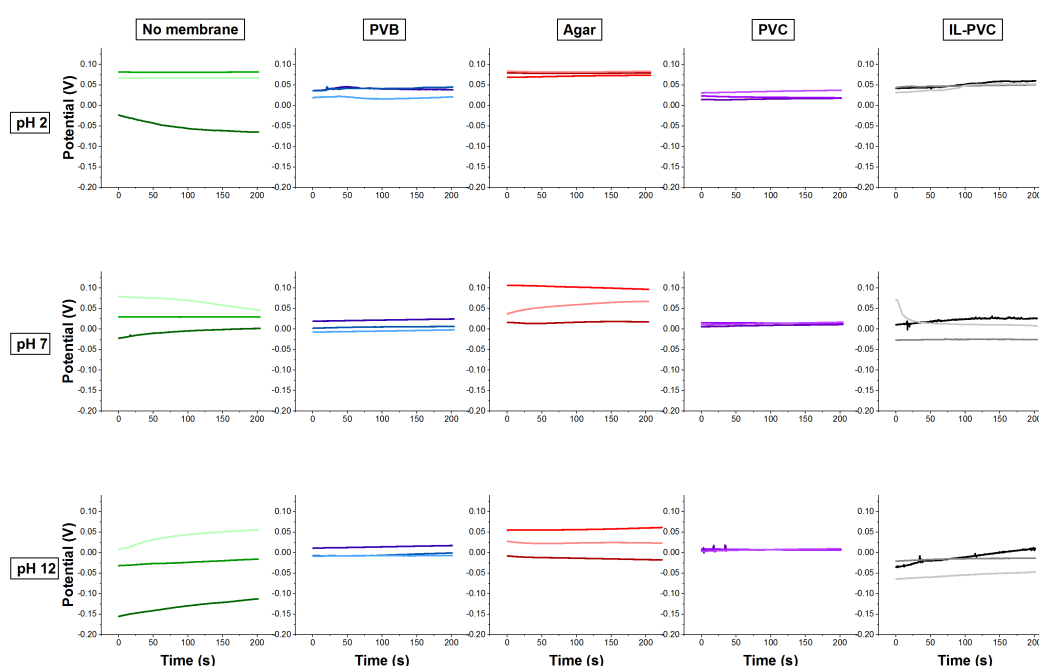


Figure 5.11 – Reference membranes potential at different pH. The responses of three different samples are reported per each RE type. Reprinted with permission from [16]. ©[2019]IEEE

Ag/AgCl DJ RE. The IL-PVC membranes have similar behaviour, but with a small shift (0.1 V) towards more negative potentials.

In conclusion, the characterization and comparison of different REs membranes on rigid silver electrodes has been reported: agar, PVB, PVC, IL-doped PVC. While agar offers only some minor improvements with respect to the bare Ag/AgCl RE, all other membranes contribute significantly to the enhancement of the stability of all-solid-state Ag REs. The PVC RE shows the highest stability towards chlorides and pH variations, followed by IL-PVC and PVB. These differences can be explained by considering the different permeability of the membranes, as

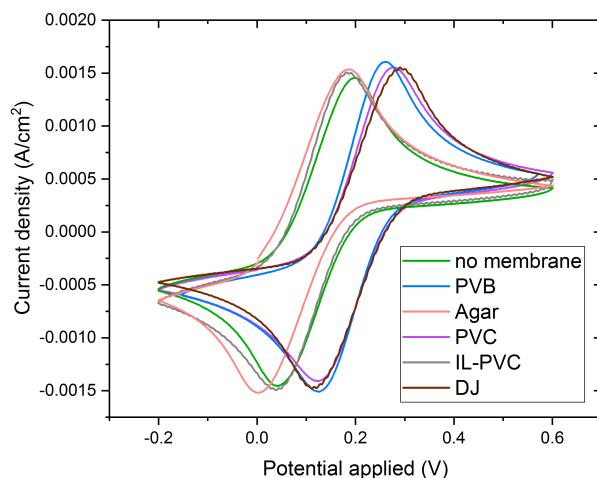


Figure 5.12 – Cyclic voltammograms of a gold screen-printed electrode in a 5 mM potassium ferro/ferricyanide solution versus the different REs. Reprinted with permission from [16]. ©[2019]IEEE

evident from the SEM analysis.

The membranes are then used to calibrate the nanostructured lithium ISEs. The PVB, PVC and IL-PVC membranes show quasi-Nernstian behaviour. In particular, IL-PVC has a very similar value to the conventional DJ RE, with a small measurement error.

The PVC and PVB membranes confirm their good behaviour also for voltammetric applications, with almost identical responses to the DJ one. The IL-PVC also maintains the same peak-to-peak distance with a small shift of the all curve to more negative potentials (0.1 V).

It is possible to conclude that the PVC and IL-PVC membranes offer good stability and reproducibility with subtle differences depending on the application and on the pH of the working solution. Thus they will be preferred for the fabrication of the flexible REs.

5.3.4 Fabrication and testing of flexible all-solid-state REs

As explained in the previous section, a stable RE is crucial to ensure accurate measurements, especially in potentiometric sensors where the precision on potential has to be optimal. A chemical chlorination is used as the electrochemical one is found to give similar results, while requiring a more laborious procedure. The produced Ag/AgCl RE is then covered with the two best membranes described in the previous section, that are PVC and an IL-doped PVC, to improve potential stability. The calibration time traces of the RE (obtained during half-log increases of the concentration) are compared to the ones obtained with a conventional Ag/AgCl double junction RE (Fig. 5.13) to prove their efficiency. The flexible IL-PVC exhibits very limited drift at low concentrations and almost identical steps height in the range of

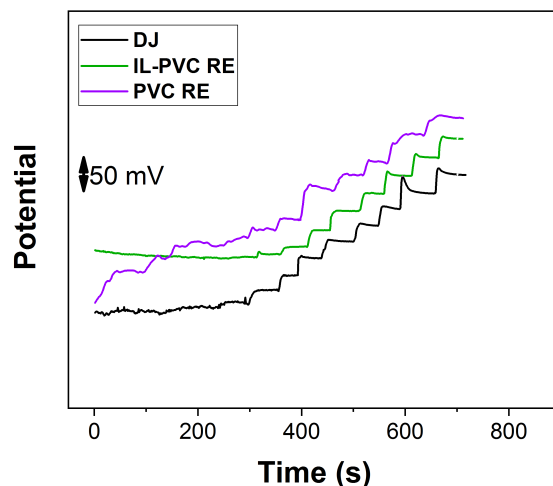


Figura 5.13 – Calibration time traces obtained with flexible REs in comparison with a double junction Ag/AgCl electrode. Adapted with permission from [13].

interest. On the contrary, the PVC RE has relatively smooth and sharp increases, but the response at low concentration shows significant drift and noise. For these reasons, the IL-PVC membrane will be preferred in the final system.

The stability of the IL-PVC RE over time was also proved, as evident from Figure 5.14. The experiment was performed in a 10 mM LiCl solution.

5.3.5 Summary

In this section, we have compared and tested the behaviour of different reference membranes. The tests on rigid electrodes showed that the best solutions seem to be the PVC and IL-PVC membranes. However, the IL-PVC RE offers a more stable response when transferred on the flexible substrate, with small drift at low concentration and sharp steps after each analyte addition. The stability of its potential value over time is also proven.

5.4 Use of the complete flexible electrochemical system for lithium detection

In Section 5.2, we prove the good functioning of the custom-made flexible platform for the deposition of platinum nanoflowers. The voltammetric signal is found to be smooth and stable. In addition, the bending/unbending of the platform does not have a significant impact on the potentiometric response. Furthermore, in Section 5.3 the fabrication of an efficient miniaturized RE on flexible substrates is described. In this section, this complete flexible electrochemical platform is used for lithium sensing.

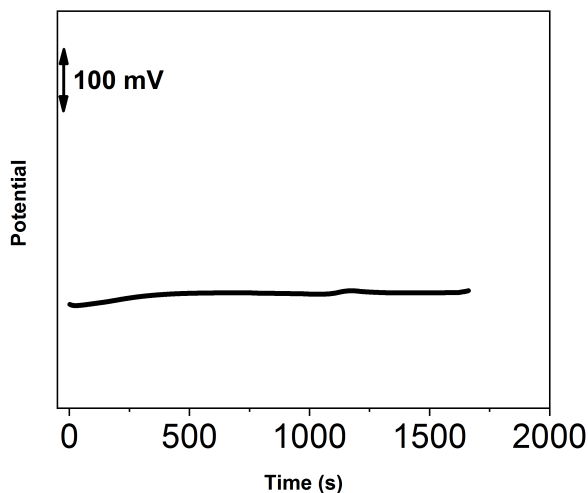


Figure 5.14 – Time stability of an all-solid-state RE based on a IL-PVC membrane. (LiCl 10 mM)
©[2019]IEEE

5.4.1 Experimental methods

The experimental details of the fabrication and characterization of the complete flexible electrochemical Li^+ -sensing system are reported below.

Materials

All chemicals were obtained from Sigma Aldrich. The custom-made flexible electrochemical platforms were fabricated as discussed in Section 5.1.

Electrode fabrication

Li^+ ISEs with nanostructured SCs were fabricated as described in Section 3 for rigid substrates. The calibrations were performed by subsequent LiCl additions. The RE electrodes were fabricated as described in the Section 5.3.

Electrochemical characterization

A two-electrodes setup was used in all potentiometric measurements using the flexible Li^+ -ISE and the built-in flexible RE.

5.4.2 Experimental results and discussion

The complete system is tested both in aqueous solution and in sweat (Fig. 5.15). The corresponding sensor parameters are reported in Table 5.3 in comparison with the literature values for rigid systems. In both cases, a quasi-Nernstian response (56.8 ± 3.9 mV/decade) is achieved in the concentration range of clinical interest. Both sensitivities and LOD values are comparable to the one reported in literature for rigid sensors. Further improvements could be obtained by proper tuning of the conditioning procedure. In this regard, a first optimization of the conditioning procedure will be discussed for this reason in the next chapter.

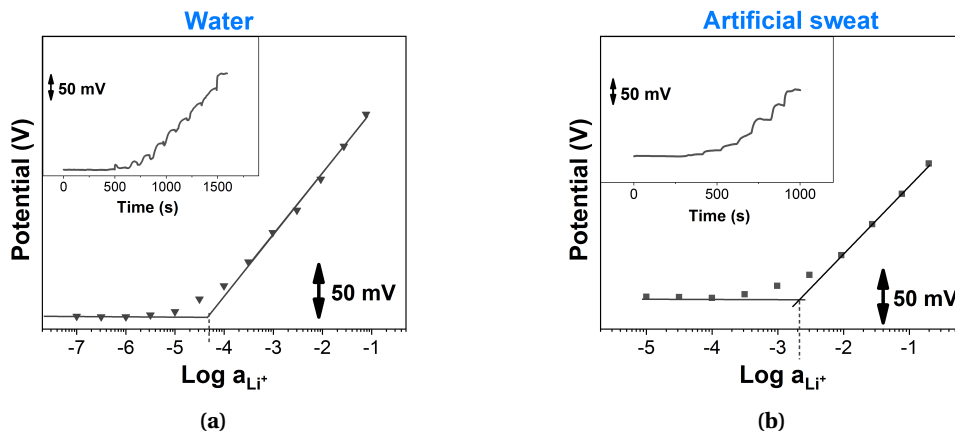


Figure 5.15 – Li^+ calibrations obtained with the flexible electrochemical sensing platform in water (a) and in artificial sweat (b) by subsequent LiCl additions. The flexible all-solid-state RE is used in all measurements. Reprinted with permission from [13]. ©[2019]IEEE

Tabella 5.3 – Analytical parameters of the flexible Li^+ -sensing system in water and in sweat [13]

	Sensitivity [mV/decade]	LOD
This work on flexible substrates (water solution)	59.6 ± 1.5	$(5.9 \pm 2.6) \times 10^{-5}$
Literature on rigid substrates (water solution) [10]	58.7 ± 0.8	$(1.3 \pm 0.4) \times 10^{-5}$
This work on flexible substrates (artificial sweat)	56.8 ± 3.9	$(1.7 \pm 0.6) \times 10^{-3}$
Literature on rigid substrates (artificial sweat) [14]	57.6 ± 2.1	$(1.4 \pm 0.2) \times 10^{-3}$

5.4.3 Summary

A complete flexible electrochemical sensing platform for non-invasive monitoring of lithium levels is fabricated and tested. The integrated all-solid-state RE discussed in the previous section of this chapter is used for all measurements. The system is tested for lithium calibration both in water and in sweat. A quasi-Nernstian response (56.8 ± 3.9 mV/decade) is obtained in both cases in the range of clinical interest ($\text{LOD} = (1.7 \pm 0.6) \times 10^{-3}$).

5.5 Integrated temperature sensor

Body temperature is a key parameter to monitor the health of a person. For this reason a temperature sensor is also integrated in the flexible platform. In this section its design and characterization is described.

5.5.1 Experimental methods

The resistivity of the Pt resistor is measured using a 4-point measurement setup (Fig. 5.16). The probes are arranged in couples on the two distal pads. The temperature is controlled using a Temptronics Model TP03215B ThermoChuck system in the range 33 °C/44 °C. The probing current has a maximum value of 500 μ A, so to be able to perform an accurate extraction of the resistivity without altering the resistor temperature by Joule effect. For each temperature set-point, the resistivity is calculated using the following equation:

$$\rho = \frac{\pi}{\ln 2} \frac{V_{23}}{I_p} t \quad (5.1)$$

where t is the film thickness, V_{23} is the voltage difference between terminals 2 and 3, and I_p is the probing current flowing from terminal 1 to terminal 4.

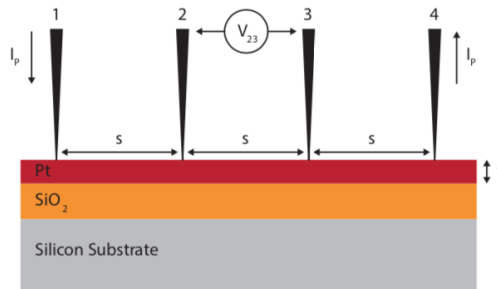


Figura 5.16 – Experimental setup for the resistive measurements on the temperature sensor.

5.5.2 Design and testing

An integrated temperature sensor is designed on the flexible platform to monitor the body temperature. It consists of a resistive coil made of platinum. This is called a Resistive Thermal Device (RTD). RTDs offer great sensing performance and simple fabrication. They are recommended applications in which high temperatures are not reached [147].

A linear response must be found to ensure high precision. Measurements accuracy is lowered when the RTD resistance is large. The lead impedance of the resistance measuring device measuring the resistance value will hide the real resistance value of the RTD. For this reason, it is important to choose properly the metal to maximize the RTD resistance. In Table 5.4 the

resistivity values of several metals are reported. It is possible to see that platinum has a quite high resistivity with respect to the other conductors. In addition, it is biocompatible, very stable and resistant to oxidation. Furthermore, it offers liner response. For these reasons, it is the most common material of choice together with Nickel alloys [147].

Tabella 5.4 – Electrical resistivity of some metals at 20 °C.

Metal	Resistivity [nΩ·m]
Silver	15.9
Copper	16.8
Gold	22.1
Tungsten	52.8
Nickel	69.3
Platinum	105
Titanium	420

The sensor is designed as a serpentine with a wire width of 130 μm and 20 foldings. We can thus predict the theoretical resistance of the system at a temperature T by applying the definition of resistance R:

$$R = \rho_{Pt} \times \frac{l}{w \times t} \quad (5.2)$$

where ρ_{Pt} is the restistance of platinum at temperature T, w the width of the serpentine and t its thickness. The variation of material resistivity with temperature can be computed using the following equation:

$$\Delta\rho = \rho_0 \times \alpha \times \Delta T \quad (5.3)$$

where ρ_0 is the original resistivity value, α is the temperature coefficient of the material (0.00392 K⁻¹ for Pt) and ΔT is the change of temperature. Using Equations 5.2 and 5.3 with the value in Table 5.4, it is possible to compute a total theoretical resistance of the serpentine of about 1.2 kΩ at 37 °C [148].

The sensors were calibrated at increasing temperature steps of 0.5 °C. The resistive measurements are performed in a 4 probes setup, as explained in Section 5.5.1. Four measurements were performed for each point. The actual temperature of the plate is measured with a temperature probe for hot plates. Figures 5.17 and 5.18 show the calibration curves obtained by using the extreme and the average values of the resistance from the measured device characteristic. In both cases a perfect linear response is obtained in the range of interest. In addition, it is possible to see that the resistance values are similar to theoretical one calculated with Equation 5.2. However, it is possible to observe that the average values offer a more precise result as the linear fitting falls always within the error bars.

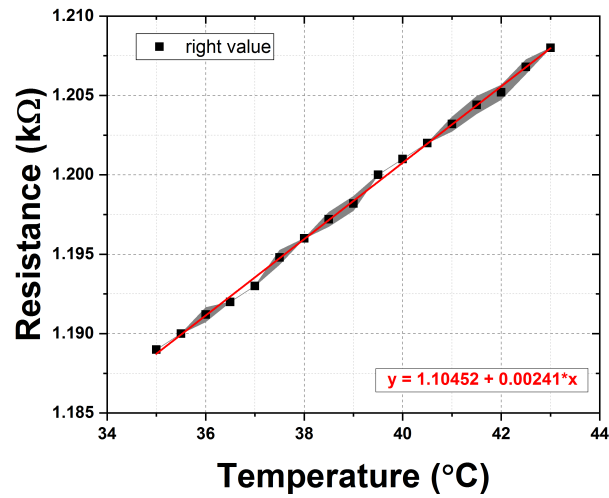


Figura 5.17 – Calibration curve obtained using the extreme values of the current-voltage characteristics of the resistors.

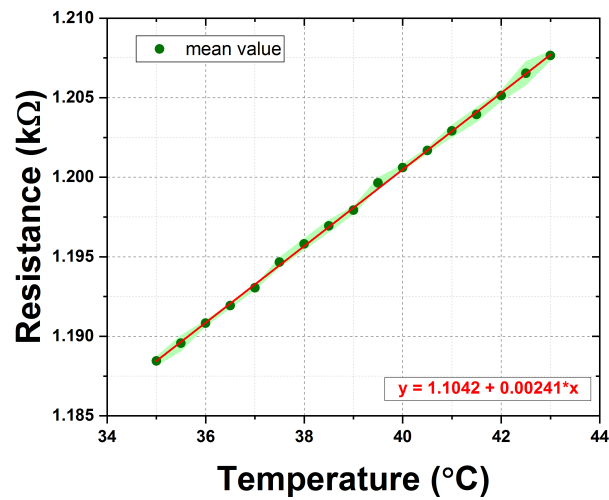


Figura 5.18 – Calibration curve obtained using the mean values of the current-voltage characteristics of the resistors.

5.5.3 Summary

In this section the design and characterization of the temperature sensor on the custom-made flexible electrochemical platforms is reported. The platinum serpentine shows perfect linear behaviour, with values close to the theoretical ones. The average resistance is calculated from the characteristic of the temperature sensor to achieve more accurate results.

5.6 Main contributions and conclusions

The increasing interests towards wearable monitoring devices requires the development of flexible sensing platform that can be easily placed on the skin. In this chapter we have described the design and realization of a complete flexible electrochemical multi-sensing system. The main contributions are:

- the fabrication by means of lithographic methods of a flexible electrochemical platform with three WEs, a silver RE and a temperature sensor on a PI substrate;
- the successful electrochemical characterization of the platform under normal conditions and during bending;
- several reference membranes were compared to produce an efficient flexible RE;
- the flexible RE was found to have good stability over time and was efficiently used to calibrate a Li^+ ISE;
- the complete flexible and integrated electrochemical system was efficiently used to sense lithium both in aqueous solution and in artificial perspiration with good analytical results;
- the calibration of the temperature gave a perfect linear response and values comparable to the theoretical ones.

In conclusion, an efficient electrochemical flexible platform with several sensing sites, a stable reference system and an accurate temperature sensor was fabricated. This represents the first step towards the development of a complete wearable system for sweat sensing applications.

To fabricate wearable sensing systems we must consider the integration of different heterogeneous components: properly-designed electrodes for efficient multi-panel detection and fabrication compatibility, a fluidics transporting the sample to the sensing area, an electronic read-out circuitry for signal acquisition and data transmission. The combination of these different elements is far from trivial and must be conceived carefully.

In this chapter, we address these challenges in order to build and test a fully wearable system for ion sensing in human sweat.

6.1 Optimization of platform design and wells

Effects of electrodes area and contacts pitch

In Chapter 3, the deposition of platinum nanoflowers on both macro and miniaturized electrodes has been described. The first design of the custom-made platform was based on the use of macro-electrodes. In subsequent attempts also flexible micro-electrodes with a radius of 500 nm have been fabricated. A smaller pitch (2.54 mm) was used in this case to reduce the dimensions of the whole platform. The deposition of platinum nanoflowers on those electrodes by means of the LSV technique described in Section 3.5 was found to be successful. This proves the possibility to create miniaturized electrodes in applications in which this is necessary. An image of the microfabricated platform is given in Figure 6.1.

In our case the use of micro-electrodes is not crucial as the gain of space is not particularly significant. Consequently, for the sake of simplicity, macro-electrodes will be used in the last tests of the platform.

In the final design, the passivation opening areas were increased in order to enable easier release from the silicon wafer during the anodic dissolution in NaCl. In fact, the larger the

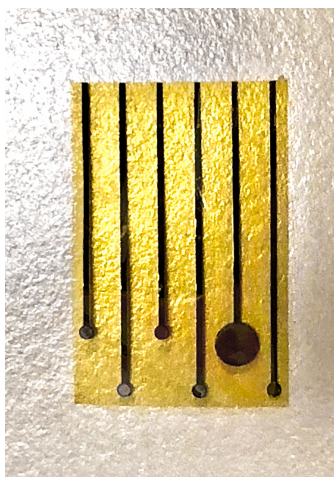


Figura 6.1 – Image of the microfabricated flexible platform with smaller pitch (2.54 cm) and smaller electrodes dimension (radius of 500 μm).

exposed aluminum layers after the dry etching step described in Chapter 5, the easier the possibility of the NaCl solution to wet the aluminum areas below each PI platform.

Realization of electrodes wells

The custom-made platform proposed here contains different ISEs, a RE and a temperature sensor, as explained before. Consequently, during the fabrication process it is necessary to ensure efficient drop-casting of each membrane on top of the corresponding electrode, without the risk of intermixing between neighbouring sites. The cocktail solutions used in this work wet well the flexible PI substrate, thus they easily spread over the surface, causing possible contamination. In addition, also after the fabrication of the membranes, different conditioning solution must be used on each electrode to improve the sensing performance. Therefore, it is important to find an efficient method that enables the isolation of each electrode solution from the other. Different ideas have been tested to address this issue. They are reported below.

At a first attempt, the drop-casting of smaller volumes of cocktail solution on top of each electrode was investigated. In principle, this reduces the spread of the liquid outside of the target electrode. However, the control on the process is not very high, especially because the flexible PI substrate normally has a certain curvature due to the internal stresses caused by the microfabrication process.

As a second attempt, wells made of PVC adhesive tape were tried. However, the adhesion between the tape and the PI substrate is not optimal, causing leakage of liquid among neighbouring electrodes.

The fabrication of silicone wells is also studied, but the control on the process is very limited.

Finally, the optimal solution is found to be the use of a thick Kapton adhesive tape. Wells of 4 mm are fabricated with a punch cutter. The adhesion between the two PI layers is found to be optimal. No leakage between neighbouring sites is occurring. A picture of the final system is shown in Figure 6.2.

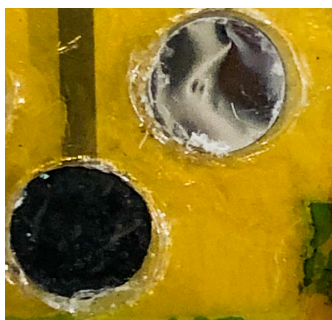


Figura 6.2 – Image of the platform wells obtained with the adhesive Kapton tape to avoid intermixing of the membranes cocktails and of the conditioning solutions among neighbouring electrodes.

6.2 Optimization of the fluidic system

The realization of an efficient fluidic system for the transport of the biofluid to the sensing area and the subsequent disposal of the already tested sample is crucial to ensure accuracy. Paper (in different forms) is the material of choice in order to have a simple low-cost system.

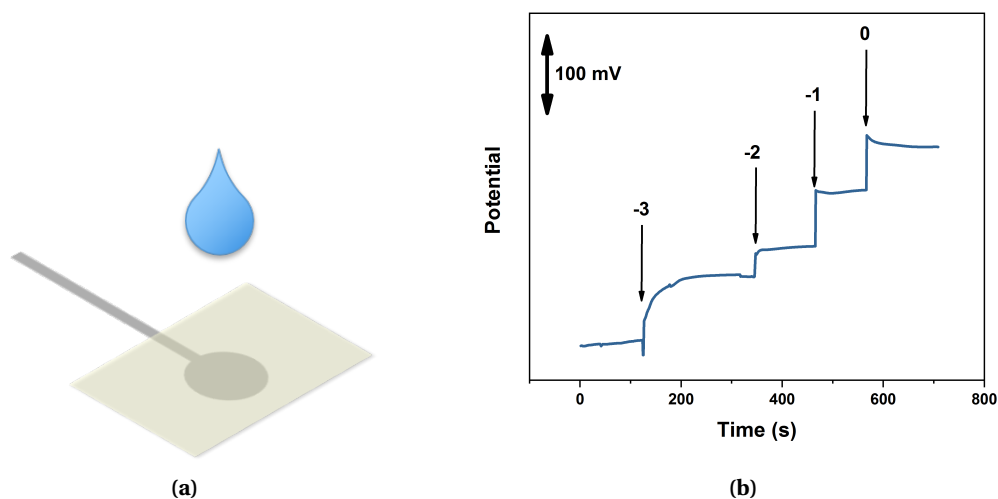


Figura 6.3 – Fluidic test with fast adsorbing Whatman paper on a lithium-selective electrode: a) scheme of the experimental setup; b) obtained time trace at increasing LiCl concentration.

The first material which has been tested is Whatman filter paper in different grades. The initial

tests are simply based on the use of rectangular fast adsorbing Whatman paper in order to see the response of the sensing system to a paper fluidics. The setup is shown in Figure 6.3a. A significant amount of LiCl solution at increasing concentration was drop-cast on top of the fluidic system, while measuring the electrode potential. The corresponding curve is given in Figure 6.3b. It is possible to conclude that the signal recorded by wetting the electrodes with a Whatman paper fluidics is comparable to the one obtained in solution.

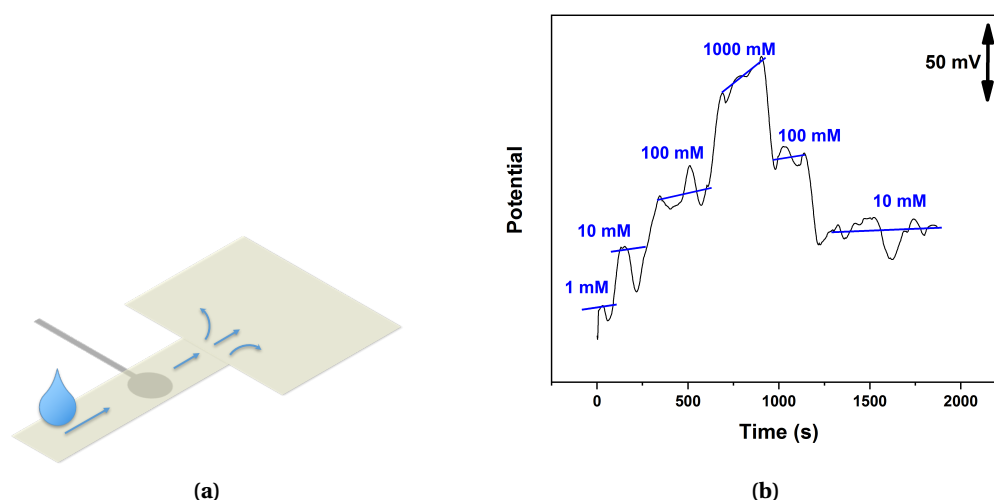


Figure 6.4 – Fluidic test with fast adsorbing Whatman paper on a lithium-selective electrode: a) scheme of fluidic design and experimental setup; b) obtained time trace while going up and down in LiCl concentration.

The previous experiments prove the feasibility of using paper to bring the liquid onto the sensors. However, in order to have accurate results, we need to create a system that is able to transport always fresh sweat onto the sensing surface and to dispose the already tested perspiration. For this reason, a second test is performed with the use of a mannequin to simulate the final setup of the wearable system. At a first stage, a fast adsorbing paper is combined with a slow adsorbing one in a shape like the one in Figure 6.4a. The two pieces of paper are attached using a general-purpose glue. The original idea is to have fast adsorption in the sensing regions (corresponding to area of the narrow channel) in order to always have fresh sweat on the electrodes surface. For this reason a fast adsorbing paper is used for this part of the fluidics. On the contrary, the wider portion enables a slower flow that will act as a reservoir, thanks also to the use of a slower adsorbing filter paper. However, the connection between the two types of paper is found to act as a bottleneck to the continuity of the flow. For this reason, subsequent experiments are based on the use only of the fast adsorbing filter paper.

A fluidic system made entirely of fast adsorbing Whatman paper was fabricated and put in place thanks to the use of a commercial sport headband. A solution of LiCl from a concentration

of 1 mM up to 1M was deposited on one side of the fluidic system, while measuring the sensor potential. The resulting curve is shown in Figure 6.4. It is possible to see that in general the plateau is rising when the concentration is going up. A good reversibility is also evident when the concentration is lowered. However, there is a significant oscillation in the measured signal. This can be explained by considering that the liquid is sucked away from the electrodes by the fluidic system. Consequently, the area over the sensor is drying and the paper is slightly detaching from the electrodes, causing a change in the potentiometric signal.

In order to avoid this signal oscillation due to drying of the paper, two methods were investigated. The first one is based on the use of a surgical grade tape by 3M in order to firmly attach the fluidics to the sensor surface. The second one investigates alternative soaking materials. In particular make-up pads and wound adsorbent patches were tested and compared.

The adsorbing capability of each material was tested by immersing the narrow region in a Petri dish full of stained water. The reservoirs were made with different numbers of layers to increase the capacity. The images of the different flows are reported in Figure 6.5. The three samples corresponds to different numbers of layers in the reservoir. One, two and three layers of materials were used for the measurements. Thus, in each picture from left to right we increase the reservoir capacity.

It is possible to observe that samples having a reservoir with lower capacity (i.e. left samples) fill up faster then the others, as expected. In addition, at a first look Whatman paper does not seem to be able to completely fill the reservoir, also at long times. In addition, the filling is slower.

A quantitative analysis was obtained by measuring the amount of remaining liquid in each Petri dish at the end of tests. The results are reported in the graph in Figure 6.6. It is evident that the slowest adsorption is the one of the Whatman paper fluidics, as expected. It is also possible to see that the use of multiple layers of Whatman papers in the reservoir does not contribute significantly to the increase of the capacity. This phenomenon can be explained by the considering the low adherence between different layers, as highlighted also in the initial experiments combining different grades of Whatman paper. On the contrary, the make-up cotton patch shows the highest adsorbing rate and a large increase in reservoir capacitance when multiple layers are used. However, this system was found to be quite delicate. In fact, it ravel when completely soaked. To solve this issue a medical grade surgical tape by 3M was used to cover the reservoir and firmly attach the narrow channel to the sensing surface. This expedient is useful both to avoid displacements and detachments of the fluidic system and to ensure no contamination from the already tested sweat, as in this way the reservoir is isolated from the skin surface.

For the reasons explained before, the cotton make-up patches were used for the fabrication of the final fluidic system. A potentiometric measurement at increasing and decreasing concentrations was performed to test the capability of the system to detect changes in concentrations without contamination. The fluid was drop-cast on one side of the narrow channel in or-

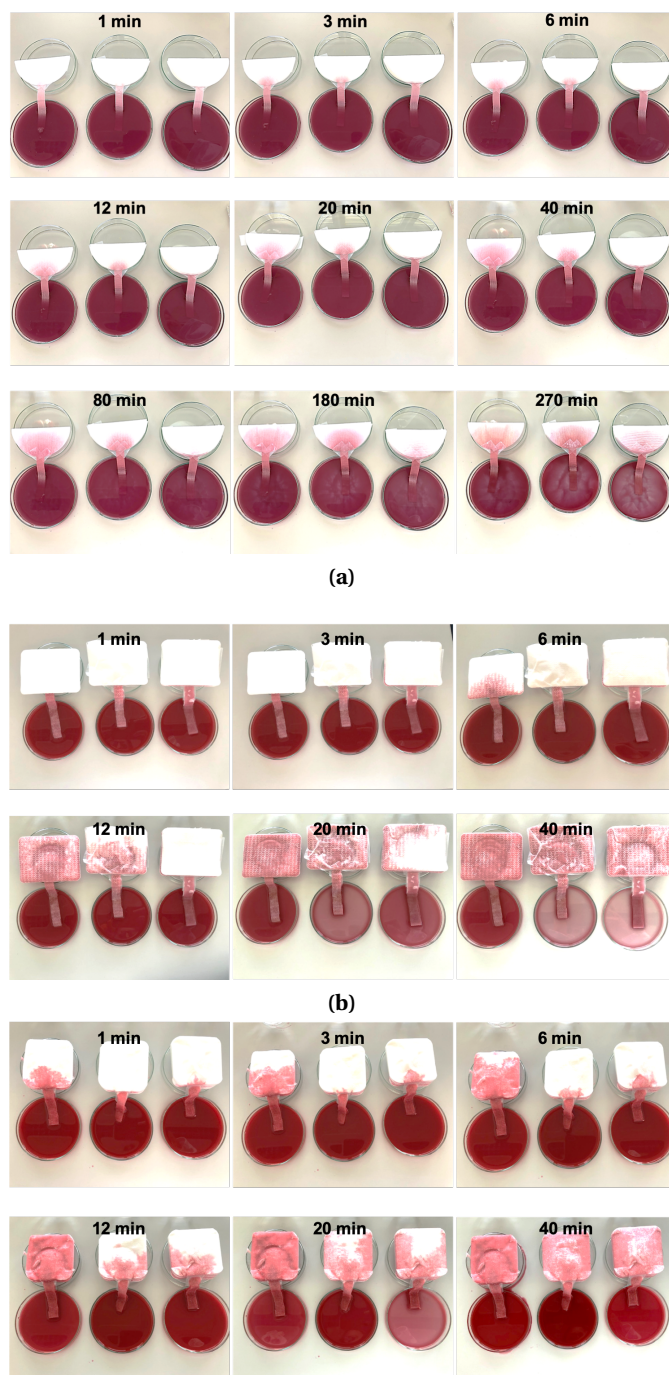


Figura 6.5 – Adsorbing tests of fluidic systems fabricated with different materials: a) Whatman paper; b) wound adsorbent patch; c) make-up removing patch. The samples on the left of each picture are using 1 layer for the reservoir, the sample in the middle 2 layers and the one on the right 3.

der to simulate the region where the sweat will be produced and soaked from the skin. The successfull outcome of the experiments is shown in Figure 6.7.

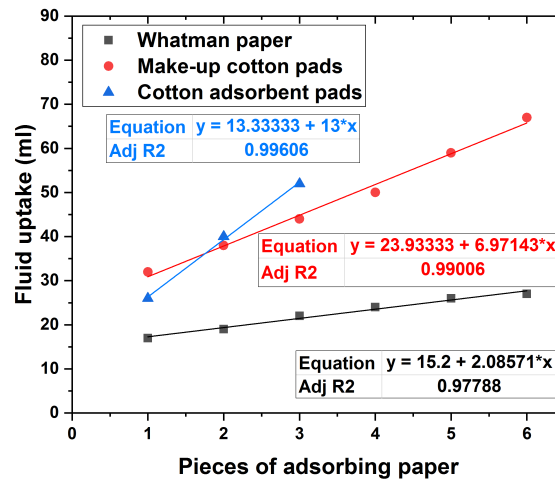


Figura 6.6 – Comparison of the adsorbing power of different fluidic systems (Whatman paper, make-up removing pads and cotton adsorbent patches).

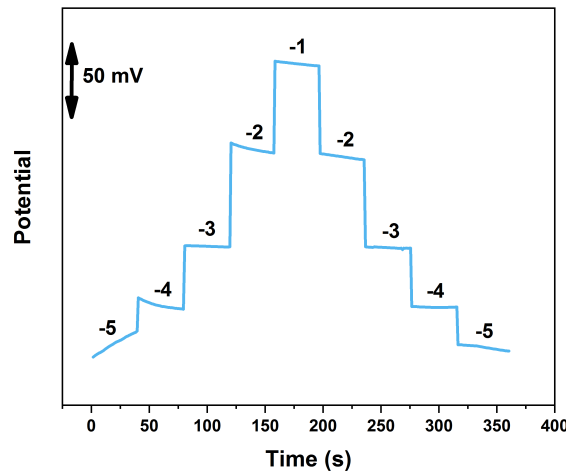


Figura 6.7 – Test of the final fluidics made with make-up cotton pads while increasing and decreasing lithium concentration. The fluid is drop-cast on one side of the narrow channel in order to simulate the region where the sweat will be produced and soaked.

6.3 Tests with portable read-out electronics

The platform was also tested successfully with different custom-made portable read-out systems, proving the possibility to realize a completely wearable system for non-invasive monitoring of electrolytes.

The first hardware front-end that is tested with the developed sensors is reported in Figure 6.8.

The hardware front-end is manufactured on a 1.6 mm FR4 substrate with 54×64 mm size. It enables multi-sensing of up to four endogenous electrolytes. A temperature readout circuit is also present. The platform has been tested with potassium and sodium selective electrodes. The hardware is remotely controlled by an user interface that configures the sensor panel and collects the biological data through a Bluetooth link. Since the electronic system has been realized by another PhD student of the reserach group, Ivan Ny Hanitra, we refer the reader to [17] for more information on design and fabrication.

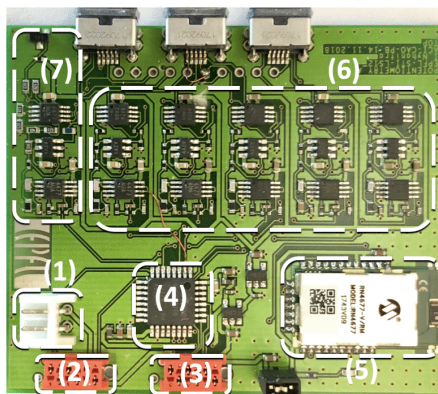


Figura 6.8 – Different blocks of the potentiometric board: (1) socket for the power supply, (2) Programming/Debugging Interface, (3) UART serial port and alternative power supply, (4) microcontroller unit, (5) Bluetooth module, (6) four-channels potentiometric readout and pH readout circuitry, (7) temperature readout block. Reprinted with permission from [17]. ©[2019]IEEE

Potassium and sodium sensors were fabricated as described in Chapter 4. Figure 6.9 shows the calibration of the potassium sensor with the hardware front-end. This is performed by subsequent Li^+ addition in the range 10^{-9} -0.1 M. The corresponding time trace is reported in the small inset on top left. It is possible to observe that a near-Nernstian response (57.3 ± 1.1 mV/decade) is achieved from the calibration curve. The lower LOD, computed according to the IUPAC definition, is of about 5 ± 1 μM . This falls within the range of physiological interest for potassium in sweat that is 1–40 mM. The same potassium sensor calibration was compared with the one obtained with an Autolab potentiostat by Metrohm. The values obtained in this case were very similar (sensitivity of 57.8 ± 1.2 mV/decade, LOD of 4.2 ± 1 μM), proving the efficiency of the fully integrated sensing system.

Likewise, the calibration of the sodium sensor with the read-out electronics is reported in Fig. 6.10. The potentiometric response offers quasi-Nernstian behavior with a sensitivity of 57.7 ± 1.5 mV/decade and lower LOD of 2.5 ± 1 μM , within the range of clinical interest for sodium (1–160 mM). The same calibration performed with an Autolab potentiostat gives a sensitivity of 58.5 ± 1 mV/decade and lower LOD of 3.5 ± 1 μM . The similarity of the results further proves the accuracy of the system.

Subsequently, lithium-selective electrodes were also tested with a new and more complete version of read-out electronics. A smaller hardware front-end, of 38×76 mm in size, is

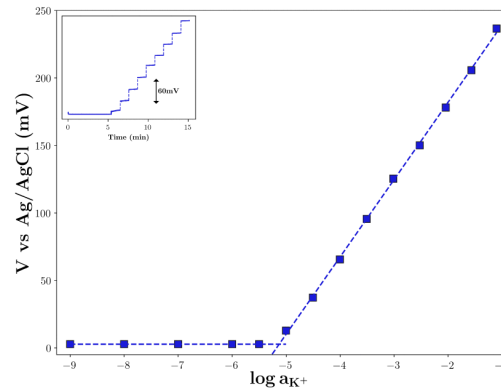


Figure 6.9 – Potassium sensor calibration in water background electrolyte. Reprinted with permission from [17]. ©[2019]IEEE

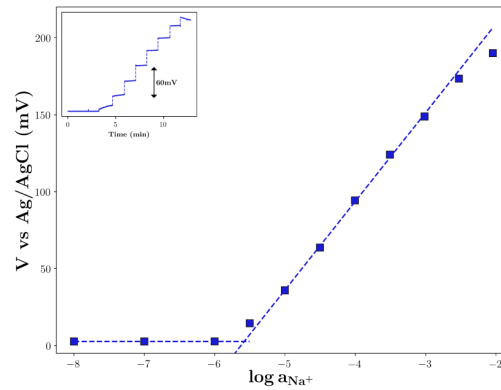


Figure 6.10 – Sodium sensor calibration in water background electrolyte. Reprinted with permission from [17]. ©[2019]IEEE

mounted on a 1.6 mm double side FR4 substrate. This is called the AmpPot board. The different blocks constituting the readout front-end are highlighted in Figure 6.11. Since also this electronic system has been realized by another PhD student of the group, Ivan Ny Hanitra, we refer the reader to [18] for more information on the fabrication and circuits.

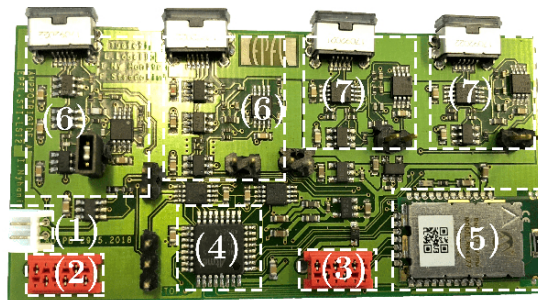


Figure 6.11 – Different blocks constituting AmpPot board: (1) power supply socket, (2) programming/debugging interface, (3) UART/I2C serial ports, (4) microcontroller unit, (5) Bluetooth module, (6) amperometric readout blocks, (7) potentiometric readout blocks. Reprinted with permission from [18]. ©[2020]IEEE

Lithium-selective electrodes were fabricated as described in 4. A water solution of LiCl is gradually added to obtain concentrations from 10^{-8} to 0.1 M. The calibration curve of the lithium sensor is reported in Figure 6.12. The corresponding time trace is reported in the small inset on the top left. The sensitivity of the sensor is 55.6 ± 1.16 mV/decade, proving its quasi-Nernstian behaviour. An LOD of 11 ± 3.5 μ M is obtained. This is well below the minimum effective concentration of lithium drug in sweat (~ 2.1 mM [113]). The results were compared with the ones obtained with a commercial Autolab potentiostat by Metrohm. The comparison is reported in Table 6.1. The measurements with AmpPot board yield lower sensitivity but very good linearity. Besides, the LODs are comparable.

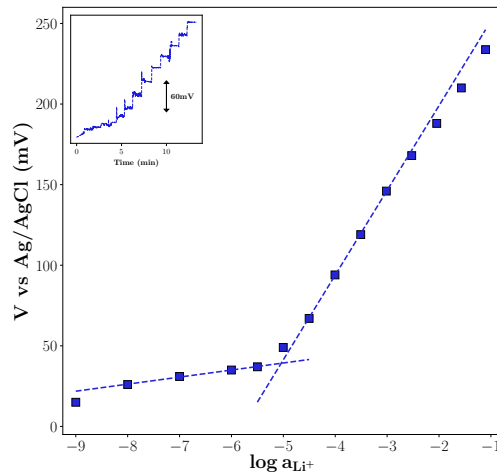


Figure 6.12 – Lithium sensor calibration in water background electrolyte. Reprinted with permission from [18]. ©[2020]IEEE

Tabella 6.1 – Performance of the developed front-end on the developed lithium ISE [18]

	AmpPot board	Autolab
Sensitivity (mV/decade)	55.6 ± 1.16	61.9 ± 0.48
Root mean square error (mV)	0.5	0.1
Coefficient of determination R^2	0.9994	0.9994
LOD (μ M)	11.0 ± 3.50	12.4 ± 2.40

In conclusion, in this section the possibility to use the developed nanostructured ISEs in combination with different custom-made electronics is proved, towards the development of wearable ion-sensing platforms.

6.4 Testing of the whole system in artificial and in real sweat

In the previous section the optimization of the sensing platform, the study of an efficient fluidic system and the interfacing with the electronics was discussed. This section focuses on the integration of the different elements to create a functional wearable electrochemical

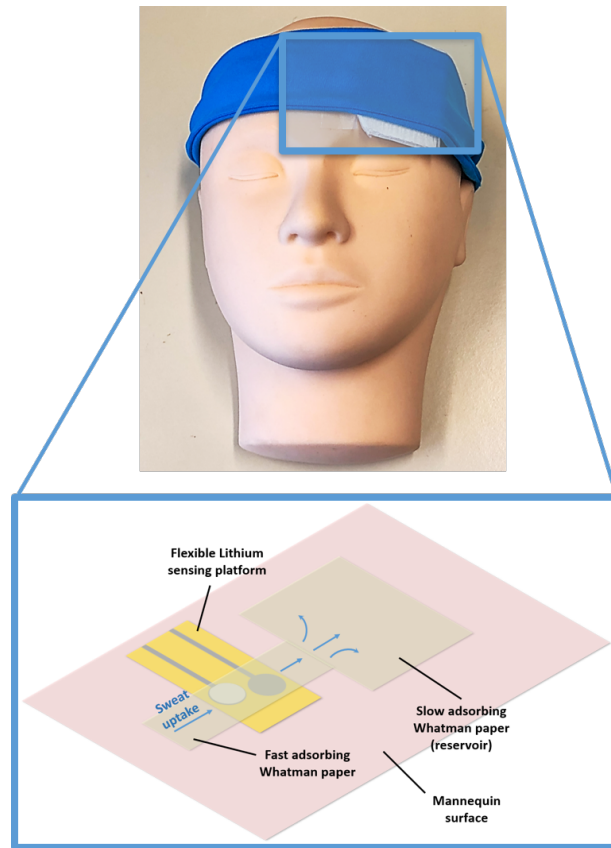


Figura 6.13 – Experimental setup to simulate in-situ measurements using our wearable lithium-sensing system. [19]

sensing system. In the first part the realization of a non-invasive lithium sensing device with a paper fluidic system is reported. In the second part, a complete wearable multi-electrode platform for ion-sensing is fabricated and tested in artificial sweat for different applications. The system includes 4 electrodes for the detection of Li^+ , Pb^{2+} , K^+ and Na^+ and a temperature sensor.

6.4.1 A wearable electrochemical sensing system for lithium monitoring

As explained in Section 6.2, we need to create a system that is able to transport always fresh sweat onto the sensing surface and to dispose the already tested perspiration in order to have accurate results. A mannequin to simulate the final setup of the wearable system is used to mimic the functioning of the whole system (Fig. 6.13). A fast adsorbing paper is combined with a slow adsorbing one in a shape like the one in the zoomed inset in Figure 6.13. The two pieces of paper are attached using a general-purpose glue in order to ensure fast adsorption in the sensing regions (corresponding to the area of the narrow channel) and slow adsorption in the reservoir. In this way, continuous collection of untested perspiration from the skin is achieved on the sensor surface, while the already tested sweat is disposed in the large reservoir

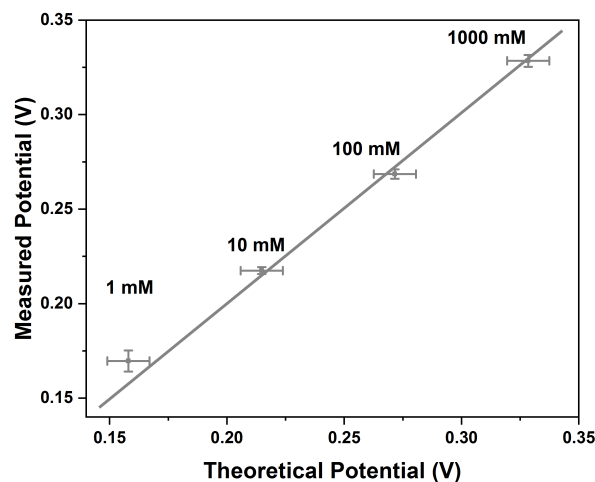


Figura 6.14 – Comparison between the potential values obtained with the proposed wearable lithium-sensing system with respect to the predicted ones. [19]

made of slow adsorbing Whatman paper.

The proper functioning of the complete wearable electrochemical sensing system is assessed by measuring the cell potential at different lithium ion concentrations in artificial sweat. The measured potential values are then compared to the ones predicted from the calibrations. The results are reported in Figure 6.14. It is possible to observe that the sensing system has a good predictability. With this results, we prove the promising potential of the proposed integrated non-invasive lithium sensing system for remote drug dose optimization, without the need of invasive procedures like blood collection. This results is of key importance since it paves the way for new tools in monitoring and personalized medicine of BD.

6.4.2 Wearable multi-sensing platform for ion sensing in sweat

System overview

The complete wearable multi-sensing platform for ion-sensing in sweat is built. The overview of the system is given in Figure 6.15. The flexible electrochemical platform consists of four ion-sensing sites for different applications: a Li^+ -ISE for TDM of psychiatric disorders, a Pb^{2+} -ISE for monitoring of heavy metal contamination, a Na^+ -ISE and a K^+ -ISE for hydration and physical exercise tracking. In addition, a body temperature sensor has also been implemented on the platform in the form of a platinum serpentine. For more details on the fabrication of each part of the sensing system we refer the reader to Chapters 4 and 5.

Considering the experiments reported in Section 6.2, a cotton fluidics as the one reported in Figure 6.16 has been fabricated to ensure the uptake of fresh sweat on the sensing surface and

6.4. Testing of the whole system in artificial and in real sweat

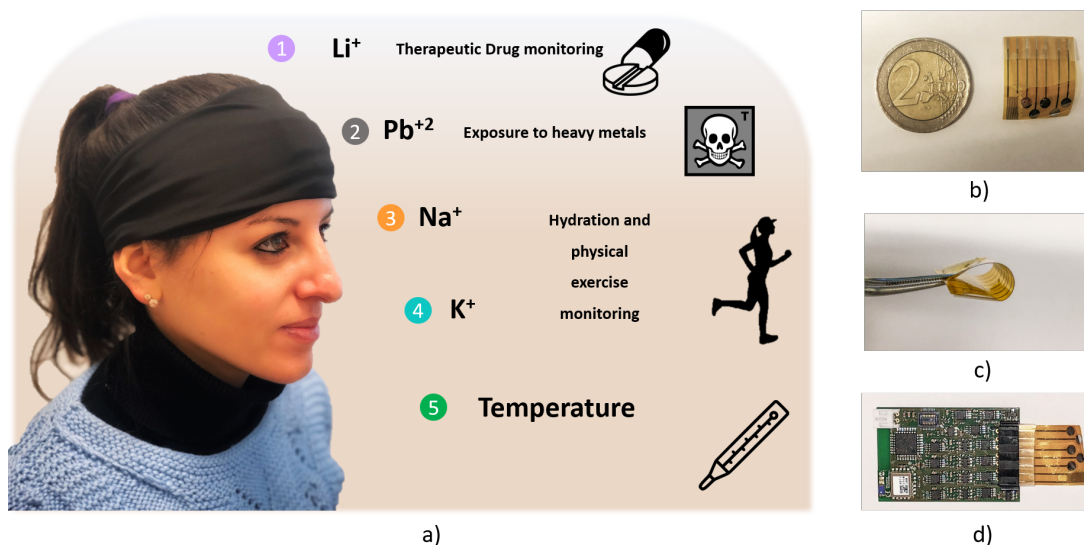


Figura 6.15 – Overview of the wearable headband for ion-sensing in sweat: a) different sensing sites available on the flexible electrochemical platform; b) picture of the fabricated flexible electrochemical platform on a PI substrate; c) flexibility of the fabricated electrochemical platform; d) read-out electronics for potentiometric sensors. [20]

the disposal of the already tested fluid in the reservoir.

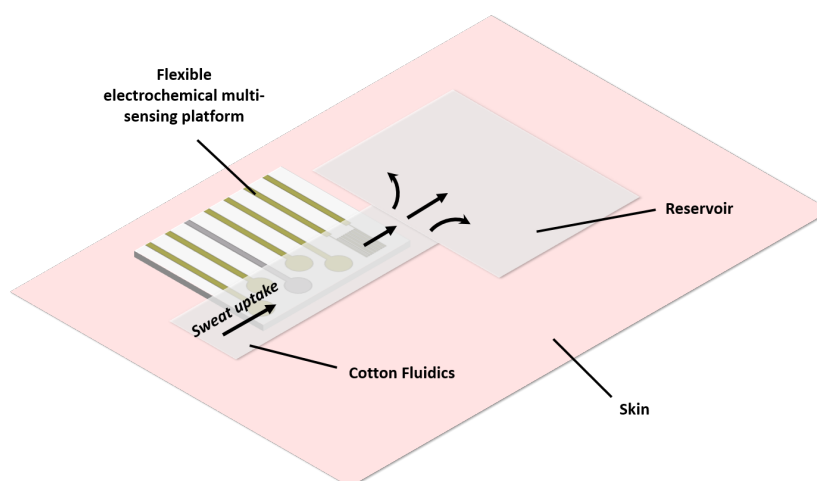


Figura 6.16 – Cotton fluidics of the complete wearable headband for ion-sensing in sweat. [20]

Selectivity test in artificial sweat

The analytical capabilities and the selectivity of the system were tested in artificial sweat during the consequent exposure of the platform to 10 mM solutions of the four different ions. The potentiometric curves that were obtained are reported in Figure 6.17. It is possible to observe that each sensors is highly sensitive to its target ion, with sharp steps after the

exposure to the corresponding ion solution. On the contrary, when each ISE is exposed to the solution of an interfering ion, the signal is significantly reduced. Therefore, it is evident that the multi-sensing platform is able to detect each target ion with good accuracy and limited interference due to the presence of other ions in solution. As expected a small signal is present on the Na^+ curve when K^+ is added, as these two ions have similar ionic radius. However, the difference in step height is extremely significant, proving the good selectivity of the system.

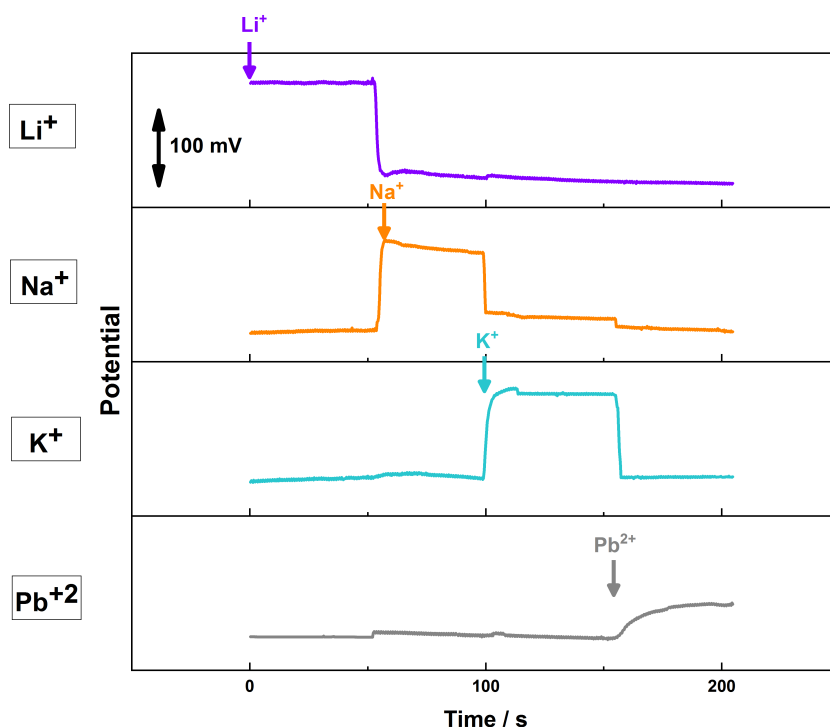


Figura 6.17 – Potentiometric response of each electrode of the flexible electrochemical multi-sensing platform during subsequent exposure to 10 mM LiCl, 10 mM NaCl, 10 mM KCl and 10 mM $\text{Pb}(\text{NO}_3)_2$ in artificial sweat. [20]

6.4.3 Test on human volunteers

The wearable electrochemical sensing platform was finally tested on human volunteers for sodium and potassium monitoring to prove its efficiency. Naturally lithium and lead were not considered because of the complications that those two compounds would imply for the tests: the first would require the testing on people suffering from people disorder under lithium drug therapies, the second one would need the deposition of a highly poisoning compound on the human skin. Therefore, the unfeasibility of the experiments both with lithium and lead is clear.

The tests were approved by the Ethical Commission of Canton Vaud. Five volunteers were

6.4. Testing of the whole system in artificial and in real sweat

asked to cycle indoor for 30 minutes after the starting of the perspiration. The experimental setup is shown in Figure 6.18. An EMF6 electrochemical interface by Lawson Lab was used for data collection. In-situ and ex-situ measurements were compared. The sampling interval was set to 5 minutes in order to enable the subsequent attachment and detachment of cotton pads to be used for the ex-situ measurements.



Figure 6.18 – Experimental setup used for the testing of the wearable platform on human volunteers.

It is clear from Figure 6.19 that the concentration of both sodium and potassium is increasing with time, as expected. In fact, as dehydration starts, there is a progressive loss of water, which causes an increase of the ionic concentrations in sweat. Furthermore, a good correlation between in-situ and ex-situ values is found for both ions.

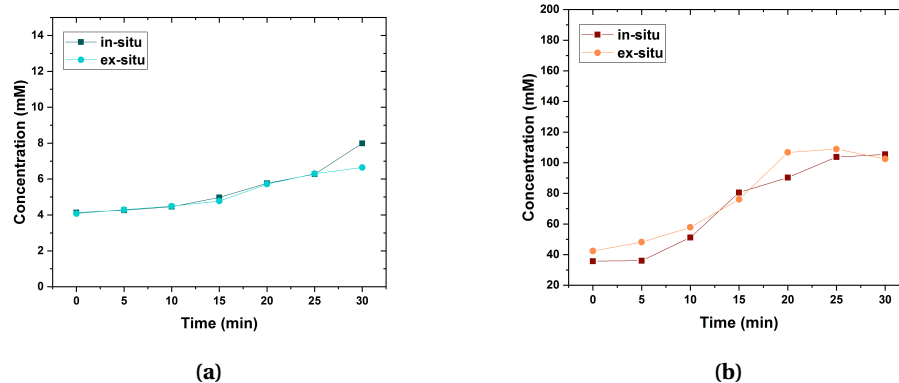


Figure 6.19 – Potassium and sodium trends in the sweat of a volunteer during 30 minutes of indoor cycling after the perspiration starts. [20]

This result is further corroborated by considering the scatter plots for the two ions. They

are reported in Figure 6.20. It is evident that a very good correlation between the potentials measured in-situ and ex-situ is achieved, thus proving the efficiency of the complete wearable multi-sensing system proposed and fabricated in this work.

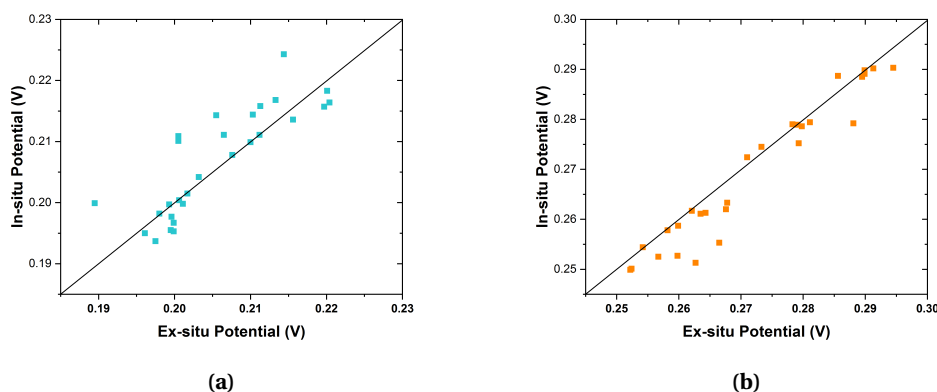


Figure 6.20 – Scatter plots of potassium and sodium comparing the in-situ and ex-situ measurements in the sweat of a volunteer during 30 minutes of indoor cycling after the perspiration starts. [20]

6.5 Main contributions and conclusions

The integration of the previously described flexible ion-sensing system in a complete wearable headband is described in this chapter. The main contributions are reported below.

- Electrode wells are fabricated to facilitate the deposition and conditioning of the ISMs, thus improving reproducibility.
- A cotton fluidics able to ensure the uptake of fresh sweat and dispose the already tested fluid is demonstrated.
- The possibility to use the developed nanostructured ISEs in combination with different custom-made readout electronics is also reported.
- The analytical capability of the sensing system and the limited interference is demonstrated on a simulated setup on a mannequin.
- Finally, the wearable headband was tested successfully on human volunteers for potassium and sodium sensing during physical exercise.

In conclusion, in this chapter the realization of a complete wearable headband able to monitor simultaneously four different ions in sweat is demonstrated. These results open interesting perspectives in the emerging field of e-Health and personalized medicine, towards a better and less-invasive healthcare for different applications.

Conclusions and future work

The data-driven healthcare revolution of the last two decades has boosted the research towards the development of efficient and low-cost remote sensing system, with particular interest for wearable devices that enable continuous tracking and personalized treatments without the need of moving the patient and/or the physician to clinics or hospitals. Despite the great research efforts, current wearable biosensors still have to address several unsolved issues, such as separate sampling and analysis, poor collection, low multi-sensing capabilities and lack of data correlating sweat and blood values. Progress in materials science to enhance sensitivity, selectivity, detection range and to reduce costs is also needed. This thesis investigates and addresses some of the challenges related to wearable chemical sensors, with particular interest on the promising field of sweat sensing.

The main contributions of this thesis are summarized below:

- **The fabrication of highly stable all-solid-state SC-ISEs exploiting gold and platinum nanostructures by fast electrodeposition procedures.** The deposition process requires less than 4 minutes. A detailed characterization and comparison between different types of gold and platinum nanostructures in terms of morphology and electrochemical behaviour and the study of substrate influence, reversibility and stability over time is carried out. Gold and platinum nanostructures have also been combined in various stacks to further improve the SC capacitance (up to 196 μF), and thus potential stability. The development of an alternative fast electrodeposition procedure of platinum nanoflowers on miniaturized sensors is also discussed.
- **The non-invasive optimization of lithium drug dose via sweat analysis is proposed for the first time to eliminate the need of hospitalization.** The feasibility of the measurement is proved by testing in artificial perspiration. A quasi Nernstian response (57.6 ± 2.1 mV/decade) is obtained, with a LOD of 1.4 ± 0.2 mM, that is well below the therapeutic window of lithium drug in sweat (2.4-4.5 mM).

- **A novel device for monitoring the exposure to heavy metals of people in risky environments by perspiration analysis is fabricated.** The feasibility of measurement of lead concentration is demonstrated in artificial sweat with great analytical performance. To the best of our knowledge, it is the first time that the exposure to risky environments is proposed by means of perspiration analysis. A quasi-Nernstian calibration (28.9 ± 1.7 mV/decade) is obtained within the range of clinical interest.
- **The design and realization of a complete flexible electrochemical multi-sensing system by means of lithographic methods.** This includes the integration of a stable all-solid-state Ag RE and a temperature sensor. The platform is successfully tested in normal conditions and during bending at 180° . The complete flexible and integrated electrochemical system is efficiently used to sense lithium both in aqueous solution and in artificial perspiration with good analytical results: in particular, a sensitivity of 56.8 ± 3.9 mV/decade with a LOD of 1.7 ± 0.6 mM is obtained. The calibration of the temperature gives a perfect linear response and values comparable to the theoretical ones.
- **The integration in a complete wearable multi-sensing headband for ion-monitoring in sweat.** Wearable sensing systems must consider the integration of duly-functionalized electrodes for efficient detection of different ions, the microfluidics transporting the sample to the sensing area, an electronics read-out. A cotton fluidics is designed in this work to ensure the collection of fresh sweat and the disposal of the already tested sample fluid. The platform is successfully tested with several custom-made electronic circuitry to test the possibility to interface the system with small potentiometric read-out boards. The analytical capability and the selectivity of the complete system is tested in artificial sweat with a wearable setup using a mannequin for the detection of lithium, sodium, potassium and lead.
- **Finally the wearable headband is successfully tested on human volunteers for potassium and sodium monitoring during physical exercise.** As expected, the ionic concentrations increases with dehydration. In addition, the good correlation between ex-situ and ex-situ values is proved on all volunteers.

The results reported in this thesis confirm the promising performance of the prototype. However, further research needs to be carried out to improve the system. Some interesting aspects for future work are reported here:

- **Integration with a sweat stimulation system.** The wearable multi-sensing headband includes a flexible electrochemical platform and a cotton fluidic system to ensure the collection of fresh sweat from the skin. Human volunteers are required to perform some physical exercise for sweat stimulation. The integration of an artificial sweat production system (based for instance on iontophoresis) is an important future step for the development of a complete and user-friendly device.

-
- **Further testing on human volunteers.** After ethical approval (under request) of the planned experiments, the testing of the complete system on human volunteers for complete validation is envisioned. This will require the collaboration with the psychiatric department of an hospital for lithium dose optimization and with people exposed to risky environment for heavy metal detection.
 - **Clinical research on blood/sweat correlation and excretion mechanism in perspiration.** One of the main limitations of the emerging field of sweat sensing is the reduced number of studies carried out by the medical and biochemical community to further corroborate sweat and blood correlation, as well as understand better the excretion of metabolites and electrolytes in perspiration. This aspect is crucial in order to target the research efforts in the correct directions and to optimize the sensing parameters to achieve high accuracy and reproducibility.
 - **Extension of the system for the detection of other sweat metabolites.** The present system focuses on the measurements of body temperature and ions. However, as explained in Chapter 1, sweat contains a huge amount of biological information. The sensing of other metabolites, like cortisol for stress monitoring or cancer biomarkers for early-disease detection, could be implemented on the platform to enlarge the application areas.
 - **Extension to other fields in which ion sensing is important.** This work focuses on ion sensing for healthcare. However, ion sensors find application in several other fields, like food and water quality monitoring, control of industrial processes, agriculture and fishery.
 - **Design and fabrication of optimized electronics.** A small and custom-made read-out system to enable fast and continuous multi-channel sensing without consuming too much power is essential in every wearable sensor. In this thesis the interface of the fabricated electrochemical multi-sensing system with several custom-made boards has been reported. However, further optimization of the electronic design can be obtained to reduce system dimensions and power consumption, improve accuracy and create a user-friendly interface.

We hope that the present work will open up new perspectives and boost further research in the promising field of sweat and wearable biosensing for a better and less-invasive next generation healthcare.

Bibliografia

- [1] M. G. de Lecea and M. Rossbach, “Translational genomics in personalized medicine – scientific challenges en route to clinical practice,” *The HUGO Journal*, vol. 6, no. 1, p. 2, 2012.
- [2] C. Legner, U. Kalwa, V. Patel, A. Chesmore, and S. Pandey, “Sweat sensing in the smart wearables era: Towards integrative, multifunctional and body-compliant perspiration analysis,” *Sensors and Actuators, A: Physical*, vol. 296, pp. 200–221, 2019.
- [3] M. Chung, G. Fortunato, and N. Radacsi, “Wearable flexible sweat sensors for healthcare monitoring: a review,” *Journal of The Royal Society Interface*, vol. 16, pp. 1–15, 2019.
- [4] M. Novell, M. Parrilla, G. A. Crespo, F. X. Rius, and F. J. Andrade, “Paper-based ion-selective potentiometric sensors,” *Anal. Chem.*, vol. 84, no. 11, pp. 4695–4702, 2012.
- [5] T. Guinovart, M. Parrilla, G. A. Crespo, F. X. Rius, and F. J. Andrade, “Potentiometric sensors using cotton yarns, carbon nanotubes and polymeric membranes,” *Analyst*, vol. 138, no. 18, p. 5208, 2013.
- [6] A. J. Bandodkar, V. W. Hung, W. Jia, G. Valdés-Ramírez, J. R. Windmiller, A. G. Martinez, J. Ramírez, G. Chan, K. Kerman, and J. Wang, “Tattoo-based potentiometric ion-selective sensors for epidermal pH monitoring,” *Analyst*, vol. 138, no. 1, pp. 123–128, 2013.
- [7] T. Guinovart, A. J. Bandodkar, J. R. Windmiller, F. J. Andrade, and J. Wang, “A potentiometric tattoo sensor for monitoring ammonium in sweat,” *The Analyst*, vol. 138, no. 22, pp. 7031–8, 2013.
- [8] W. Gao, S. Emaminejad, H. Y. Y. Nyein, and S. Challa, “Fully integrated wearable sensor arrays for multiplexed in situ perspiration analysis,” *Nature*, vol. 529, no. 7587, pp. 509–514, 2016.

- [9] S. Wang, Y. Wu, Y. Gu, T. Li, H. Luo, L. H. Li, Y. Bai, L. Li, L. Liu, Y. Cao, H. Ding, and T. Zhang, "Wearable Sweatband Sensor Platform Based on Gold Nanodendrite Array as Efficient Solid Contact of Ion-Selective Electrode," *Anal. Chem.*, vol. 89, no. 19, pp. 10224–10231, 2017.
- [10] F. Criscuolo, I. Taurino, F. Stradolini, S. Carrara, and G. De Micheli, "Highly-stable Li⁺ ion-selective electrode based on noble metal nanostructures as solid-contacts," *Anal. Chim. Acta*, vol. 1027, pp. 22–32, 2018.
- [11] F. Criscuolo, L. Lobello, I. Taurino, D. Demarchi, S. Carrara, and G. D. Micheli, "Mixed gold and platinum nanostructured layers for all-solid-state ion sensors," in *IEEE Sensors Conference*, 2018.
- [12] F. Criscuolo, I. Taurino, V. A. Dam, and F. Catthoor, "Fast Procedures for the Electrodeposition of Platinum Nanostructures on Miniaturized Electrodes for," *Sensors*, vol. 19, no. 2260, pp. 1–12, 2019.
- [13] F. Criscuolo, F. Cantù, I. Taurino, S. Carrara, and G. D. Micheli, "Flexible sweat sensors for non-invasive optimization of lithium dose in psychiatric disorders," in *IEEE sensors*, 2019.
- [14] F. Criscuolo, I. Taurino, S. Carrara, and G. D. Micheli, "A novel electrochemical sensor for non-invasive monitoring of lithium levels in mood disorders," in *EMBC 2018*, pp. 3825–3828, 2018.
- [15] S. Carrara, *Bio/CMOS Interfaces and Co-Design*. Springer, 2013.
- [16] F. Criscuolo, M. Galfione, S. Carrara, and G. De Micheli, "All-solid-state Reference Electrodes for analytical applications," 2019.
- [17] I. N. Hanitra, F. Criscuolo, S. Carrara, and G. De Micheli, "Multi-Target Electrolyte Sensing Front-End for Wearable Physical Monitoring," in *PRIME 2019 - 15th Conference on Ph.D. Research in Microelectronics and Electronics, Proceedings*, pp. 249–252, 2019.
- [18] I. N. Hanitra, S. Member, F. Criscuolo, N. Pankratova, S. Carrara, and G. D. Micheli, "Multi-Channel Front-End for Electrochemical Sensing of Metabolites , Drugs , and Electrolytes," *IEEE sensors*, pp. 1–10, 2020.
- [19] F. Criscuolo, F. Cantù, I. Taurino, S. Carrara, and G. De Micheli, "A wearable electrochemical sensing system for non-invasive monitoring of Lithium drug in bipolar disorder," *submitted to IEEE sensors*.
- [20] F. Criscuolo, I. Ny Hanitra, S. Aiassa, S. Carrara, and G. De Micheli, "Wearable multi-sensing system for healthcare monitoring in sweat," *paper under submission*.
- [21] D. Riskin, "The next revolution in Healthcare," *Forbes*, vol. October, 2012.
- [22] J. Haughom, "The Rising Healthcare Revolution: The Future Is Already Here," 2014.

-
- [23] K. Maharatna and S. Bonfiglio, *Systems Design for Remote Healthcare*. Springer, 2014.
- [24] H. Shen, *Healthcare and Big Data Management*, vol. 1028. Springer, 2017.
- [25] A. Mena-Bravo and M. D. Luque de Castro, "Sweat: A sample with limited present applications and promising future in metabolomics," *Journal of Pharmaceutical and Biomedical Analysis*, vol. 90, pp. 139–147, 2014.
- [26] G. Matzeu, C. Zuliani, and D. Diamond, "Solid-Contact Ion-Selective Electrodes (ISEs) based on Ligand Functionalised Gold Nanoparticles," *Electrochim. Acta*, vol. 159, pp. 158–165, 2015.
- [27] G. Matzeu, L. Florea, and D. Diamond, "Advances in wearable chemical sensor design for monitoring biological fluids," *Sens. Actuators B*, vol. 211, pp. 403–418, 2015.
- [28] A. J. Bandodkar, I. Jeerapan, and J. Wang, "Wearable Chemical Sensors: Present Challenges and Future Prospects," *ACS Sensors*, p. acssensors.6b00250, 2016.
- [29] J. Heikenfeld, "Let them see you sweat," *IEEE Spectr.*, vol. 51, no. 11, pp. 46–63, 2014.
- [30] S. Anastasova-Ivanova, B. Crewther, P. Bembnowicz, V. Curto, H. M. Ip, B. Rosa, and G. Z. Yang, "A wearable multisensing patch for continuous sweat monitoring," *Biosens. Bioelectron.*, vol. 93, p. 730, 2017.
- [31] P. Kumar, K. H. Kim, V. Bansal, T. Lazarides, and N. Kumar, "Progress in the sensing techniques for heavy metal ions using nanomaterials," *Journal of Industrial and Engineering Chemistry*, vol. 54, pp. 30–43, 2017.
- [32] S. Chowdhury, B. Rooj, A. Dutta, and U. Mandal, "Review on Recent Advances in Metal Ions Sensing Using Different Fluorescent Probes," *Journal of Fluorescence*, vol. 28, no. 4, pp. 999–1021, 2018.
- [33] B. Kaur, N. Kaur, and S. Kumar, "Colorimetric metal ion sensors – A comprehensive review of the years 2011–2016," *Coordination Chemistry Reviews*, vol. 358, pp. 13–69, 2018.
- [34] N. Kaur and S. Kumar, "Colorimetric metal ion sensors," *Tetrahedron*, vol. 67, no. 48, pp. 9233–9264, 2011.
- [35] J. Hu, A. Stein, and P. Bühlmann, "Rational design of all-solid-state ion-selective electrodes and reference electrodes," *Trends Anal. Chem.*, vol. 76, pp. 102–114, 2016.
- [36] E. Bakker, P. Buhlmann, and E. Pretsch, "Polymer Membrane Ion-Selective Electrodes ± What are the Limits?," *Electroanalysis*, vol. 11, no. 13, pp. 915–933, 1999.
- [37] N. Rubinova, K. Chumbimuni-Torres, and E. Bakker, "Solid-contact potentiometric polymer membrane microelectrodes for the detection of silver ions at the femtomole level," *Sens. Actuators B*, vol. 121, no. 1, pp. 213–223, 2006.

- [38] C. C. Rundle, "A Beginners Guide to Ion-Selective Electrode Measurements," 2011.
- [39] W. E. Morf, "The Principles of ion-selective electrodes and of membrane transport," in *Volume 2*, Elsevier science Ltd, 1981.
- [40] P. C. Meier, "Two-parameter debye-hückel approximation for the evaluation of mean activity coefficients of 109 electrolytes," *Analytica Chimica Acta*, vol. 136, pp. 363–368, 1982.
- [41] E. Lindner and R. E. Gyurcsányi, "Quality control criteria for solid-contact , solvent polymeric membrane ion-selective electrodes," *J. Solid State Electrochem.*, vol. 13, pp. 51–68, 2009.
- [42] I. Taurino, G. Sanz , F. Mazzei, G. Favero, G. De Micheli, and S. Carrara, "Fast synthesis of platinum nanopetals and nanospheres for highly-sensitive non-enzymatic detection of glucose and selective sensing of ions," *Sci. Rep.*, vol. 5, no. October, p. 15277, 2015.
- [43] J. Bobacka, A. Ivaska, and A. Lewenstam, "Potentiometric ion sensors," *Chem. Rev.*, vol. 108, no. 2, pp. 329–351, 2008.
- [44] A. Lewenstam, "Routines and Challenges in Clinical Application of Electrochemical Ion-Sensors," *Electroanalysis*, vol. 26, no. 6, pp. 1171–1181, 2014.
- [45] H. Hirata, "Copper(I) sulphide-impregnated silicone rubber membranes as selective electrodes for copper(II) ions," *Talanta*, vol. 17, pp. 2–6, 1970.
- [46] R. W. Cattrall, H. Freiser, and R. W. Cattrall, "Coated Wire Ion Selective Electrodes," *Anal. Chem.*, vol. 43, no. 13, pp. 1905–1906, 1971.
- [47] E. Lindner and Y. Umezawa, "Performance evaluation criteria for preparation and measurement of macro- and microfabricated ion-selective electrodes (IUPAC Technical Report)," *Pure Appl. Chem.*, vol. 80, no. 1, pp. 85–104, 2008.
- [48] J. Bobacka, "Conducting Polymer-Based Solid-State Ion-Selective Electrodes," *Electroanalysis*, vol. 18, no. 1, pp. 7–18, 2006.
- [49] T. Yin and W. Qin, "Trends in Analytical Chemistry Applications of nanomaterials in potentiometric sensors," *Trends Anal. Chem.*, vol. 51, pp. 79–86, 2013.
- [50] A. Cadogan, Z. Gao, A. Lewenstam, A. Ivaska, D. Diamond, A. Lewenstam, and Z. Gao, "All-Solid-State Sodium-Selective Electrode Based on a Calixarene Ionophore in a Poly(vinyl chloride) Membrane with a Polypyrrole Solid Contact," *Analytical Chemistry*, vol. 64, no. 21, pp. 2496–2501, 1992.
- [51] J. Bobacka, "Potential Stability of All-Solid-State Ion-Selective Electrodes Using Conducting Polymers as Ion-to-Electron Transducers," *Anal. Chem.*, vol. 71, no. 21, pp. 4932–4937, 1999.

- [52] J. Bobacka, T. Lindfore, M. McCarrick, A. Ivaska, and A. Lewenstam, "Single-Piece All-Solid-State Ion-Selective Electrode," *Anal. Chem.*, vol. 67, no. 20, pp. 3819–3823, 1995.
- [53] J. Bobacka, M. Mccarrick, and A. Ivaskat, "All solid-state Poly(vinyl chloride) Membrane Ion-selective Electrodes With Poly(3-octylthiophene) Solid Internal Contact," *Analyst*, vol. 119, pp. 1985–1991, 1994.
- [54] C. Z. Lai, M. A. Fierke, A. Stein, and P. Bühlmann, "Ion-selective electrodes with three-dimensionally ordered macroporous carbon as the solid contact," *Anal. Chem.*, vol. 79, no. 12, pp. 4621–4626, 2007.
- [55] G. A. Crespo, S. Macho, and F. X. Rius, "Ion-selective electrodes using carbon nanotubes as ion-to-electron transducers," *Anal. Chem.*, vol. 80, no. 4, pp. 1316–1322, 2008.
- [56] J. Ping, Y. Wang, J. Wu, and Y. Ying, "Development of an all-solid-state potassium ion-selective electrode using graphene as the solid-contact transducer," *Electrochem. Commun.*, vol. 13, no. 12, pp. 1529–1532, 2011.
- [57] F. Li, J. Ye, M. Zhou, S. Gan, Q. Zhang, D. Han, and L. Niu, "All-solid-state potassium-selective electrode using graphene as the solid contact," *Analyst*, vol. 137, no. 3, pp. 618–623, 2012.
- [58] E. Jaworska, M. Wójcik, A. Kisiel, J. Mieczkowski, and A. Michalska, "Gold nanoparticles solid contact for ion-selective electrodes of highly stable potential readings," *Talanta*, vol. 85, no. 4, pp. 1986–1989, 2011.
- [59] B. Paczosa-Bator, L. Cabaj, R. Piech, and K. Skupień, "Potentiometric sensors with carbon black supporting platinum nanoparticles," *Anal. Chem.*, vol. 85, no. 21, pp. 10255–10261, 2013.
- [60] T. Yin, D. Pan, and W. Qin, "All-solid-state polymeric membrane ion-selective miniaturized electrodes based on a nanoporous gold film as solid contact," *Anal. Chem.*, vol. 86, no. 22, pp. 11038–11044, 2014.
- [61] E. Bakker and E. Pretsch, "Potentiometric sensors for trace-level analysis," *Trends Anal. Chem.*, vol. 24, no. 3, pp. 199–207, 2005.
- [62] M. Guzinski, J. M. Jarvis, B. D. Pendley, and E. Lindner, "Equilibration Time of Solid Contact Ion-Selective Electrodes," *Anal. Chem.*, vol. 87, pp. 6654–6659, 2015.
- [63] R. P. Buck and E. Lindner, "Recommendations for nomenclature of ion-selective electrodes (IUPAC recommendations 1994)," *Pur & Appl. Chem*, vol. 66, no. 12, pp. 2527–2536, 1994.
- [64] E. Bakker, E. Pretsch, and P. Buhlmann, "Selectivity of Potentiometric Ion Sensors," *Anal. Chem.*, vol. 72, no. 6, pp. 1127–1133, 2000.

- [65] M. A. Pineros, J. E. Shaff, L. V. Kochian, and E. Bakker, "Selectivity of Liquid Membrane Cadmium Microelectrodes Based on the Ionophore N,N,N',N'-Tetrabutyl-3,6-dioxaocanedithioamide Miguel," *Electroanalysis*, vol. 10, no. 14, pp. 937–941, 1998.
- [66] R. Cánovas, S. P. Sanchez, M. Parrilla, M. Cuartero, and G. A. Crespo, "Cytotoxicity Study of Ionophore-Based Membranes : Towards On-Body and In Vivo Ion Sensing Cytotoxicity Study of Ionophore-Based Membranes : Towards On-Body and In Vivo Ion Sensing," *ACS Sensors*, 2019.
- [67] R. Hernández, J. Riu, J. Bobacka, C. Vallés, P. Jiménez, A. M. Benito, W. K. Maser, and F. X. Rius, "Reduced graphene oxide films as solid transducers in potentiometric all-solid-state ion-selective electrodes," *J. Phys. Chem. C*, vol. 116, no. 42, pp. 22570–22578, 2012.
- [68] J. Ping, Y. Wang, Y. Ying, and J. Wu, "Application of electrochemically reduced graphene oxide on screen-printed ion-selective electrode," *Anal. Chem.*, vol. 84, no. 7, pp. 3473–3479, 2012.
- [69] M. Fouskaki and N. Chaniotakis, "Fullerene-based electrochemical buffer layer for ion-selective electrodes.," *Analyst*, vol. 133, pp. 1072–5, 2008.
- [70] J. Xu, F. Jia, F. Li, Q. An, S. Gan, Q. Zhang, A. Ivaska, and L. Niu, "Simple and Efficient Synthesis of Gold Nanoclusters and Their Performance as Solid Contact of Ion Selective Electrode," *Electrochim. Acta*, vol. 222, pp. 1007–1012, 2016.
- [71] F. X. Rius-Ruiz, G. A. Crespo, D. Bejarano-Nosas, P. Blondeau, J. Riu, and F. X. Rius, "Potentiometric strip cell based on carbon nanotubes as transducer layer: Toward low-cost decentralized measurements," *Anal. Chem.*, vol. 83, no. 22, pp. 8810–8815, 2011.
- [72] J. Hu, A. Stein, and P. Bühlmann, "A Disposable Planar Paper-Based Potentiometric Ion-Sensing Platform," *Angew. Chem. Int. Ed.*, vol. 55, no. 26, pp. 7544–7547, 2016.
- [73] S. T. Mensah, Y. Gonzalez, P. Calvo-Marzal, and K. Y. Chumbimuni-Torres, "Nanomolar detection limits of Cd²⁺, Ag⁺, and K⁺ using paper-strip ion-selective electrodes," *Anal. Chem.*, vol. 86, no. 15, pp. 7269–7273, 2014.
- [74] B. Schazmann, D. Morris, C. Slater, S. Beirne, C. Fay, R. Reuveny, N. Moyna, and D. Diamond, "A wearable electrochemical sensor for the real-time measurement of sweat sodium concentration," *Anal. Methods*, vol. 2, no. 4, p. 342, 2010.
- [75] A. J. Bandodkar and J. Wang, "Non-invasive wearable electrochemical sensors: A review," *Trends in Biotechnology*, vol. 32, no. 7, pp. 363–371, 2014.
- [76] V. A. T. Dam, M. A. G. Zevenbergen, and R. van Schaijk, "Toward wearable patch for sweat analysis," *Sens. Actuators B*, vol. 236, pp. 834–838, 2016.

- [77] D. P. Rose, M. E. Ratterman, D. K. Griffin, L. Hou, N. Kelley-Loughnane, R. R. Naik, J. A. Hagen, I. Papautsky, and J. C. Heikenfeld, "Adhesive RFID sensor patch for monitoring of sweat electrolytes," *IEEE Trans. Biomed. Eng.*, vol. 62, no. 6, pp. 1457–1465, 2015.
- [78] S. Emaminejad, W. Gao, E. Wu, Z. A. Davies, H. Yin Yin Nyein, S. Challa, S. P. Ryan, H. M. Fahad, K. Chen, Z. Shahpar, S. Talebi, C. Milla, A. Javey, and R. W. Davis, "Autonomous sweat extraction and analysis applied to cystic fibrosis and glucose monitoring using a fully integrated wearable platform," *Proceedings of the National Academy of Sciences*, vol. 114, no. 18, pp. 4625–4630, 2017.
- [79] M. Parrilla, M. Cuartero, and G. A. Crespo, "Wearable potentiometric ion sensors," *Trends Anal. Chem.*, vol. 110, pp. 303–320, 2019.
- [80] J. C. Heikenfeld and Z. C. Sonner, "Devices for integrated, repeated, prolonged, and/or reliable sweat stimulation and biosensing," 2015.
- [81] J. Heikenfeld, D. P. Rose, I. Papautsky, W. Kang, X. Wang, and M. Ratterman, "Sweat sensing device communication security and compliance," tech. rep., Eccrine Systems , Inc ., 2018.
- [82] "<https://www.eccrinesystems.com/>."
- [83] "<https://www.kenzen.com/>."
- [84] A. Michalska, "All-Solid-State Ion Selective and All-Solid-State Reference Electrodes," *Electroanalysis*, vol. 24, no. 6, pp. 1253–1265, 2012.
- [85] M. Fibbioli, W. E. Morf, M. Badertscher, N. F. D. Rooij, and È. Pretsch, "Potential Drifts of Solid-Contacted Ion-Selective Electrodes Due to Zero-Current Ion Fluxes Through the Sensor Membrane," *Electroanalysis*, vol. 12, no. 16, pp. 1286–1292, 2000.
- [86] E. J. Parra, F. X. Rius, and P. Blondeau, "A potassium sensor based on non-covalent functionalization of multi-walled carbon nanotubes," *Analyst*, vol. 138, no. 9, p. 2698, 2013.
- [87] S. Roy, M. David-Pur, and Y. Hanein, "Carbon Nanotube-Based Ion Selective Sensors for Wearable Applications," *ACS Appl. Mater. Interfaces*, vol. 9, no. 40, pp. 35169–35177, 2017.
- [88] R. Liang, T. Yin, and W. Qin, "A simple approach for fabricating solid-contact ion-selective electrodes using nanomaterials as transducers," *Anal. Chim. Acta*, vol. 853, no. 1, pp. 291–296, 2015.
- [89] J. Li, T. Yin, and W. Qin, "An all-solid-state polymeric membrane Pb²⁺-selective electrode with bimodal pore C60 as solid contact," *Anal. Chim. Acta*, vol. 876, pp. 49–54, 2015.

- [90] T. Zhang, C. Z. Lai, M. A. Fierke, A. Stein, and P. Bühlmann, "Advantages and limitations of reference electrodes with an ionic liquid junction and three-dimensionally ordered macroporous carbon as solid contact," *Anal. Chem.*, vol. 84, no. 18, pp. 7771–7778, 2012.
- [91] J. Ye, F. Li, S. Gan, Y. Jiang, Q. An, Q. Zhang, and L. Niu, "Using sp²-C dominant porous carbon sub-micrometer spheres as solid transducers in ion-selective electrodes," *Electrochem. Commun.*, vol. 50, pp. 60–63, 2015.
- [92] Z. A. Boeva and T. Lindfors, "Few-layer graphene and polyaniline composite as ion-to-electron transducer in silicone rubber solid-contact ion-selective electrodes," *Sens. Actuators B*, vol. 224, pp. 624–631, 2015.
- [93] B. Paczosa-Bator, L. Cabaj, M. Pięk, R. Piech, and W. W. Kubiak, "Carbon-Supported Platinum Nanoparticle Solid-State Ion Selective Electrodes for the Determination of Potassium," *Anal. Lett.*, vol. 48, no. 17, pp. 2773–2785, 2015.
- [94] X. Zeng and W. Qin, "A solid-contact potassium-selective electrode with MoO₂ microspheres as ion-to-electron transducer," *Anal. Chim. Acta*, vol. 982, pp. 72–77, 2017.
- [95] G. Sanzó, I. Taurino, R. Antiochia, L. Gorton, G. Favero, F. Mazzei, G. D. Micheli, and S. Carrara, "Bioelectrochemistry Bubble electrodeposition of gold porous nanocorals for the enzymatic and non-enzymatic detection of glucose," *Bioelectrochemistry*, vol. 112, pp. 125–131, 2016.
- [96] M. Novell, T. Guinovart, P. Blondeau, F. X. Rius, and F. J. Andrade, "A paper-based potentiometric cell for decentralized monitoring of Li levels in whole blood," *Lab Chip*, vol. 14, no. 7, p. 1308, 2014.
- [97] F. Coldur and M. Andac, "All-Solid-State Polyvinyl Chloride Membrane Lithium-Selective Electrode with Improved Selectivity and Its Application in Serum Lithium Assay," *Sensor Lett.*, vol. 9, no. 5, pp. 1738–1744, 2011.
- [98] D. Gruson, A. Lallali, A. M. Taburet, A. Legrand, M. Conti, and L. D. Biochimie, "Evaluation of a new lithium colorimetric assay performed on the Dade Behring Dimension X-pand system," *Clin. Chem. Lab. Med.*, vol. 42, no. 9, pp. 1066–1068, 2004.
- [99] J.-p. Veder, R. D. Marco, G. Clarke, R. Chester, A. Nelson, K. Prince, E. Pretsch, and E. Bakker, "Elimination of undesirable water layers in solid contact polymeric ion-selective electrodes," *Anal. Chem.*, vol. 80, no. 17, pp. 6731–6740, 2008.
- [100] G. Matzeu, C. Zuliani, and D. Diamond, "Recent Progress in Disposable Ion-Selective Sensors for Environmental Applications," *Adv. Sci. Technol.*, vol. 77, pp. 65–70, 2012.
- [101] R. W. Licht, "Lithium : Still a Major Option in the Management of Bipolar Disorder Acute Antimanic Actions of Lithium," *CNS Neurosci. Ther.*, vol. 18, pp. 219–226, 2012.

-
- [102] K. A. Kaplan and A. G. Harvey, "Behavioral Treatment of Insomnia in Bipolar Disorder," *Am. J. Psychiatry*, vol. 170, no. 7, pp. 716–720, 2013.
- [103] V. Umamaheswari, A. Avasthi, and G. S. Risk, "Risk factors for suicidal ideations in patients with bipolar disorder," *Bipolar disord.*, vol. 16, pp. 642–651, 2014.
- [104] M. Pompili, M. Innamorati, M. Raja, G. Ducci, G. Angeletti, D. Lester, P. Girardi, R. Tatarelli, and E. D. Pisa, "Suicide risk in depression and bipolar disorder : Do impulsiveness-aggressiveness and pharmacotherapy predict suicidal intent ?," *Neuropsychiatr. Dis. Treat.*, vol. 4, no. 1, pp. 247–255, 2008.
- [105] A. Muneer, "Staging Models in Bipolar Disorder : A Systematic Review of the Literature," *Clin. Psychopharmacol. Neurosci.*, vol. 14, no. 2, pp. 117–130, 2016.
- [106] H. S. Hopkins and J. Gelenberg, "Serum lithium levels and the outcome of maintenance therapy of bipolar disorder," *Bipolar disord.*, vol. 2, pp. 174–179, 2000.
- [107] G. D. Christian, "Reagents for Lithium Electrodes and Sensors for Blood Serum," *Sensors*, vol. 2, pp. 432–435, 2002.
- [108] B. Rumbelow and M. Peake, "Performance of a novel spectrophotometric lithium assay on a routine biochemistry analyser," *Ann. Clin. Biochem.*, vol. 38, pp. 684–686, 2001.
- [109] R. H. Christenson, J. J. Mandichak, S. Hong, J. M. Augustyn, and J. C. Thompson, "Clinical performance characteristics of a new photometric lithium assay : a multicenter study," *Clin. Chim. Acta*, vol. 327, pp. 157–164, 2003.
- [110] W. Glazer, J. Sonnenberg, M. Reinstein, and R. Akers, "A novel, point-of-care test for lithium levels: description and reliability," *J. Clin. Psychiatry*, vol. 65, no. 5, pp. 652–5, 2004.
- [111] F. Coldur and M. Andac, "A Flow-Injection Potentiometric System for Selective and Sensitive Determination of Serum Lithium Level," *Electroanalysis*, vol. 25, no. 3, pp. 732–740, 2013.
- [112] M. Kamenica, R. R. Kothur, A. Willows, and B. A. Patel, "Lithium Ion Sensors," *Sensors*, vol. 17, p. 2430, 2017.
- [113] B. Leboulanger, J. M. Aubry, G. Bondolfi, R. H. Guy, and M. B. Delgado-Charro, "Lithium monitoring by reverse iontophoresis in vivo," *Clinical Chemistry*, vol. 50, no. 11, pp. 2091–2100, 2004.
- [114] T. Kilic, V. Brunner, L. Audoly, and S. Carrara, "Smart e-Patch For Drugs Monitoring in Schizophrenia," in *2016 IEEE International Conference on Electronics, Circuits and Systems (ICECS)*, pp. 57–60, IEEE, 2016.

- [115] F. Coldur, M. Andac, and I. Isildak, "Flow-injection potentiometric applications of solid state Li + selective electrode in biological and pharmaceutical samples," *Journal of Solid State Electrochemistry*, vol. 14, no. 12, pp. 2241–2249, 2010.
- [116] K. Kimura, H. Yano, S. Kitazawa, and T. Shono, "Synthesis and Selectivity for Lithium of Lipophilic 14-Crown-4 Derivatives bearing Bulky Substituents or an Additional Binding Site in the Side Arm," *J. Chem. Soc. Perkin Trans. II*, no. 12, pp. 1945–1951, 1986.
- [117] E. Bakker, "Selectivity of Liquid Membrane Ion-Selective Electrodes," *Electroanalysis*, vol. 9, no. 1, pp. 7–12, 1997.
- [118] A. K. Yousuf, M. Misbahuddin, and M. S. Rahman, "Secretion of arsenic, cholesterol, vitamin E, and zinc from the site of arsenical melanosis and leucomelanosis in skin," *Clinical Toxicology*, vol. 49, no. 5, pp. 374–378, 2011.
- [119] M. E. Sears, K. J. Kerr, and R. I. Bray, "Arsenic, cadmium, lead, and mercury in sweat: A systematic review," *Journal of Environmental and Public Health*, vol. 2012, no. February 2012, 2012.
- [120] S. G. Lilley, T. M. Florence, and J. L. Stauber, "The use of sweat to monitor lead absorption through the skin," *Science of the Total Environment*, The, vol. 76, no. 2-3, pp. 267–278, 1988.
- [121] S. Jadoon, S. Karim, M. R. Akram, A. Kalsoom Khan, M. A. Zia, A. R. Siddiqi, and G. Murtaza, "Recent developments in sweat analysis and its applications," *International Journal of Analytical Chemistry*, vol. 2015, 2015.
- [122] M. Fouskaki and N. A. Chaniotakis, "Thick Membrane , Solid Contact Ion Selective Electrode for the Detection of Lead at Picomolar Levels," *Anal. Chem.*, vol. 77, no. 6, pp. 1780–1784, 2005.
- [123] C. Wardak and J. Lenik, "New lead-sensitive ion selective electrode with low detection limit," *E3S Web of Conferences*, vol. 1, no. 3, pp. 2–5, 2013.
- [124] S. Yu, F. Li, T. Yin, Y. Liu, D. Pan, and W. Qin, "A solid-contact Pb²⁺-selective electrode using poly(2-methoxy-5-(2-ethylhexyloxy)-p-phenylene vinylene) as ion-to-electron transducer," *Anal. Chim. Acta*, vol. 702, no. 2, pp. 195–198, 2011.
- [125] W. J. Zhang, C. Y. Li, X. B. Zhang, and Z. Jin, "Synthesis of an amide-linked diporphyrin xanthene as a neutral carrier for a lead(II)-sensitive electrode," *Analytical Letters*, vol. 40, no. 6, pp. 1023–1035, 2007.
- [126] A. J. Mccubbin and R. J. S. Costa, "The Impact of Dietary Sodium Intake on Sweat Sodium Concentration in Response to Endurance Exercise : A Systematic Review," *International Journal of Sports Science*, vol. 8, no. 1, pp. 25–37, 2018.
- [127] S. Ferner, R. Koszmagk, A. Lehmann, and H. W, "Reference values of Na(+) and Cl(-) concentrations in adult sweat," *Z Erkr atmungsorgane*, vol. 175, no. 2, pp. 70–75, 1990.

- [128] B. Lara, C. Gallo-Salazar, C. Puente, F. Areces, J. J. Salinero, and J. Del Coso, "Interindividual variability in sweat electrolyte concentration in marathoners," *Journal of the International Society of Sports Nutrition*, vol. 13, no. 1, pp. 1–8, 2016.
- [129] S. J. Montain, S. N. Cheuvront, and H. C. Lukaski, "Sweat mineral-element responses during 7 h of exercise-heat stress," *International Journal of Sport Nutrition and Exercise Metabolism*, vol. 17, no. 6, pp. 574–582, 2007.
- [130] D. M. Band, J. Kratochvil, P. A. P. Wilson, and T. Treasure, "Relationship Between Activity and Concentration Measurements of Plasma Potassium," *Analyst*, vol. 103, no. 246, pp. 246–251, 1978.
- [131] T. Ghosh, H. J. Chung, and J. Rieger, "All-solid-state sodium-selective electrode with a solid contact of chitosan/prussian blue nanocomposite," *Sensors (Switzerland)*, vol. 17, no. 11, 2017.
- [132] K. Wygladacz, M. Durnaś, P. Parzuchowski, Z. Brzózka, and E. Malinowska, "Miniaturized sodium-selective sensors based on silicon back-side contact structure with novel self-plasticizing ion-selective membranes," *Sensors and Actuators, B: Chemical*, vol. 95, no. 1-3, pp. 366–372, 2003.
- [133] S. Chandra and H. Lang, "A new sodium ion selective electrode based on a novel silacrown ether," *Sensors and Actuators, B: Chemical*, vol. 114, no. 2, pp. 849–854, 2006.
- [134] B. Sethi, S. Chandra, S. Kumar, R. Singh, and L. P. Singh, "Crown ether-dendrimer based potentiometric Na⁺ sensor electrode," *Journal of Electroanalytical Chemistry*, vol. 651, no. 2, pp. 185–190, 2011.
- [135] C. Boero, *Electrochemical Biosensors for On-line Monitoring of Cell Culture Metabolism Cristina BOERO*. PhD thesis, EPFL, 2012.
- [136] C. M. A. Brett and A. M. O. Brett, *Electrochemistry: Principles, methods, and applications*. Oxford University Press, 1993.
- [137] M. Ohring, *The material science of thin films*. Academic press, 1992.
- [138] H. Frey and H. R. Khan, *Handbook of Thin-Film Technology*. 2015.
- [139] M. Sophocleous and J. K. Atkinson, "A review of screen-printed silver/silver chloride (Ag/AgCl) reference electrodes potentially suitable for environmental potentiometric sensors," *Sensors and Actuators, A: Physical*, vol. 267, pp. 106–120, 2017.
- [140] U. Guth, "Solid-state reference electrodes for potentiometric sensors," *Journal of Solid State Electrochemistry*, no. January 2009, 2009.
- [141] M. W. Shinwari, D. Zhitomirsky, I. A. Deen, P. R. Selvaganapathy, M. J. Deen, and D. Landheer, "Microfabricated Reference Electrodes and their Biosensing Applications," *Sensors*, no. 10, pp. 1679–1715, 2010.

Bibliografia

- [142] R. Maminska, A. Dybko, and W. Wr, "All-solid-state miniaturised planar reference electrodes based on ionic liquids," *Sens. Actuators B*, vol. 115, pp. 552–557, 2006.
- [143] I.-y. Huang and R.-s. Huang, "Fabrication and characterization of a new planar solid-state reference electrode for ISFET sensors," *Thin Solid Films*, vol. 406, pp. 255–261, 2002.
- [144] W.-y. Liao and T.-c. Chou, "Fabrication of a Planar-Form Screen-Printed Solid Electrolyte Modified Ag / AgCl Reference Electrode for Application in a Potentiometric Biosensor," *Anal Chem*, vol. 78, no. 12, pp. 4219–4223, 2006.
- [145] V. A. T. Dam, M. Goedbloed, and M. A. G. Zevenbergen, "Solid-Contact Reference Electrode for Ion-Selective Sensors," in *Eurosensors Paris 2017*, vol. 1, p. 464, 2017.
- [146] T. Guinovart, G. A. Crespo, F. X. Rius, and F. J. Andrade, "A reference electrode based on polyvinyl butyral (PVB) polymer for decentralized chemical measurements," *Analytica Chimica Acta*, vol. 821, pp. 72–80, 2014.
- [147] P. R. Childs, J. R. Greenwood, and C. A. Long, "Review of temperature measurement," *Review of Scientific Instruments*, vol. 71, no. 8, pp. 2959–2978, 2000.
- [148] D. H. Dickey, "A Spreading Resistance Technique for Resistivity Measurements on Silicon," *Journal of the Electrochemical Society*, vol. 113, no. 3, pp. 255–259, 1966.

FRANCESCA CRISCUOLO

Address: Rue des Echelettes, 3
Lausanne, 1004 (Switzerland)
E-mail: fcriscuolo91@gmail.com
Mobile: +41 775041448
Citizenship: Italian
Birth: 22/03/1991, Milan, Italy
Gender: female



Graduated with honors in "Materials engineering and Nanotechnology", she is using her expertise to develop next-generation electronics and to improve healthcare.

PROFESSIONAL EXPERIENCE

May 2016 – April 2020



Research doctoral assistant at Laboratory of Integrated System at EPFL

Project: Multi-sensing electrochemical platform for immunohematology and for novel flexible biosensors

Ideation and optimization of new nanostructured electrochemical sensors for healthcare applications. Implementation in both rigid and flexible multi-electrodes platforms fabricated in cleanroom. Integration with stirring circuits and read-out electronics.

July 2015 – April 2016



Research internship at IMEC (Leuven, Belgium)

Project: Thin-film lithium-ion conductors for solid-state batteries

Ideation, cleanroom fabrication and characterization of novel electrolytes materials for thin-film solid-state batteries. Investigation of compatible stacks for 3D batteries. Expertise achieved in several thin film deposition and in morphological, thermal, compositional, structural and electrical characterization methods.

EDUCATION

July 2014 – July 2015



Msc exchange student in "Materials science and engineering" Delft University of Technology (Delft, The Netherlands)

- *Project: Engineered vascular graft with lithographically controlled 3D micro and nanotopography*
- *Project: Kawasaki Ninja Motorbike– Exhaust System – Material challenge*

October 2013 –
April 2016



POLITECNICO
MILANO 1863

Msc in "Materials engineering and nanotechnology" Politecnico di Milano (Milan, Italy) MARK: 110/110 cum laude

September 2010 –
September 2013



POLITECNICO
MILANO 1863

BEng in "Materials engineering and nanotechnology" Politecnico di Milano (Milan, Italy) MARK: 110/110 cum laude

- *PRIZE HONOR STUDENT "Giuseppe Baiardi"*
- *Research project on new materials, surfaces and MEMS devices in microfluidics for diagnostics and chemical engineering*
- *Research project on nanostructured materials for PV applications* 139
- *THESIS: "Characterization of Nanostructured Titanium dioxide for Photocatalytic applications"*

March 2013



Athens Programme

Ceske vysoke uceni technicke v praze (Praha, Czech Republic)

Course and laboratory on vibrational spectroscopy

November 2012



Athens Programme

École nationale des ponts et Chaussées - Paris Tech (Paris, France)

MARK: A+

Course on quantum mechanics and theory of chaos

October 2012



Piano diploma

Conservatorio G.Cantelli (Novara,Italy)

Mark: 10/10

- Absolute winner of "S. Preatoni" music competition
- Absolute first prize in the national competition "J.S. Bach"
- Awarded in many national and international competitions

KEY SKILLS

- Project management and supervision
- Team player
- Creative problem solving
- Time management

LANGUAGE SKILLS

Italian: Mother tongue

French: Very good

German: Basic

English: Fluent

Spanish: Good

COMPUTING SKILLS

- Origin, Matlab, SketchUp, Abaqus, Image J, CES selector, MEISP, Nova, L-edit

PERSONAL INTERESTS

- Reading, music, sports, travelling and experiencing different cultures

PUBLICATIONS

Peer-reviewed papers in international journals

1. **F. Criscuolo**; I. Ny Hanitra; *et al.*: Wearable multi-sensing system for healthcare monitoring in sweat.; *paper under submission*.
2. **F. Criscuolo**; F. Cantù; *et al.*: A wearable electrochemical sensing system for non-invasive monitoring of Lithium drug in bipolar disorder.; *submitted to IEEE sensors*.
3. **F. Criscuolo**; I. Taurino; *et al.*: Fast procedures for the electrodeposition of platinum nanostructures on miniaturized electrodes for improved ion sensing.; MDPI sensors, 2019.
4. M. I. Ny Hanitra; **F. Criscuolo** *et al.*: Multi-Channel Front-End for Electrochemical Sensing of Metabolites, Drugs, and Electrolytes.; IEEE sensors journal, 2019.
5. A. Sepulveda; **F. Criscuolo**; *et al.*: Effect of high temperature LiPON electrolyte in all solid-state batteries.; Solid State Ionics, 2019.
6. **F. Criscuolo**; I. Taurino *et al.*: Highly-stable Li + ion-selective electrodes based on noble metal nanostructured layers as solid-contacts; Analytica Chimica Acta, 2018.

Peer-reviewed conference papers

7. **F. Criscuolo**; F. Cantù *et al.*: Flexible sweat sensors for non-invasive optimization of lithium dose in psychiatric disorders. IEEE SENSORS 2019, Montreal, Canada. [2nd best paper award]
8. M. I. Ny Hanitra; **F. Criscuolo** *et al.*: Multi-Target Electrolyte Sensing Front-End for Wearable Physical Monitoring. PRIME 2019, Lausanne, Switzerland, July 2019.
9. **F. Criscuolo**; M. Galfione *et al.*: All solid-state Reference Electrodes for analytical applications. IWASI 2019, Otranto, Italy, June 2019.
10. **F. Criscuolo**; L. Lobello; *et al.*: Mixed Gold and Platinum Nanostructured Layers for All-Solid-State Ion Sensors. 7th IEEE SENSORS, New Delhi, India, October 2018.
11. **F. Criscuolo**; I. Taurino *et al.*: A novel electrochemical sensor for non-invasive monitoring of lithium levels in mood disorders. 40th International Conference of the IEEE Engineering in Medicine and Biology Society (EMBC), Honolulu, Hawaii, USA, July 2018.
12. M. I. Ny Hanitra; L. Lobello; F. Stradolini; A. Tuoheti; **F. Criscuolo** *et al.*: A Flexible Front-End for Wearable Electrochemical Sensing. 2018 IEEE International Symposium on Medical Measurements and Applications (MeMeA), Rome, Italy, June 2018.
13. **F. Criscuolo**; I. Taurino *et al.*: An electrochemical sensor for quantitative analysis of Rhesus D antibodies in blood. 7th IEEE International Workshop on Advances in Sensors and Interfaces (IWASI), Vieste, Italy, June 2017.

AWARDS

- **2nd BEST PAPER AWARD AT THE IEEE Sensors Conference 2019** in Montreal , Canada, with the article F. Criscuolo; F. Cantù *et al.*: Flexible sweat sensors for non-invasive optimization of lithium dose in psychiatric disorders. IEEE SENSORS 2019, Montreal, Canada.
- **PRIZE HONOR STUDENT** “Giuseppe Baiardi” 2010